ELECTRONIC PROPERTIES OF FEW-LAYER TWISTRONIC GRAPHENE

A thesis submitted to the University of Manchester
for the degree of Doctor of Philosophy
in the Faculty of Science and Engineering

2021

Lok Ting Bonnie Tsim
School of Natural Sciences

Contents

Word count 17613

The University of Manchester

Lok Ting Bonnie Tsim
Doctor of Philosophy
Electronic properties of few-layer twistronic graphene
December 22, 2021

This thesis is dedicated to the electronic properties of few-layer twistronic graphene, and in particular, the electron transport in twisted bilayer graphene. I introduce the continuum-model Hamiltonian to describe twisted graphene heterostructures and give an overview of the band structures for twisted bilayer graphene, twisted double bilayer graphene and twisted monolayer-bilayer graphene.

In this thesis, I show that the electronic properties in twisted bilayer graphene are different for varying twist angles. For relatively large angles of $\sim 2^\circ$, I model transverse magnetic focusing and theoretically explain the ballistic transport observed in the experiment. In addition, we study the effects of an applied displacement field to the system where we observe selective focusing from each minivalley. At relatively smaller angles below 1° with a large perpendicular electric field, we found that there are independent, perfect one-dimensional channels propagating in three different directions in the lattice. Using the continuum-model Hamiltonian, we demonstrate that an applied bias causes two well-defined energy windows on either side of zero energy that contain the one-dimensional channels. Lastly, the resistivity from umklapp electron-phonon interaction is analytically calculated for twisted bilayer graphene and twisted double bilayer graphene. This is a specific mechanism where an electron tunnels from one layer to another layer whilst transferring momentum to the superlattice. We find that there is a weak contribution to resistivity even at room temperature.

Declaration

No portion of the work referred to in the thesis has been submitted in support of an application for another degree or qualification of this or any other university or other institute of learning.

Copyright Statement

Acknowledgements

I would like to say a heartfelt thank you to all the people who have helped and supported me along the course of my PhD. The path has been nothing short of a character-building experience filled with joyous occasions, tough challenges and introspective moments. I would first like to thank my supervisor Professor Vladimir Fal'ko for his guidance, patience and support. It has been a privilege to learn from such an incredible physicist and I feel truly fortunate for the opportunity to work in the Theory Group at the National Graphene Institute. I reserve a special thank you to Dr. John Wallbank who was my lecturer in my second-year undergraduate at Lancaster University. He inspired me to follow in his footsteps in the field of 2D materials and has been a great source of wisdom and support over the last few years. Moreover, I am thankful for the opportunity to work at Osaka University with Professor Mikito Koshino and our collaborator Dr. Nguyen N. T. Nam whilst exploring Japan on the JSPS Summer Programme. The PhD experience has exceeded my wildest dreams with opportunities to travel, learn about the industry and try startups. I have met and worked with many talented individuals: Adrian Ceferino, Angelika Knothe, Aitor Garcia-Ruiz, Christian Moulsdale and many others. I am truly grateful. In addition, I thank Yanmeng Shi for the insightful discussions on the electronic properties of twisted double bilayer graphene and twisted monolayer-bilayer graphene presented in Chapter 2. In particular, I thank Alexey Berdyugin who I collaborated with to interpret results from transport experiments on twisted bilayer graphene, which are presented in Chapter 3. Moreover, I have had an incredible experience on the Graphene NOWNANO Centre of Doctoral Training and I am thankful for the friends I have made along the way. Lastly, I express my gratitude towards my Mum and family for their continuous encouragement leading to the completion of this thesis.

Chapter 1

Introduction

For decades, scientists around the world theorised about the potential existence of graphene. Graphene is an allotrope of carbon and can be found in what we call pencil lead as part of a material called graphite. Graphite is a three-dimensional crystalline form of the element carbon with its atoms arranged in a hexagonal structure. When we isolate a single layer of graphite, we obtain graphene, which is a single layer of carbon atoms arranged in the shape of a two-dimensional honeycomb lattice.

In 2004, graphene gained global traction from researchers when it was first isolated and characterised by Andre Geim and Konstantin Novoselov at the University of Manchester [1]. Using adhesive tape, the mechanical exfoliation technique was used to extract graphene from a single piece of graphite. This was the first time a truly two-dimensional material was ever isolated in human history. Graphene is a promising material for next-generation electronic devices as a result of the rich physical phenomena and electronic properties observed in the material [2]. In the following years, a variety of unique properties and physical phenomena not found in bulk three-dimensional materials were discovered. This was a springboard to the start of an exciting new era of condensed matter physics and materials science in two-dimensional materials.

Following this, there has been intense interest in a new class of two-dimensional materials called van der Waals heterostructures [3, 4]. These materials are artificially stacked atomic layers where isolated atomic planes are designed, fabricated and produced layer by layer. Crystallographic alignment of atomically thin crystals stacked together in a van der Waals heterostructure is a powerful tool that enables fine-tuning of their

electronic spectra and thus opens up a wealth of opportunity for revealing novel physics where different materials can be selected, the number of layers chosen, as well as the ability to finely tune the relative crystallographic alignment between successive layers.

One of the most researched van der Waals heterostructures is graphene overlaid on hexagonal boron nitride (hBN) that emerged as a promising substrate for graphene devices to enhance its electronic properties [5, 6]. Hexagonal boron nitride, like graphene, is atomically flat with a honeycomb lattice structure. It is an insulating material with a lattice constant that is 1.8% longer than the graphene lattice constant. This small lattice mismatch combined with any relative twist angle between their crystallographic axes generates a large-scale periodic hexagonal interference pattern known as a moiré superlattice. The superlattice potential results in a reconstruction of the graphene band structure offering a myriad of opportunities to observe new physical phenomena. There are many research studies on graphene/hBN heterostructures where novel physics has been realised including enhanced electronic mobility in graphene and the first realisation of Hofstadter's butterfly [7, 8].

In the past few years, a graphene superlattice called twisted bilayer graphene (TBG) attracted a surge of interest from the condensed matter physics community. Unlike graphene/hBN heterostructures where one layer is conductive and one is insulating, both layers of graphene have the same lattice constant and are conductive. This gives rise to electronic states that are hybridised in different ways depending on the twist angle. These twist-engineered changes in the electronic properties of TBG have been shown to exhibit many interesting physical phenomena. A twist at discrete 'magic' angles results in flattened low-energy bands, periodically modulated interlayer hybridisation and a strong enhancement of electron correlations, which led to the discovery of superconductivity and Mott insulator transitions in TBG [9, 10, 11]. Consequently, there has been an avalanche of theoretical and experimental research in the field of graphene twistronics. Many theoretical studies are investigating the low-energy electronic spectrum in TBG, most notably, the presence of the moiré superlattice potential that reduces the Fermi velocity at the Dirac points as the twist angle between the two layers decrease and the emergence of van Hove singularities [12].

The long-range wavelength of the superlattice period means that the size of the

Brillouin zone is reduced. This leads to the interaction between the original Dirac cones of the two graphene layers to generate minibands, which has been captured experimentally via scanning tunnelling microscopy [13, 14, 15]. Figure 1.1a shows two graphene lattices overlaid on top of each other with an in-plane relative twist resulting in a moiré pattern. In the absence of interlayer coupling, the low-energy band structure consists of four Dirac cones from the two layers and two valleys, as illustrated in Fig. 1.1b. In the presence of interlayer coupling, the Dirac cones from each layer hybridise with each other to produce avoided crossings, and leads to the formation of van Hove singularities in the band structure. At large twist angles, the low-energy band structure resembles that of two decoupled graphene layers as the Dirac cones from each layer are far apart from each other. As the twist angle decreases, the hybridisation between the layers means that the low-energy Dirac cone states become coupled.

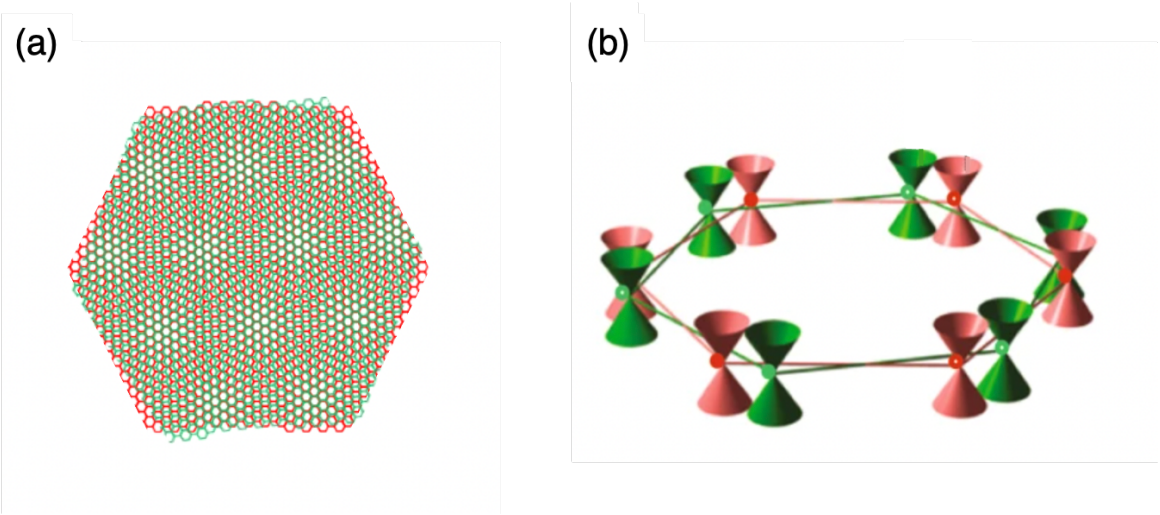

Figure 1.1: (a) Two graphene lattices superimposed on top of each other with an in-plane relative twist to give TBG. (b) The red and green hexagons are the original Brillouin zones of the individual graphene layers where the Dirac cones from each graphene layer are shown. Alternating corners of the hexagons belong to inequivalent sets of K and K' Brillouin zone corners shown by the open and closed circles. Figure adapted from Ref. [16].

Twisted bilayer graphene consists of two layers of graphene overlaid on top of each other with an in-plane relative twist. This rotation gives rise to a moiré pattern with a superlattice period given by $\lambda = \frac{a}{2\sin(\theta/2)}$ where a is the graphene lattice constant. The moiré pattern has three characteristic areas that resemble AA, AB and BA stacking regions. Figure 1.2 shows the moiré superlattice where the local stacking arrangement

between the atoms in the two graphene layers are shown. In the right panel, the interlayer coupling strength as a function of the position is shown. This means that at each position, the local stacking arrangement is considered to be homogeneous. We see that the interlayer coupling strength in AA regions reaches a maximum energy eigenvalue shown by the red regions as tunnelling between the two layers produces a gap in AA-stacked bilayer graphene. Conversely, the energy eigenvalue vanishes at AB and BA regions where tunnelling between the two layers does not produce a gap. In this thesis, we study ballistic transport and consider twisted graphene heterostructures without disorder where the mean free path exceeds the superlattice period [17]. Experimentally, high-quality graphene encapsulated with hBN is needed to support long-range ballistic transport in TBG [18]. This work will probe the electronic properties of the minibands to analyse the transport properties in graphene twistronic systems.

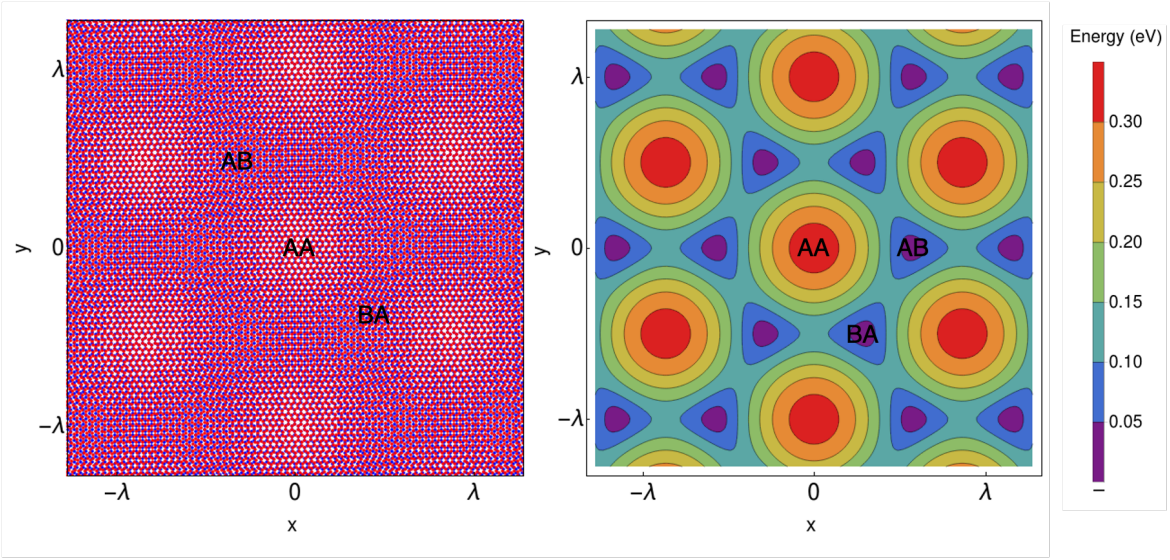

Figure 1.2: The left panel is the moiré pattern in TBG where two graphene layers are stacked on top of each other with a relative twist angle θ. The moiré superlattice period is given by $\lambda = \frac{a}{2\sin(\theta/2)}$ where a is the graphene lattice constant. The local stacking regions AA, AB and BA are shown. The right panel shows the energy eigenvalues of the interlayer coupling Hamiltonian between the two layers. At AA regions, we reach a local maxima and at AB and BA stacking regions, the energy eigenvalues vanish.

This thesis is organised as follows: In Chapter 2, we probe the electronic properties of twisted graphene heterostructures. This is addressed by formulating a continuum-model Hamiltonian to describe twisted bilayer graphene and extending the theory to two other graphene moiré systems, twisted double bilayer graphene (TDBG) and twisted monolayer-bilayer graphene (TMBG). TDBG is composed of two AB-stacked bilayer graphene layers rotationally stacked on top of each other whereas TMBG consists of bilayer graphene stacked on top of monolayer graphene. Chapter 3 addresses the ballistic transport properties of TBG in a regime where the angles are larger than the magic angle at $\sim 2^{\circ}$. This work was conducted in collaboration with experimentalists at the University of Manchester where we showed that the band structure of TBG can be probed using a magnetic field applied to the sample to observe the transverse magnetic focusing of electrons. In addition, we studied the effect of an electric displacement field on the system where minivalley polarised magnetic focusing was observed. The chapter will present the experimental data supported by theoretical modelling that describes and explains the manifestation of these features that were observed in the experiment. Chapter 4 addresses the regime where a network of topological channels is formed in TBG. The chapter is devoted to investigating the electronic structure of small-angle TBG with a large potential asymmetry between the top and bottom layers where we also explain the origin of these emergent topological channels. This work was conducted at Osaka University under the Japan Society for the Promotion of Science Summer Programme. In Chapter 5, we consider umklapp electron-phonon interactions in TBG using an analytical method. We study a specific electron-phonon process where momentum is transferred to the superlattice when electrons tunnel from one layer to another layer; this work is also extended to TDBG. Finally, we conclude our findings in Chapter 6.

Chapter 2

Miniband spectra of twisted graphene heterostructures

Since the discovery of both superconductivity and insulating behaviour in twisted bilayer graphene [19, 10, 9, 20, 11], there has been an avalanche of research focused on twisted graphene systems. In twistronic systems, a relative twist between the crystallographic axes of neighbouring layers leads to the formation of a moiré interference pattern. Similar to the graphene/hBN superlattice, the additional spatial periodicity reduces the size of the Brillouin zone and a long-range periodic perturbation is created, which results in a strong modification of the electronic structure by the superlattice band folding [21, 22, 23, 24, 25, 12, 26, 27, 28, 29]. As the twist angle decreases, the superlattice unit cell increases in size. This means that the individual nature of the atoms can be neglected and the low-energy electronic band structure of the system can be described using a continuum model [21, 22, 12, 30, 27]. This chapter will introduce the continuum-model Hamiltonian used to describe twisted bilayer graphene and the resulting electronic miniband spectra. In addition, we generalise the model to describe twisted double bilayer graphene and twisted monolayer-bilayer graphene spectra.

2.1 Twisted bilayer graphene (TBG)

2.1.1 Continuum-model Hamiltonian

We calculate the electronic band structure of twisted bilayer graphene using a low-energy continuum model that is constructed using two Hamiltonian blocks from isolated monolayer graphene sheets and an interlayer off-diagonal tunnelling Hamiltonian block to describe the hopping between the two layers [21, 12, 26, 27, 31, 32, 33, 34]. For small-angle TBG, the Hamiltonian is a 4×4 matrix with the basis of atoms (A_1, B_1, A_2, B_2). It is given by

$$H_{\mathrm{TBG}} = \begin{pmatrix} H_{\mathrm{MLG}} & T \\ T^{\dagger} & H_{\mathrm{MLG}} \end{pmatrix} + V, \tag{2.1.1}$$

where

$$H_{\mathrm{MLG}} = \begin{pmatrix} 0 & -\upsilon\pi^{\dagger} \\ -\upsilon\pi & 0 \end{pmatrix}, \tag{2.1.2}$$

and

$$T = \sum_{j=0,1,2} e^{i(\boldsymbol{K}_{\xi}^{j} - \boldsymbol{K}_{\xi}^{0})\cdot \boldsymbol{r}_0} \begin{pmatrix} w_{\mathrm{AA}} & w_{\mathrm{AB}} e^{i\xi\frac{2\pi}{3}j} \\ w_{\mathrm{AB}} e^{-i\xi\frac{2\pi}{3}j} & w_{\mathrm{AA}} \end{pmatrix}. \tag{2.1.3}$$

The vectors $\boldsymbol{K}_{\xi}^{j}\,(j = 0, 1, 2)$ are three distinct Dirac points closest to the $\boldsymbol{\Gamma}$ point in the graphene Brillouin zone and are given by

$$\boldsymbol{K}_{\xi}^{j} = \xi\frac{4\pi}{3a}\Big[\cos\left(\frac{2\pi j}{3}\right), -\sin\left(\frac{2\pi j}{3}\right)\Big], \tag{2.1.4}$$

where the valley index $\xi = \pm 1$ is used to distinguish between K and K' valleys, and $a = 2.46$ Å is graphene's lattice constant. As a result of the moiré superlattice potential, the interlayer hybridisation has a periodic coordinate dependence. This is described by the two graphene layers laterally offset by $\boldsymbol{r}_0$ with respect to each other such that

the spatial modulation is described by $\boldsymbol{r}_0 = \theta\hat{\boldsymbol{z}} \times \boldsymbol{r}$, where $\hat{\boldsymbol{z}}$ is the unit vector in the perpendicular direction [34]. A unitary gauge transformation is applied to the Hamiltonian in Eq. (2.1.1) to establish common momentum coordinates in the system,

$$H_{\mathrm{TBG}} = U^{\dagger} H_{\mathrm{TBG}} U. \tag{2.1.5}$$

The wave vectors in both layers are measured relative to their Dirac points such that the original graphene Brillouin zones of the top and bottom layers are rotated by $\pm\Delta\boldsymbol{K}_{\xi}^{0}/2$,

$$U = \begin{pmatrix} e^{i\Delta\boldsymbol{K}_{\xi}^{0}\cdot\boldsymbol{r}/2}\mathbb{1} & 0 \\ 0 & e^{-i\Delta\boldsymbol{K}_{\xi}^{0}\cdot\boldsymbol{r}/2}\mathbb{1} \end{pmatrix}, \tag{2.1.6}$$

where $\mathbb{1}$ is the 2×2 identity matrix, and $\Delta\boldsymbol{K}_{\xi}^{0}$ is related to $\boldsymbol{K}_{\xi}^{0}$ by $\Delta\boldsymbol{K}_{\xi}^{j} = \theta\boldsymbol{z}\times\boldsymbol{K}_{\xi}^{j}$. After applying the gauge transformation and using the vector identity $\boldsymbol{a}\cdot(\boldsymbol{b}\times\boldsymbol{c}) = (\boldsymbol{a}\times\boldsymbol{b})\cdot\boldsymbol{c}$ with the definition of $\boldsymbol{r}_0$ to give the relation $\boldsymbol{K}_{\xi}^{j}\cdot\boldsymbol{r}_0 = -\Delta\boldsymbol{K}_{\xi}^{j}\cdot\boldsymbol{r}$, the off-diagonal interlayer matrix in Eq. (2.1.3) becomes

$$T = \sum_{j=0,1,2} e^{-\Delta\boldsymbol{K}_{\xi}^{j}\cdot\boldsymbol{r}} \begin{pmatrix} w_{\mathrm{AA}} & w_{\mathrm{AB}}e^{i\xi\frac{2\pi}{3}j} \\ w_{\mathrm{AB}}e^{-i\xi\frac{2\pi}{3}j} & w_{\mathrm{AA}} \end{pmatrix}. \tag{2.1.7}$$

We assume that the applied perpendicular electric field is constant, which gives the interlayer potential V as

$$V = \begin{pmatrix} \frac{\Delta}{2}\mathbb{1} & 0 \\ 0 & -\frac{\Delta}{2}\mathbb{1} \end{pmatrix}. \tag{2.1.8}$$

The on-diagonal blocks of the Hamiltonian in Eq. (2.1.1) describe the two graphene layers where $\pi = \hbar(\xi k_x + \mathrm{i}k_y)$. The parameter v is the band velocity of monolayer graphene where $\hbar v/a = 2.1354$ eV [31, 35], and Δ represents the electrostatic energy shift induced by the perpendicular electric field. The off-diagonal blocks describe the moiré interlayer coupling between the two twisted layers where we retain the hopping parameters from each site in layer 1 to the closest sites in layer 2. In addition, we use parameters $w_{\mathrm{AA}} = 0.0797$ eV and $w_{\mathrm{AB}} = 0.0975$ eV [35] to describe corrugation effects perpendicular to the plane, which enhances the gap between the lowest energy bands

and the excited bands [35, 36, 37]. The vectors $\Delta \boldsymbol{K}_{\xi}^{j}\,(j=0,1,2)$ account for the shift between the original Brillouin zone corners of the two graphene layers shown in Fig. 2.1 such that the original Dirac point of layer 1 is placed at the corner of the moiré Brillouin zone (mBZ) at κ and the original Dirac point of layer 2 is placed at κ' as illustrated in Fig. 2.1.

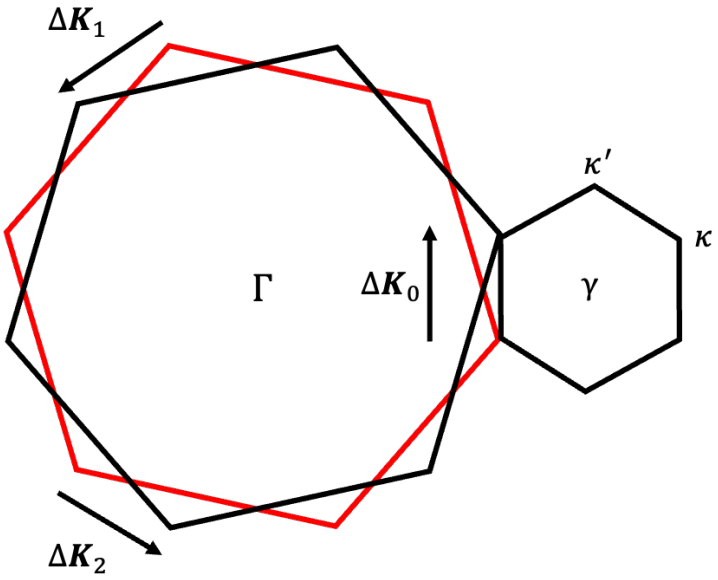

Figure 2.1: Brillouin zone of the two twisted graphene layers where the black and red hexagons are the original Brillouin zones of graphene layer 1 and layer 2 and they are overlaid with a relative twist. The vectors $\Delta \boldsymbol{K}_j$ $(j=1,2,3)$ account for the shift between the original Brillouin zone corners of the two graphene layers to make TBG.

2.1.2 Numerical procedure for band structures

To calculate the band structures, we must first construct the Hamiltonian that will be diagonalised. We take a basis of $\boldsymbol{k}$-states from both graphene layer 1 and 2, which are taken as

$$\begin{aligned}\boldsymbol{k}_{m_1,m_2}^{(1)} &= \boldsymbol{k} + \Delta \boldsymbol{K}_0 + m_1 \boldsymbol{G}_1 + m_2 \boldsymbol{G}_2 \\ \boldsymbol{k}_{m_1,m_2}^{(2)} &= \boldsymbol{k} - \Delta \boldsymbol{K}_0 + m_1 \boldsymbol{G}_1 + m_2 \boldsymbol{G}_2,\end{aligned} \tag{2.1.9}$$

respectively, where $\boldsymbol{k}$ is the wave vector in the first mBZ spanned by $\boldsymbol{G}_1$ and $\boldsymbol{G}_2$, where m_1 and m_2 are integers. Note that in the definitions of $\boldsymbol{k}_{m_1,m_2}^{(i)}$, we account for the twist angle by including a rotation matrix $R(\pm\theta/2)$, $\pm$ for $i=1$ and 2, respectively.

Let us take an example of TBG with twist angle $\theta = 5^\circ$, the minimum number of basis states needed such that the band structures are converged up to a cut-off energy of 1 eV when the Hamiltonian is numerically diagonalised is 24. The set of basis states comprises of two triangular sublattices where half of the states belong to graphene layer 1 and half of the states belong to graphene layer 2. This is illustrated in Fig. 2.2. More basis states are needed for smaller angles such that more orders of mBZs are included. For $\theta = 1^\circ$, basis states must include the 6th mBZ to converge the miniband spectra at low energies. Fig. 2.2 shows the basis states needed for $\theta = 5^\circ$ where the origin is the γ point, and the 6 basis states that are closest enclose a hexagon in which the area is the first mBZ. With 24 basis states, the full Hamiltonian is a 48×48 matrix as a result of zone folding. The on-diagonal is comprised of 24 alternating 2×2 matrices describing the isolated monolayer graphene sheets on layer 1 and layer 2, respectively, as shown in Eq. 2.1.2. The off-diagonal of the Hamiltonian is comprised of the interlayer tunnelling Hamiltonian blocks in Eq. (2.1.3) between every basis $\boldsymbol{k}$-state in layer 1 with every basis $\boldsymbol{k}$-state on layer 2. In other words, we use zone folding to bring the states in each valley with momenta connected by the moiré reciprocal lattice vectors, $\boldsymbol{G}_1 = \Delta\boldsymbol{K}_1 - \Delta\boldsymbol{K}_0$ and $\boldsymbol{G}_2 = \Delta\boldsymbol{K}_2 - \Delta\boldsymbol{K}_0$, from the second mBZs into the first mBZ.

To find the 3D band structure, we first create a mesh of states to cover the first mBZ. For each state in the mBZ, we apply the full Hamiltonian and numerically diagonalise the matrix to find the eigenvalues for that particular state. Note that we calculate the energy spectra for the K and K' valleys independently because the intervalley coupling is negligible at small twist angles as a result of the long-wavelength superlattice period. The electronic spectra for the two valleys are connected by a π-rotation, and this is as a result of the connected triangular sublattices that are related by a π-rotation.

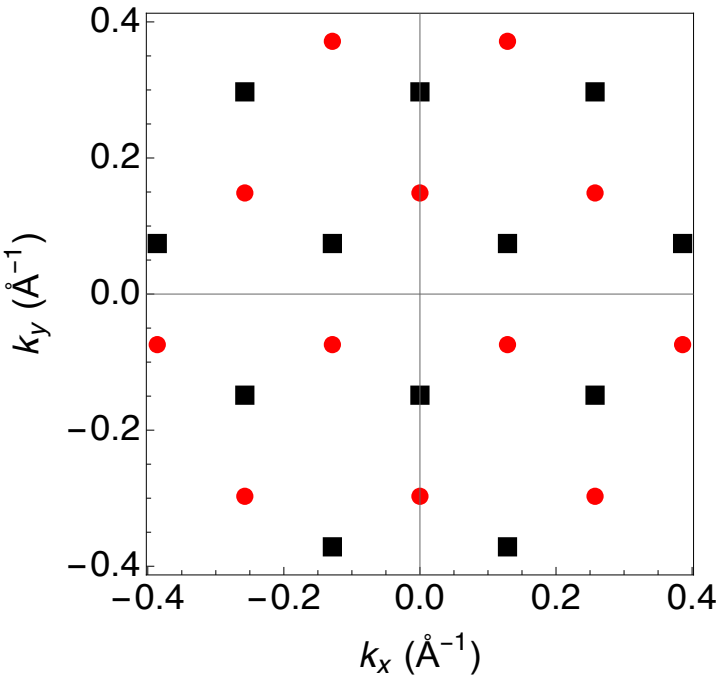

Figure 2.2: The set of basis $\boldsymbol{k}$-states needed to construct the full Hamiltonian for $\theta = 5°$ twisted bilayer graphene. The origin is the γ point of the first mBZ. The black and red states belong to graphene layers 1 and 2, respectively.

2.1.3 Band structures with no electric field

Varying the relative twist angle between the two layers in TBG affects not only the wavelength of the moiré pattern but also the strength of the interlayer coupling between the layers. At larger twist angles, the two graphene layers are almost decoupled such that the low-energy spectrum of the TBG system for a given valley exhibits two Dirac cones where one cone belongs to one graphene layer and one cone belongs to the second graphene layer. As we decrease the twist angle, the interlayer coupling between the two graphene layers causes the Dirac cones to hybridise, and the Fermi velocity of the Dirac cones renormalises and decreases further [12]. The presence of the Dirac points means that at charge neutrality, there is a zero density of states. In addition, a feature of the TBG spectra is the presence of van Hove singularities in the first conduction and valence bands, which emerge between the Dirac points. Figure 1.2 presents the three-dimensional electronic spectra for TBG at various twist angles, $\theta = 5°, 2.5°$ and $1.05°$ of K-valley bands with no perpendicular electric field, $\Delta = 0$. At an angle $\theta \approx 1.05°$, the velocity at the Dirac point vanishes and the bands at the Fermi energy are flattened.

The TBG band structure exhibits electron-hole symmetry and this is clearly seen in Fig. 2.4 where the electronic spectra for varying twist angles are shown along the path $\kappa \to \gamma \to \mu \to \kappa'$ for both the K (black) and K' (red) valleys. In agreement with previous works on the electronic spectra of TBG, the flattening of the lowest energy bands is not monotonous with decreasing twist angle as we can see that the bands are less flat for $\theta = 0.9°$ [12].

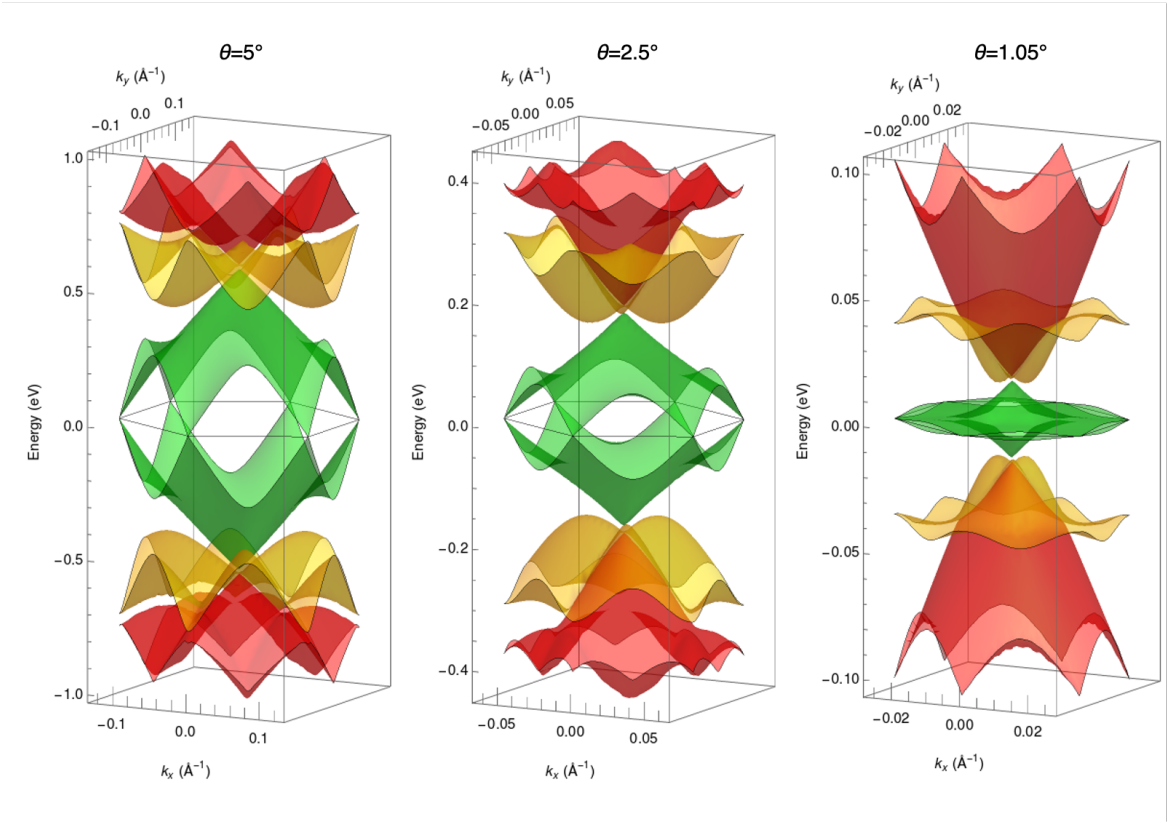

Figure 2.3: Three-dimensional twisted bilayer graphene band structures calculated for twist angles $\theta = 5°, 2.5°$ and $1.05°$ at the K valley with zero displacement field. The outline of the hexagon is the moiré Brillouin zone where the γ point is at the centre of the hexagon. The band structures exhibit Dirac cones characteristic of the low-energy electronic spectrum of graphene such that each non-identical cone belongs to each graphene layer. As the twist angle decreases, the Fermi velocity of the Dirac cones decreases and at the magic angle $1.05°$, the first conduction and valence bands are flattened.

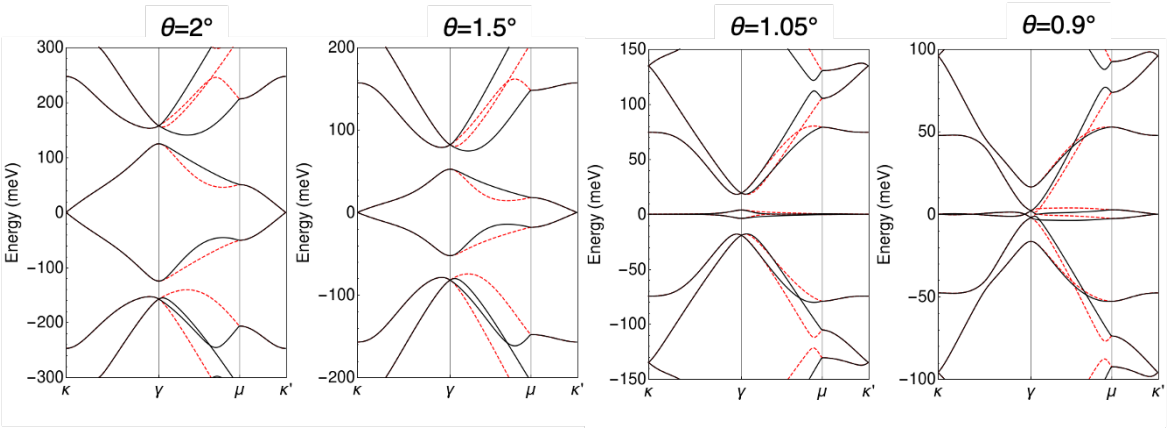

Figure 2.4: Twisted bilayer graphene band structures calculated for twist angles $\theta = 2°, 1.5°$, $1.05°$ and $0.9°$ with zero displacement field. The black and red lines are the band structures calculated for the K and K' valleys, respectively.

2.1.4 Band structures with an electric field

A displacement field results in an on-site energy difference between the top and bottom layers of graphene, respectively. Figure 2.5 illustrates the three-dimensional band structures for different displacement fields for $\theta = 2.5°$ in the K valley. The displacement field breaks the layer symmetry and we see that the energies of the low-energy bands that touch at the Dirac points, κ and κ', are shifted upwards and downwards relative to each other. The energy shifts are proportional to the applied displacement field. The result of this relative shift is that there is no longer a zero density of states at charge neutrality. Figure 2.6 shows the band structures of TBG at $\theta = 2.5°$ and varying Δ for both the K (black) and K' (red) valleys. We see that electron-hole symmetry is preserved and the band structures in each valley is a π-rotation from each other as the minivalleys at κ and κ' are shifted in opposite directions for opposite valleys.

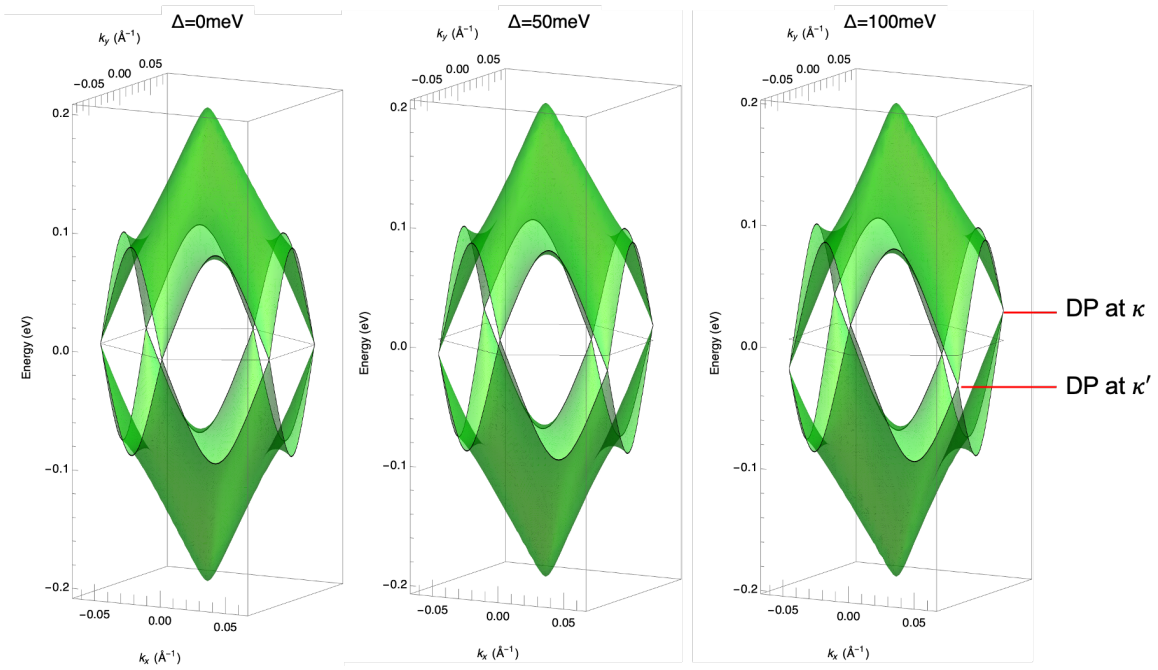

Figure 2.5: Three-dimensional band structures of K-valley bands for TBG at $\theta = 2.5°$ for varying Δ. The finite displacement field breaks the layer symmetry of the minivalleys such that Dirac points in the κ and κ' minivalleys shift upwards and downwards, respectively, meaning there is a non-zero density of states at charge neutrality.

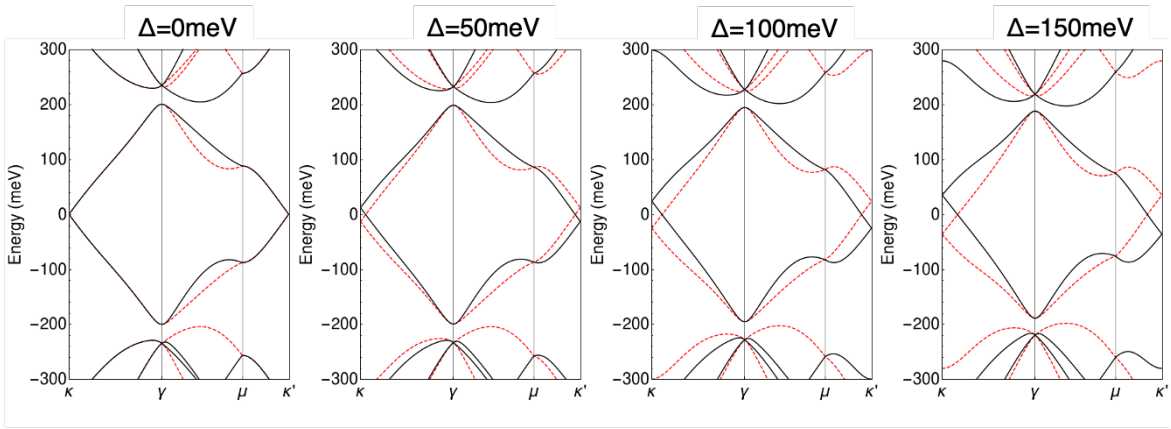

Figure 2.6: Calculated band structures for twisted bilayer graphene at twist angle $\theta = 2.5°$ for varying Δ plotted for the K (black) and K' (red) valleys.

2.2 Twisted double bilayer graphene (TDBG)

Recently reported experimental observations of superconductivity, tunable correlated states and topologically non-trivial phases in twisted double bilayer graphene (TDBG) systems have garnered huge interest amongst researchers [38, 39, 40, 41]. There

is an emerging number of theoretical studies related to the electronic properties of these systems to understand the TDBG band structure in the single-particle picture [42, 43, 44, 45, 46, 47]. In this section, we extend the continuum-model Hamiltonian used in TBG and present the electronic band structures for TDBG.

Twisted double bilayer graphene is two bilayer graphene systems stacked on top of each other with an in-plane relative twist between the two bilayers where each bilayer graphene is Bernal-stacked, i.e. in the AB stacking arrangement. Here, we present two configurations of TDBG, both AB-AB and AB-BA stacking. In addition, we employ both the minimal and full parameter model of each bilayer graphene using the continuum-model Hamiltonian and compare the band structures in the absence of and with a perpendicular electric field.

2.2.1 Continuum-model Hamiltonian

We calculate the electronic band structure of TDBG by adapting the continuum-model approach for twisted bilayer graphene in Eq. (2.1.1). The Hamiltonian is a 8×8 matrix with the basis of atoms $(A_1, B_1, A_2, B_2, A_3, B_3, A_4, B_4)$, and the AB-AB stacking Hamiltonian is given by

$$H_{\mathrm{TDBG}} = \begin{pmatrix} H_{\mathrm{BLG}} & T \\ T^{\dagger} & H_{\mathrm{BLG}} \end{pmatrix} + V, \tag{2.2.1}$$

where

$$H_{BLG} = \begin{pmatrix} 0 & -\upsilon\pi^{\dagger} & \upsilon_4\pi^{\dagger} & \upsilon_3\pi \\ -\upsilon\pi & \Delta' & \gamma_1 & \upsilon_4\pi^{\dagger} \\ \upsilon_4\pi & \gamma_1 & \Delta' & -\upsilon\pi^{\dagger} \\ \upsilon_3\pi^{\dagger} & \upsilon_4\pi & -\upsilon\pi & 0 \end{pmatrix} \tag{2.2.2}$$

and

$$T = \begin{pmatrix} \mathbf{0} & \mathbf{0} \\ \sum_{j=0,1,2} e^{-i\Delta \boldsymbol{K}_\xi^j \cdot \boldsymbol{r}} \begin{pmatrix} w_{\mathrm{AA}} & w_{\mathrm{AB}} e^{i\xi \frac{2\pi}{3} j} \\ w_{\mathrm{AB}} e^{-i\xi \frac{2\pi}{3} j} & w_{\mathrm{AA}} \end{pmatrix} & \mathbf{0} \end{pmatrix}, \tag{2.2.3}$$

where $\mathbf{0}$ is the 2×2 zero matrix. We assume that the applied perpendicular electric field is constant giving the interlayer potential V as

$$V = \begin{pmatrix} \frac{3}{2}\Delta\mathbb{1} & & & \\ & \frac{1}{2}\Delta\mathbb{1} & & \\ & & -\frac{1}{2}\Delta\mathbb{1} & \\ & & & -\frac{3}{2}\Delta\mathbb{1} \end{pmatrix}, \tag{2.2.4}$$

where $\mathbb{1}$ is the 2×2 identity matrix and Δ represents the electrostatic energy shift induced by the perpendicular electric field between adjacent layers. The same parameters are used for the band velocity of monolayer graphene and the values of w_{AA} and w_{AB} are the same as the values used for TBG in section 2.1.1. Within each bilayer graphene, the vertical interlayer coupling between dimer sites is $\gamma_1 = 0.4$ eV, the interlayer coupling between non-dimer sites is related to υ_3 and the interlayer coupling between dimer and non-dimer sites is related to υ_4. The relation used is $v_i = (\sqrt{3}/2)\gamma_i a/\hbar$ for $i = 3, 4$ where $\gamma_3 = 0.32$ eV and $\gamma_4 = 0.44$ eV [48]. In addition, the energy difference between the dimer and non-dimer sites is given by $\Delta' = 0.05$ eV [48]. To obtain the AB-BA TDBG Hamiltonian, we interchange the matrix elements so that the basis of atoms is $(A_1, B_1, A_2, B_2, A_4, B_4, A_3, B_3)$ in relation to the AB-AB TDBG Hamiltonian. We numerically diagonalise the continuum-model Hamiltonian using the zone folding method discussed for TBG to obtain the miniband spectra. Note that in this section we use the parameters used in Ref. [42] to produce similar band structures that are also in agreement with Ref. [41].

2.2.2 Minimal model

To calculate the low-energy band structure of TDBG, we first consider a minimal model for each individual bilayer by including only γ_1, w_{AA} and w_{AB}. We exclude the rotation matrix $R(\pm\theta/2)$ and neglect the relatively small parameters by setting $\upsilon_3, \upsilon_4, \Delta' = 0$. Without the presence of υ_4 and Δ', both the band structures for AB-AB and AB-BA configurations exhibit an artificial electron-hole symmetry. This holds true even in the presence of a constant perpendicular electric field. Figures 2.7a and 2.7b show the calculated band structures for $\theta = 1.3°$ with $\Delta = 0, 10, 20$ and 30 meV for both AB-AB and AB-BA configurations using the minimal parameter model for both the K (black) and K' (red) valleys. The band structures for AB-AB and AB-BA TDBG using the minimal parameter model are comparable. Similar to the TBG band structure where the electronic spectra exhibit two non-equivalent Dirac points, one from each graphene layer, the original parabolic dispersion of bilayer 1 is placed at the corner of the mBZ at κ and the original parabolic dispersion of bilayer 2 is placed at κ'.

In Fig. 2.7, these parabolic dispersions are seen at the minivalleys in the absence of a perpendicular electric field. Similar to the TBG band structures, the parameters w_{AA} and w_{AB} account for corrugation and the lowest energy bands are well-separated from the excited bands. When an asymmetric interlayer potential V is applied, the low-energy degenerate bands split and a gap is opened at the charge neutrality point for both configurations of TDBG. Unlike in TBG where an applied electric field preserves the Dirac points, the gap opening in TDBG is perhaps unsurprising as single bilayer graphene also exhibits a band opening in the presence of a perpendicular electric field. As we increase Δ, the low-energy conduction and valence bands separate further.

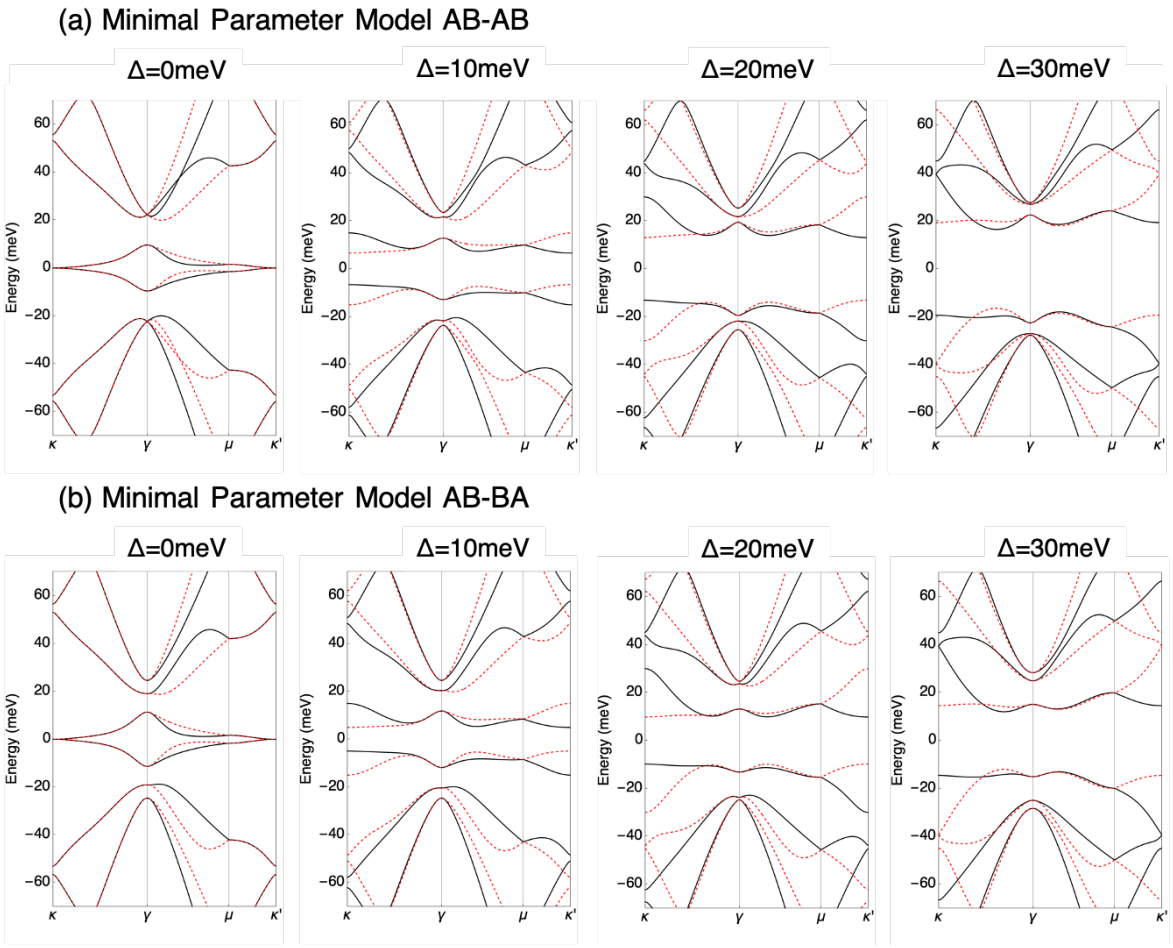

Figure 2.7: (a) Band structures for AB-AB TDBG at $\theta = 1.3°$ with $\Delta = 0, 10, 20$ and 30 meV, calculated using the minimal parameter model. Black and red lines are spectra for the K and K' valleys, respectively. (b) Corresponding plots for AB-BA TDBG.

Figure 2.8 shows the TDBG band structures calculated using the minimal parameter model for various twist angles with $\Delta = 0$. Similar to the TBG band structures, as the twist angle decreases, the bandwidth of the lowest energy bands decreases and the number of bands in a given energy window increases. For both AB-AB and AB-BA stacking configurations, flat bands that are isolated from the excited bands are observed at the magic angle, $\theta = 1.05°$. Notably, for comparable angles, the bandwidths of the low-energy bands in TDBG are approximately half of those exhibited in TBG. This suggests that TDBG could be an interesting prospect for generating narrow bandwidth flat bands in an experiment.

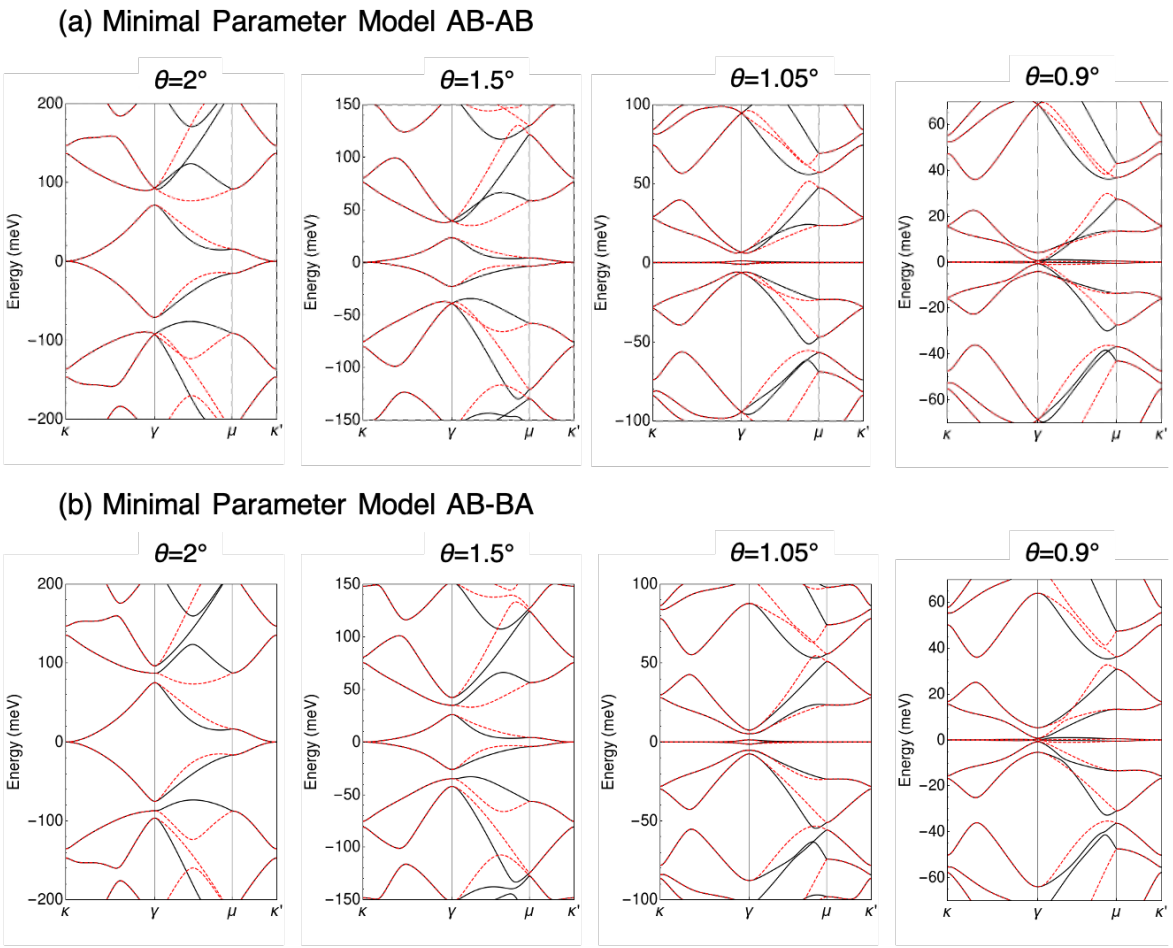

Figure 2.8: (a) TDBG band structures for various twist angles, $\theta = 2°, 1.5°, 1.05°$ and $0.9°$, calculated using the minimal parameter model for AB-AB configuration with $\Delta = 0$. The red and black lines correspond to the bands for the K and K' valley, respectively. (b) Corresponding plots for AB-BA TDBG. In both configurations, isolated flat bands are observed at $1.05°$.

2.2.3 Full parameter model

Implementing the additional parameters causes significant changes to the low-energy band structure of TDBG. Figure 2.9 shows the calculated TDBG band structures using the full parameter model for twist angle $\theta = 1.3°$ and varying Δ for AB-AB and AB-BA configurations. The v_3 term gives rise to trigonal warping leading to the broadening of the low-energy bands. This is consistent with the effect of trigonal warping in single bilayer graphene where the range of band touching points is widened. In the presence of v_4 and Δ', the artificial electron-hole symmetry observed in the minimal model band structures is broken. As Δ increases, the bandwidth of the first conduction band decreases whilst the bandwidth of the first valence band increases and becomes more

dispersed. In both TDBG configurations, the first conduction band is relatively flat and isolated from the other bands. As a result, the band gaps separating the lowest energy bands from the excited bands on the electron side is greater than that of the hole side. Experimental findings show that a correlated insulating phase is only observed on the electron-doping side, which is in agreement with the broken electron-hole symmetry in theoretical calculations [41]. At $\theta = 1.3°$ and $\Delta = 0$ meV, there are overlapping bands at charge neutrality, which is consistent with metallic behaviour. As Δ increases, the low-energy bands become increasingly separated and no longer overlap.

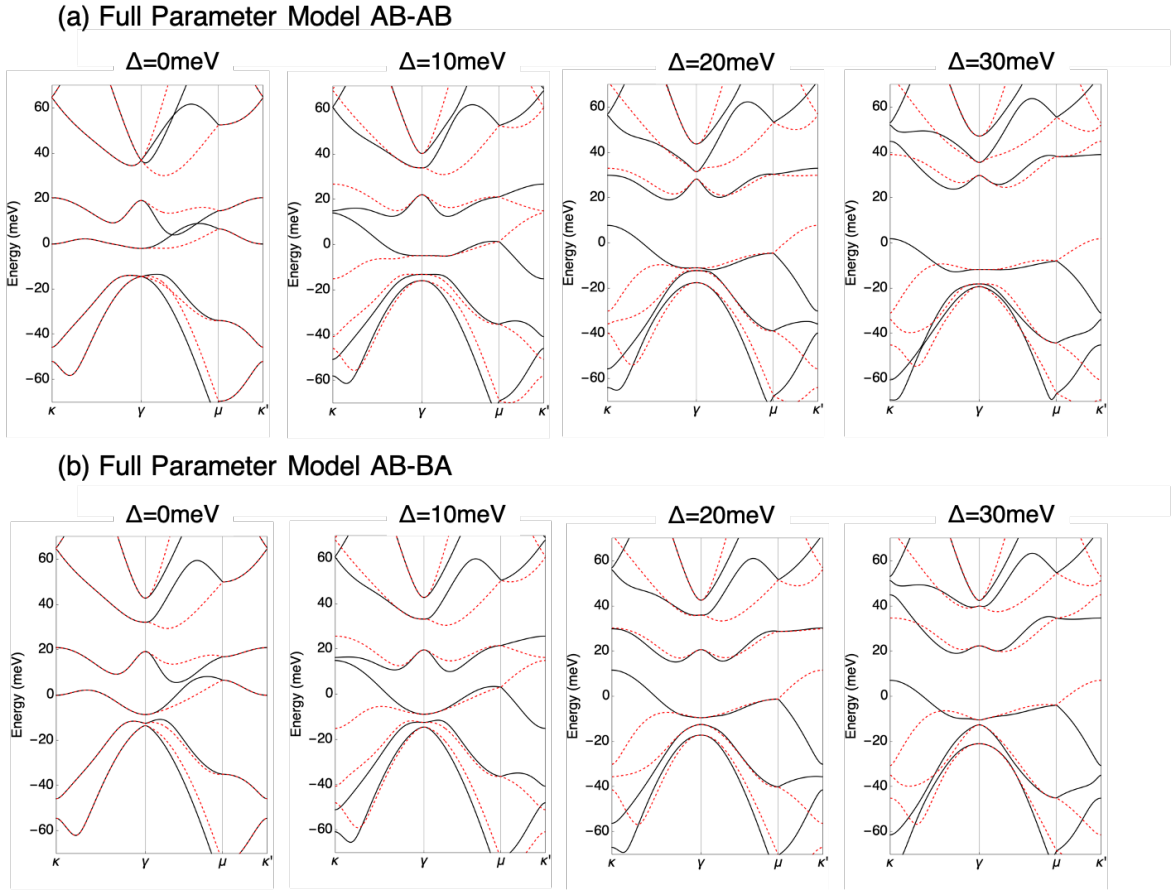

Figure 2.9: (a) Band structures for AB-AB TDBG at $\theta = 1.3°$ with $\Delta = 0, 10, 20$ and 30 meV, calculated using the full parameter model. Black and red lines are spectra for the K and K' valleys, respectively. (b) Corresponding plots for AB-BA TDBG.

Figure 2.10 shows the TDBG band structures for twist angles $\theta = 2°, 1.5°, 1.05°$ and $0.9°$. At the magic angle $\theta = 1.05°$, the low-energy bands are dispersed and there are no longer flat bands as was observed in the minimal parameter model band structures. At a relatively large angle of $\theta = 2°$, there is a band gap at the charge neutrality point, and as the twist angle decreases, the lowest energy bands begin to overlap. The four-fold

spin and valley degeneracy means that each moiré miniband has a filling factor of four electrons or holes per moiré superlattice cell area. For both TDBG configurations, Fig. 2.10 shows that there is an insulating gap between the third and the fourth valence bands for $\theta = 1.05°$ and $0.9°$. The calculated band structures are consistent with the experiment where AB-AB stacked TDBG is shown to exhibit insulating gaps at filling factors where four and twelve electrons and holes fill a moiré superlattice unit cell for devices with twist angles $\theta = 1.26°, 1.28°$ and $1.33°$ [39].

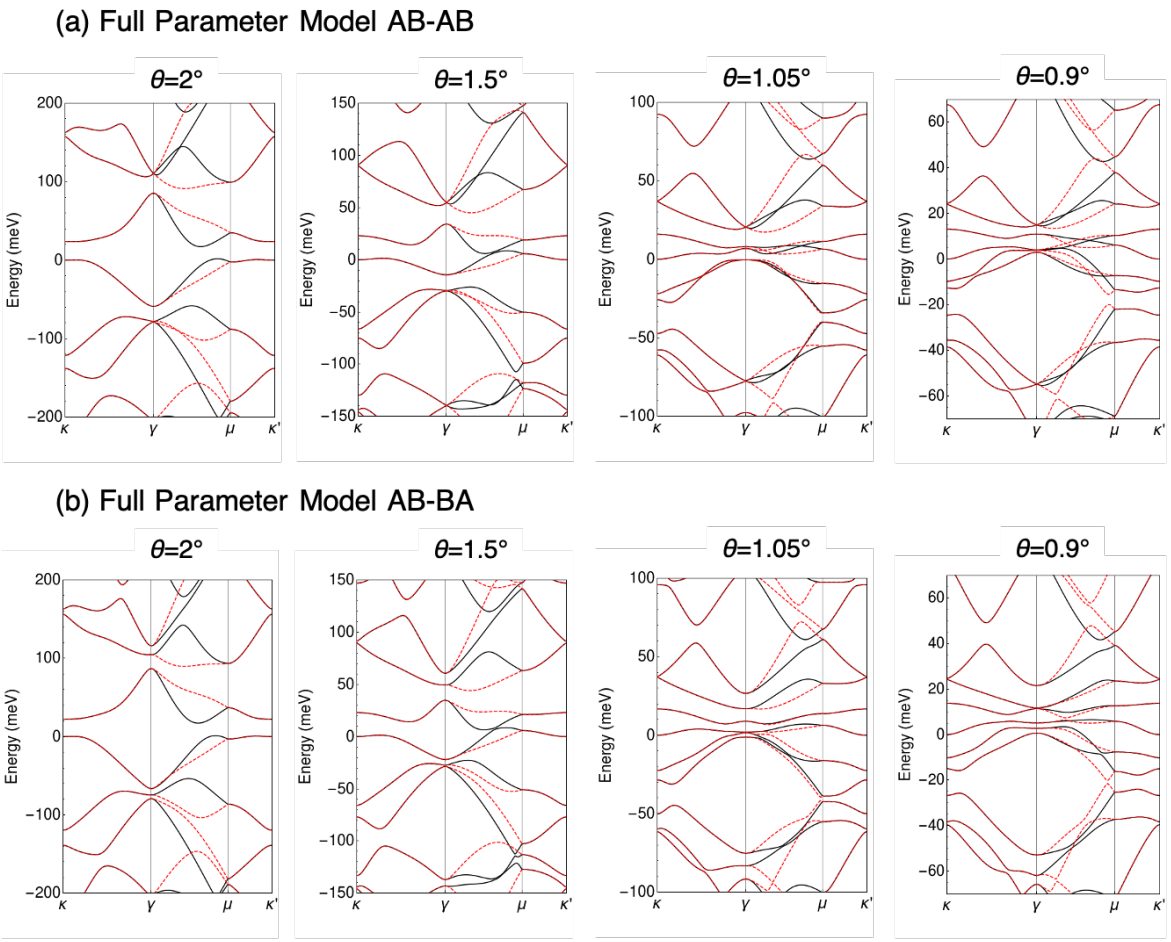

Figure 2.10: TDBG band structures for various twist angles, $\theta = 2°, 1.5°, 1.05°$ and $0.9°$, calculated using the full parameter model for AB-AB configuration with $\Delta = 0$. The red and black lines correspond to the bands for the K and K' valley, respectively. (b) Corresponding plots for AB-BA TDBG. In both configurations, the isolated flat bands observed in the minimal model at $1.05°$ are no longer present.

2.3 Twisted monolayer-bilayer graphene (TMBG)

Compared to TBG, there are more tuning parameters in twisted monolayer-bilayer graphene (TMBG) because the band structures in multilayer graphene are more tunable than monolayer band structures [49, 50, 51, 52]. In this section, we extend the continuum-model Hamiltonian to TMBG where bilayer graphene is stacked on top of monolayer graphene and we show a couple of band structures to highlight how the continuum model can be generalised to study and understand emergent phenomena in the field of twistronics.

2.3.1 Continuum-model Hamiltonian

To calculate the band structures for TMBG, we employ the continuum-model Hamiltonian following the method used for TBG and TDBG in the previous sections. The Hamiltonian is a hybrid of the twisted bilayer graphene and twisted double bilayer graphene Hamiltonians such that one on-diagonal block of the matrix is the Dirac Hamiltonian for monolayer graphene and the other on-diagonal block is that for bilayer graphene. These blocks are coupled by 2×4 off-diagonal tunnelling matrices to couple the two systems. The resulting Hamiltonian is a 6×6 matrix given by

$$H_{\mathrm{TMBG}} = \begin{pmatrix} H_{\mathrm{MLG}} & T \\ T^{\dagger} & H_{\mathrm{BLG}} \end{pmatrix} + V, \tag{2.3.1}$$

where

$$T = \sum_{j=0,1,2} e^{-i\Delta \boldsymbol{K}_{\xi}^{j} \cdot \boldsymbol{r}} \begin{pmatrix} w_{\mathrm{AA}} & w_{\mathrm{AB}} e^{i\xi \frac{2\pi}{3} j} & 0 & 0 \\ w_{\mathrm{AB}} e^{-i\xi \frac{2\pi}{3} j} & w_{\mathrm{AA}} & 0 & 0 \end{pmatrix}. \tag{2.3.2}$$

The on-diagonal blocks H_{MLG} and H_{BLG} are defined in Eqs. (2.1.2) and (2.2.2), respectively. Using the same approach as in TBG and TDBG, the perpendicular electric field is assumed to be constant and pointing from the monolayer to the bilayer. Here, the interlayer potential is given by $V = \mathrm{diag}(-\Delta/2, -\Delta/2, 0, 0, \Delta/2, \Delta/2)$.

2.3.2 Band structures

For a large twist angle of $\theta = 5^\circ$, the low-energy spectrum is as though the monolayer and the bilayer are decoupled. This results in the band structure exhibiting a Dirac cone from the monolayer and a parabolic dispersion from the bilayer at each minivalley. This is illustrated in Fig. 2.11a where we see band touching points at charge neutrality. Similar to TDBG, the band structures exhibit electron-hole asymmetry. For smaller twist angles, the interlayer coupling between the monolayer and bilayer causes the Dirac point to shift to positive energy, which we denote as E_{DS}, even in the absence of a perpendicular electric field. Figure 2.11b shows the TMBG band structure for $\theta = 1.22^\circ$ with $\Delta = 0$ meV. We see that the lowest energy bands are well separated from the excited bands. In the experiment published in our paper, this is observed as two single-particle gaps at full fillings where four electrons and holes occupy the first conduction and valence bands and thus, gives rise to band insulators [53]. With the addition of an asymmetric interlayer potential as shown in Fig. 2.11c, the degeneracies at the κ and κ' minivalleys are broken and a band gap at charge neutrality emerges, which is observed as the increase in resistivity in the experiment. Also, the first conduction band is much flatter than the first valence band. We also note that the band gap between the first conduction band and the second conduction band decreases in size with the addition of a perpendicular electric field whereas the gap on the valence band side between the first and second bands decreases slightly.

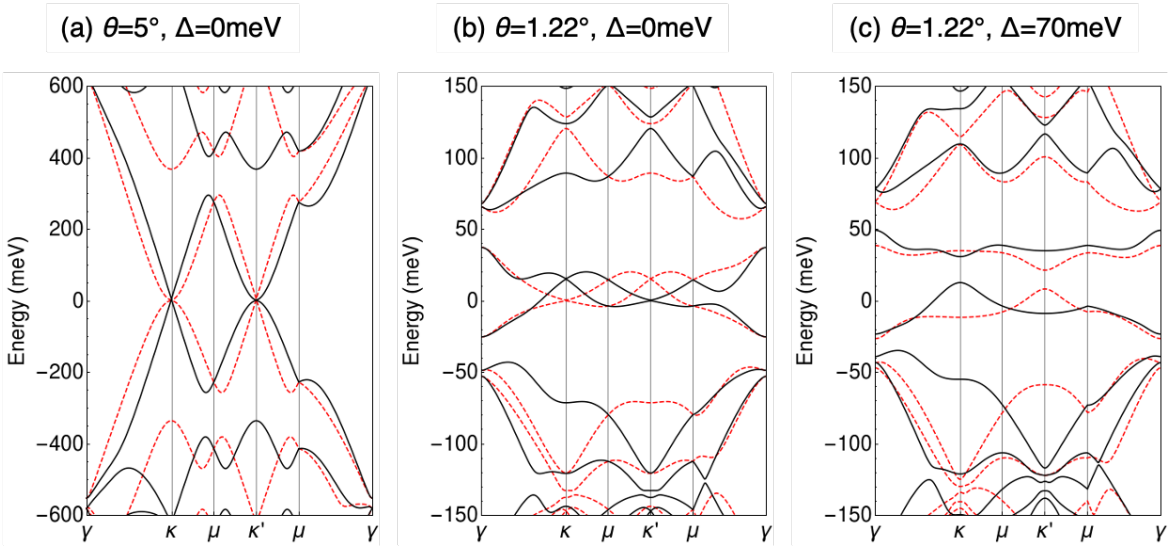

Figure 2.11: (a) Calculated band structure for TMBG for $\theta = 5°$ and $\Delta = 0$ meV. (b)(c) Calculated band structures for $\theta = 1.22°$ with no potential energy difference between the top and the bottom layer of TMBG and with a potential difference of $\Delta = 70$ meV, respectively. Red and black correspond to the K and the K' valleys, respectively.

Figure 2.12 shows the shift of the Dirac point energy with respect to zero energy, E_{DS}, as a function of the twist angle. For all twist angles, the Dirac energy shift originating from the monolayer is always shifted upwards compared to the electronic states originating from the bilayer regardless of the sign of the applied perpendicular electric field [53].

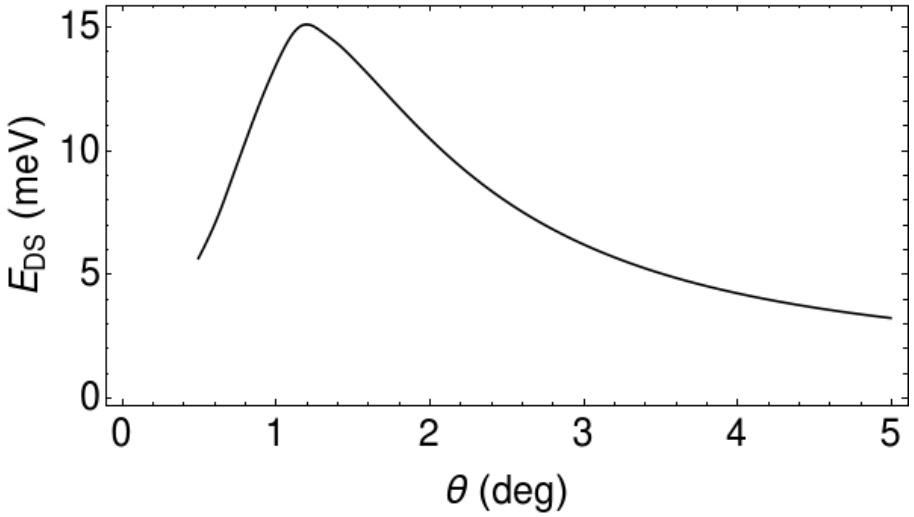

Figure 2.12: Dirac energy shift E_{DS} as a function of twist angle calculated using the continuum model. The results are comparable to the results obtained using the tight-binding model in Ref. [54].

Chapter 3

Transverse magnetic focusing (TMF) of twisted bilayer graphene

Transverse magnetic focusing (TMF) is a powerful experimental technique that uses a weak transverse magnetic field to focus charge carriers onto a detector over a scale of microns [55, 56, 57, 58, 59, 60]. Electrons can move ballistically and propagate over macroscopic distances in periodic lattices without scattering, and this phenomenon has enabled the use of TMF to be used to study the shape of the Fermi surface of metals [61], semiconductor heterostructures, as well as two-dimensional materials such as graphene [60].

The concept of TMF can be understood by considering electrons injected into a two-dimensional system via a narrow contact. Magnetic fields force these ballistic electrons to propagate along skipping orbits along the boundary of the material where the skipping trajectories converge to form caustics. This leads to pronounced resistance peaks at nearby voltage probes as electrons are focused onto the detector. This technique is analogous to charge mass spectroscopy and can be used to study the electronic structure of metals as well as to demonstrate ballistic transport.

In this chapter, we present the use of magnetic focusing to probe the band structure of twisted bilayer graphene with a twist angle of $\sim 2°$. This research was completed in collaboration with Alexey Berdyugin at the University of Manchester who conducted the experiments. The following will present the experimental data along with the supporting theoretical work and will use notation and conventions that are aligned with

our published paper [18]. We found that the minibands in TBG support long-range ballistic transport limited at low temperatures by intrinsic electron-electron scattering. In addition, applying a voltage bias between the layers causes strong minivalley splitting, which allows selective focusing of electron trajectories from different minivalleys and hence, of interest for using this degree of freedom in the field of valleytronics.

In section 2.1, we showed that at larger angles, the TBG spectrum corresponds to a metal with several minibands at each K and K' valley of the original graphene Brillouin zones. The twist angle between the two graphene layers modifies the electronic spectra by the presence of the long-range interference pattern with a moiré period that we denote λ_s in this chapter, which is illustrated in Fig. 3.1a. It is expected that the electronic properties of such a metal are different from the behaviour of Dirac electrons in monolayer or Bernal-stacked bilayer graphene and this research probes the electronic properties of TBG in more detail and, in particular, the behaviour of the lowest energy minibands where the secondary Dirac points are present, as illustrated in Fig. 3.1b where the band structure is computed using the continuum-model Hamiltonian described in section 2.1. We present the experimental manifestation of the TMF of electrons in a perpendicular magnetic field explained using theoretical analysis to probe the properties of moiré minibands in TBG. In addition, we use a vertical displacement field, D, to break valley degeneracy between the two constituent graphene layers and show that we can selectively enhance transport in one of the minivalleys.

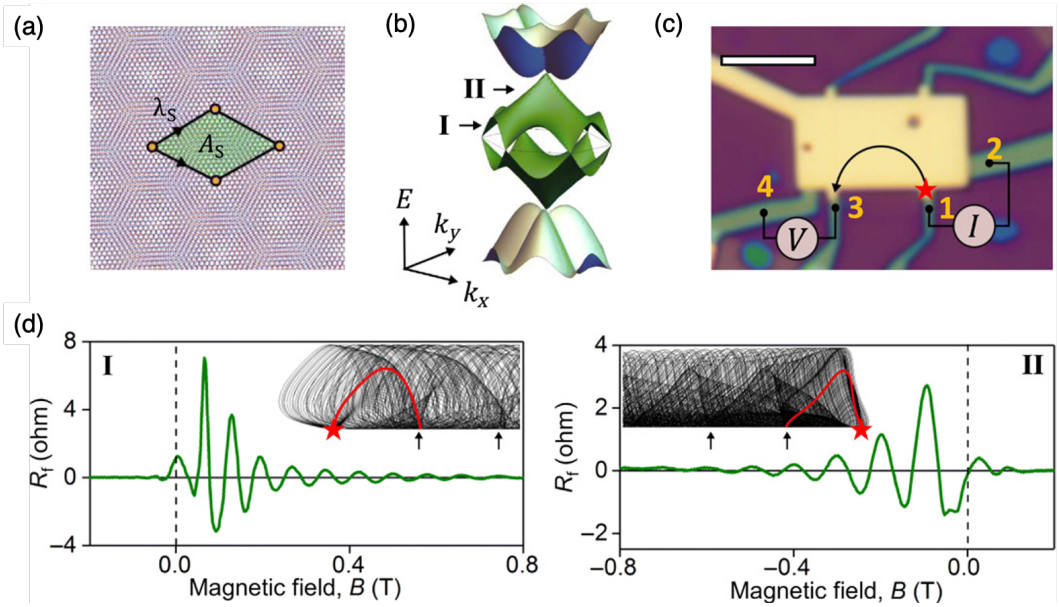

Figure 3.1: (a) Schematics of the moiré superlattice induced by the twist of graphene layers. Here, two graphene sheets are rotated by an angle θ relative to each other, which creates an additional spatial periodicity $\lambda_s = a/[2sin(\theta/2)]$ (a is graphene's lattice constant) with the unit cell area of $A_S = \sqrt{3}/2\lambda_S^2$. (b) Band structure of TBG graphene in the K valley of the Brillouin zone calculated for the twist angle $\theta = 1.87°$. (c) Optical image of TBG device D1 with $\theta = 1.87°$. Scale bar, 4 μm. (d) Two examples of TMF signals measured in device D2 ($D = 0$ Vnm^{-1}) at 5 K for the carrier density 3.7×10^{12} cm^{-2} (left) and 9.3×10^{12} cm^{-2} (right) at a distance of 4.9 μm from the injector. The latter is close to the main and secondary neutrality points, respectively, as illustrated in (b). The insets are examples of focusing caustics near the main (left) and secondary (right) neutrality points. Arrows highlight the focal points for caustics, red star marks the current injection point, and red lines show typical trajectories that extend from the injector to the first focal point.

3.1 Equations of motion and TMF

To model transverse magnetic focusing, we first establish a connection between the miniband dispersion, $\epsilon(\boldsymbol{k})$, and the transport properties using the equations of motion for an electron in an out-of-plane magnetic field, $\boldsymbol{B} = B\hat{\boldsymbol{z}}$,

$$\dot{\boldsymbol{k}} = -e\boldsymbol{v}(\boldsymbol{k}) \times \boldsymbol{B}, \quad \dot{\boldsymbol{r}} = \boldsymbol{v}(\boldsymbol{k}), \quad \boldsymbol{v}(\boldsymbol{k}) = \frac{\partial\epsilon(\boldsymbol{k})}{\partial(\boldsymbol{k})}. \tag{3.1.1}$$

The equations of motion show that energy is conserved and that the velocity is always perpendicular to the dispersion. This means that the orbit in real space can be obtained from the orbit in reciprocal space by rotating by 90° and scaling by $1/eB$. The equations

above follow from [62],

$$\dot{\boldsymbol{r}} = \frac{\partial \epsilon(\boldsymbol{k})}{\hbar \partial \boldsymbol{k}} - \dot{\boldsymbol{k}} \times \boldsymbol{\Omega}(\boldsymbol{k}), \quad \hbar \dot{\boldsymbol{k}} = -e\boldsymbol{E} - e\dot{\boldsymbol{r}} \times \boldsymbol{B} \tag{3.1.2}$$

where $\boldsymbol{\Omega}(\boldsymbol{k})$ is the Berry curvature for the two-dimensional system [63]. To obtain Eq. (3.1.1), we set $\hbar = 1$ and take $\boldsymbol{E} = 0$ so that the equations can be rewritten as,

$$\dot{\boldsymbol{k}}(1 + e\boldsymbol{B} \cdot \boldsymbol{\Omega}(\boldsymbol{k})) = -e\frac{\partial \epsilon(\boldsymbol{k})}{\partial \boldsymbol{k}} \times \boldsymbol{B}, \quad \dot{\boldsymbol{r}}(1 + e\boldsymbol{B} \cdot \boldsymbol{\Omega}(\boldsymbol{k})) = \frac{\partial \epsilon(\boldsymbol{k})}{\partial \boldsymbol{k}}. \tag{3.1.3}$$

From this, it follows that the Berry curvature only affects the speed at which the electron trajectory is traversed but not the shape of the orbit. Consequently, we take $\boldsymbol{\Omega}(\boldsymbol{k}) = 0$ to give Eq. (3.1.1).

To simulate transverse magnetic focusing (TMF) maps, we first calculate the band structures to extract the Fermi surfaces according to the miniband dispersion $\epsilon(\boldsymbol{k})$ and then determine the cyclotron orbits in real space by rotating the orbits in reciprocal space by a 90° rotation and scaling by $1/eB$ according to Eq. (3.1.1). The sign of the effective charge influences whether the charge carrier propagates in the clockwise or anticlockwise direction. We assume specular boundary conditions so that in a magnetic field the carriers travel along the edge of the sample following cyclotron (skipping) orbits and caustics of skipping orbits focus onto equidistant points. The drift direction of the skipping orbits depends on the effective charge of the carriers and the directions of the magnetic field. To achieve consistency with the experiment we select the states that are moving away from the injection point with energies between ϵ_{F} and $\epsilon_{\mathrm{F}} + eV$. The Fermi energy and applied voltage is denoted by ϵ_{F} and V, respectively. The group velocity is calculated from the band structure using $\boldsymbol{v} \propto \nabla_{\boldsymbol{k}} \epsilon(\boldsymbol{k})$. In other words, the group velocity is related to the energy dispersion, for example, the velocity is smaller in flatter parts of the dispersion. Accordingly, as the applied voltage elevates the Fermi level, it results in extra states being occupied such that the available states are populated with a probability proportional to $|\nabla_{\boldsymbol{k}} \epsilon(\boldsymbol{k})|^{-1}$ and different injection angles are weighted with a probability proportional to the density of states.

The TMF spectra are calculated numerically by using a similar method to Ref.

[55]. This is achieved by counting how many electrons enter contact 3 in Fig. 3.1c with a finite width w. The non-local resistance $R_f = (V_3 - V_4)/I_1$ is then found by calculating $(N_3 - N_4)/N_1$, where N_1 is the total number of injected electrons, N_3 is the number of electrons entering contact 3 and N_4 is a smooth background given by $N_4 = \sum_{\mathrm{i}}^{N_1} w/d_{\mathrm{i}}$. Here, the subscripts correspond to the device contacts in Fig. 3.1c and d_{i} is the distance between consecutive skips along the edge of the i^{th} trajectory. For quantitative comparison with experiment where the y-axis is in terms of carrier density n, the Fermi energy ϵ_F for each Fermi surface extracted was converted to the corresponding carrier density by creating a dense mesh of $\boldsymbol{k}$-states in the mBZ and cumulatively counting the number of states below each Fermi energy, multiplying by 4 to account for the spin and valley degeneracy and dividing by the area of the moiré unit cell to obtain the correct units.

3.2 Device setup for TMF experiment

This work studies two high-quality dual gated TBG devices encapsulated with $\sim 30-50$ nm thick hBN crystals at two different twist angles: device D1 with a twist angle of $\theta = 1.87 \pm 0.01°$ (shown in Fig. 3.1c) and device D2, with $\theta = 2.60 \pm 0.01°$. Transport measurements showed that both devices exhibited similar behaviour, with low-temperature mobilities in excess of 400000 $\mathrm{cm^2V^{-1}s^{-1}}$ for carrier density $n \sim 10^{12}$ $\mathrm{cm^{-2}}$. The high mobility in both devices enabled the observation of TMF, which is a manifestation of the ballistic motion of electrons. Using theoretical methods to compare to the TMF maps obtained from the experiment, we show that the TMF technique can identify key features related to the shape of the Fermi surface in TBG.

Figure 3.1c shows the geometry of the device used to study the magnetic focusing effect in TBG. The narrow contacts 1 and 2 are used for injecting electrons into the device, i.e. driving current I_{12}, and contacts 3 and 4 are used to detect the voltage V_{34}. With a perpendicularly applied magnetic field, electrons injected at contact 1 propagate along the edge of the device in skipping orbits. The shape of the Fermi surface characterises the caustic pattern observed and this is illustrated in the insets of Fig. 3.1d. We can see that the caustics are focused onto equidistant focal points along the sample edge highlighted by the black arrows in the inset. In addition, the drift direction of the skipping orbits is determined by the sign of the magnetic field such that electrons and holes propagate in opposite directions for the same sign of the magnetic field. Varying the magnitude of the magnetic field varies the size of the skipping orbits and consequently the positions of the focal points. When the caustic focal points coincide with the position of the voltage probe, contact 3 in Fig 3.1c, a focusing peak is observed in the non-local resistance, which is given by $R_f = I_{12}/V_{34}$. Figure 3.1d shows the observed focusing peaks measured at different carrier densities, one TMF trace near the secondary Dirac points at the main neutrality point and one trace near the γ point in the mBZ.

3.3 Focusing maps with zero displacement

Figure 3.2a shows the dependence of R_f on the carrier density and magnetic field at zero displacement field, $D = 0$ Vnm^{-1}, for device D1. The presence of a R_f signal in a particular quadrant of the $B - n$ map reflects the sign of the cyclotron mass. Upon doping, the change of the quadrant of the TMF signal indicates an inversion of the electron dispersion, in other words, a change of sign of the mass from electrons to holes or vice versa. At zero carrier density, we see a fan-like pattern emerging from the centre of the TMF map in Fig. 3.2a. The pattern converges and changes direction at the main neutrality point. Similarly, at higher electron and hole densities, we observe qualitatively similar behaviour where a change in sign of the cyclotron mass is observed such that the TMF map resembles inverted fan-like patterns at higher energies. These indicate that the electronic dispersion converges towards a secondary neutrality point, which is shown in the calculated band structure in Fig. 3.1b at the γ point in the mBZ. The crossover carrier densities between these two regimes at $n \approx 3 \times 10^{12}$ cm^{-2} and -3×10^{12} cm^{-2} correspond to the presence of van Hove singularities (vHS) in the moiré miniband spectra. Figure 3.2b presents the theoretically calculated TMF map and we see good quantitative agreement between experiment and theory, which suggests that the band structure of TBG is well described by the calculated spectrum shown in Fig. 3.1b.

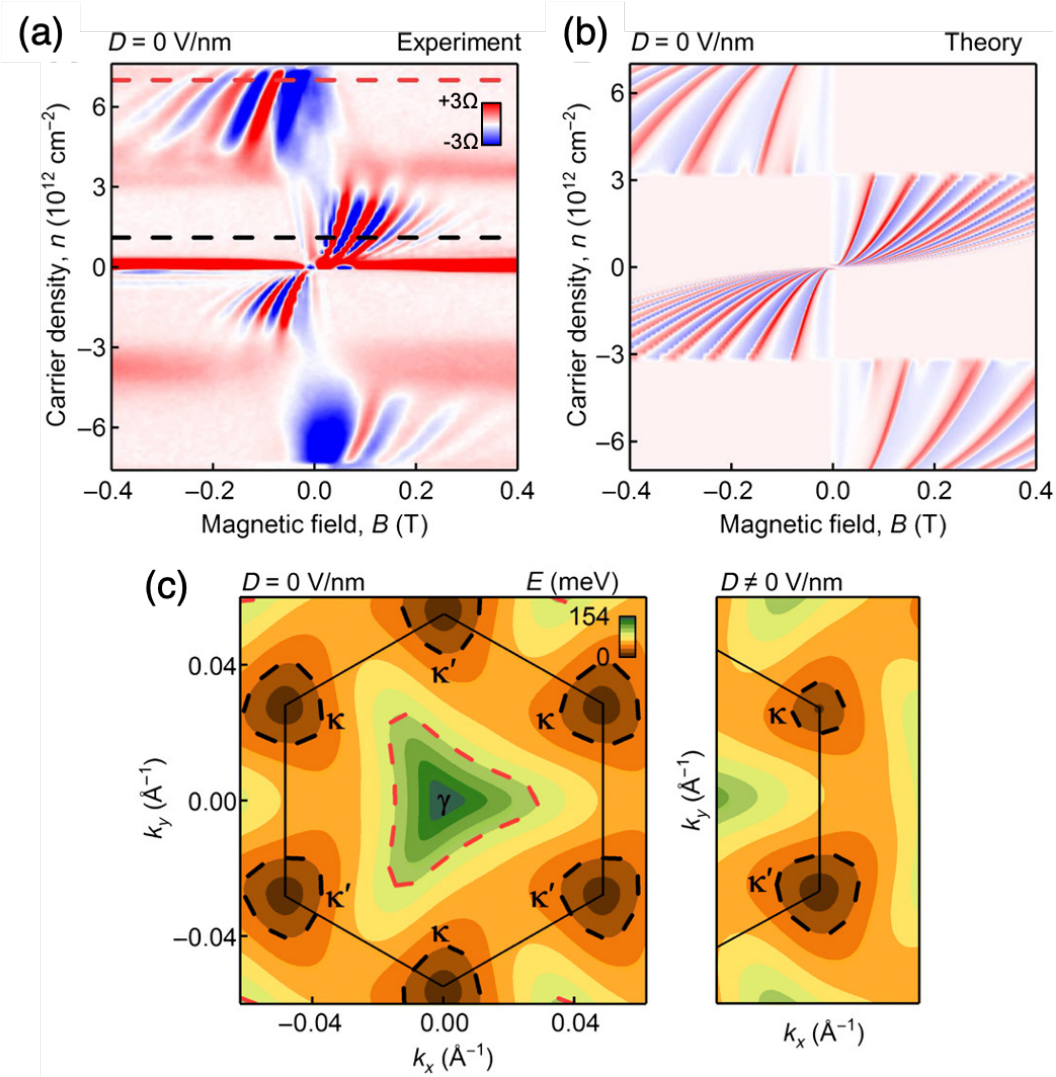

Figure 3.2: (a) Focusing signal R_f as a function of the magnetic field and carrier density measured at 2 K for device D1 in zero displacement field, $D = 0$ V nm^{-1}. Colour scale: blue to red, ± 3 Ω. (b) TMF map calculated from the energy spectrum shown in Fig. 3.1b. The angle between the zigzag edge of one of the monolayers and the sample boundary is taken as 45° to avoid any spurious effects of crystallographic alignment. The calculated TMF map is only very weakly sensitive to the mutual orientation between graphene and the sample edge, confirming the generality of our results. Note that the scale is the same as for panel (a). (c) Contour plot of the first conduction miniband shown for the K valley of the Brillouin zone for zero (left) and nonzero (right) displacement fields. Black and red dashed lines outline the shape of the Fermi surfaces for carrier densities marked by black and red dashed lines in (a); the latter corresponds to equivalent doping levels relative to the main (black) and secondary (red) neutrality points. The colour scale is from 0 to 154 meV.

In both the TMF map obtained from the measurement and the theoretically produced TMF map shown in Figs. 3.2a and 3.2b, the fan-like patterns emerging from the main and secondary neutrality points of the TBG superlattice - around zero carrier density and above the vHS, respectively - have different periodicities. This difference can be attributed to the different sizes of the Fermi surfaces at equivalent doping levels shown by the black and red dashed lines in Fig. 3.2a. Figure 3.2c shows a contour plot for the first conduction miniband shown for the K valley of the Brillouin zone for zero (left) and nonzero (right) displacement fields. The black and the red dashed lines correspond to the Fermi surface contours for the doping levels shown in Fig. 3.2a where the black dashed lines are around the κ and κ' points of the mBZ, i.e. the main neutrality point, and the red dashed line is around the γ point, i.e. the secondary neutrality point. Our theoretical analysis shows that the Fermi surfaces near the γ point are triangular in shape, which results from the strong interlayer hybridisation of the states originating from both graphene layers. In sharp contrast, the Fermi surfaces around κ and κ' points that coincide with the valley centres of the top and bottom graphene layers, are almost isotropic and similar to the Fermi surfaces found in monolayer graphene at the Dirac points. This suggests that there is weak interlayer hybridisation of these states at these points.

We calculate the density of states (DoS) of TBG using

$$\mathrm{DoS}(E) = 4 \int_{\mathrm{mBZ}} \frac{d^2k}{(2\pi)^2} \delta(E - \epsilon_{\mathrm{F}}), \tag{3.3.1}$$

where the factor of 4 encompasses spin and valley degeneracy and ϵ_{F} denotes the Fermi energy. Figure 3.3 shows the DoS plot for twist angle $\theta = 1.87°$. The minivalleys manifest itself as a zero DoS at charge neutrality, which is in agreement with the experimental TMF map in Fig. 3.2a that shows the fan-like pattern converging at the main neutrality point. In addition, the DoS shows minima at ± 4 carriers per moiré unit cell, which corresponds to the filling of one moiré miniband per spin and valley for a total degeneracy of 4. There is a sharp peak in the DoS on either side of charge neutrality, which indicates the presence of vHSs, which were observed in the TMF map in Fig. 3.2a where there is a change in sign of the cyclotron mass within the first conduction and valence bands.

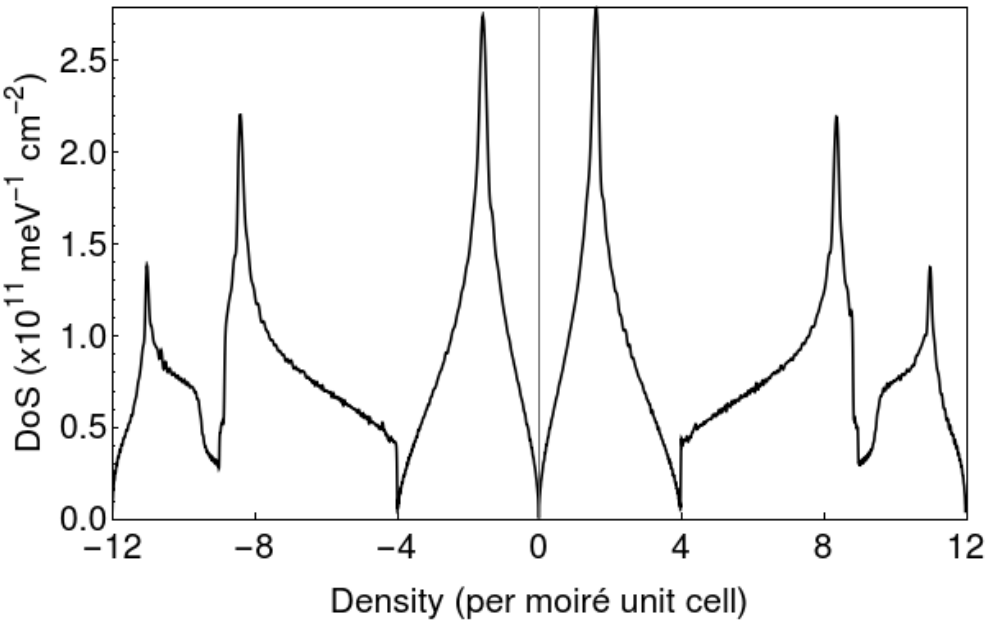

Figure 3.3: Calculated density of states for TBG with $\theta = 1.87°$

.

3.4 Focusing maps with a displacement field

As there is an absence of interlayer coupling between κ and κ' minivalleys, we can disentangle the TMF contributions from each by applying a finite displacement field. A field of up to $D = 0.75$ Vnm^{-1} without damaging the devices was applied and this shifted the onsite potential for the electrons. As a result, the layer symmetry is broken and the energies of the Dirac cones at κ and κ' shift upwards and downwards with respect to each other. This means that the size of the Fermi surfaces for equivalent doping levels about the Dirac points are now different as illustrated in Fig. 3.4c. The breaking of the layer-symmetry lifts the degeneracy between κ and κ' and the motion of the electrons from different valleys are separated in the presence of the magnetic field with different sizes of cyclotron orbits. This generates two magneto-oscillation frequencies of R_f at low carrier densities, $|n| < 10^{12}$ cm^{-2}. This is well seen in Fig. 3.4 where separate focusing peaks appear for the electrons from each valley and we see qualitatively that the theoretically produced TMF map shows minivalley splitting.

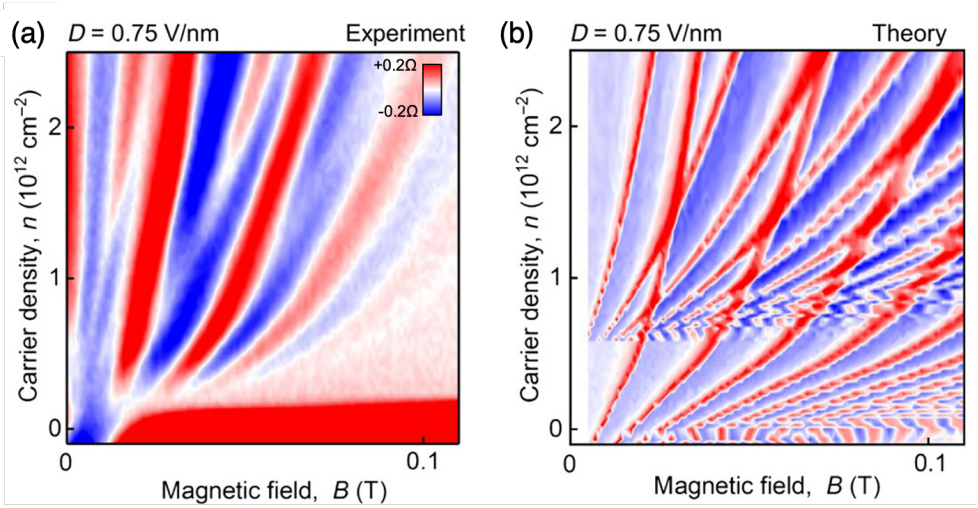

Figure 3.4: (a) R_f as a function of magnetic field and carrier density for device D2 measured at $T = 2$ K and $D = 0.75$ Vnm^{-1} at a distance of 8.5 μm from the injector. Color scale: blue to red, ± 0.2 Ω. (b) TMF map calculated numerically for device D2 in a displacement field, which shows the splitting of the focusing peaks originating from the different miniband dispersion at κ and κ'. Scale is the same as for panel (a).

3.5 TMF with different orientations

To investigate whether the TMF spectra are sensitive to the crystallographic orientation of graphene layers with respect to the skipping direction, i.e. the edge of the sample. Figure 3.5 compares TMF maps simulated for different edge orientations characterised by an angle ϕ. To this end, we fix the orientation of one of the monolayers so that $\phi = 0°$ corresponds to the zigzag edge and $\phi = 90°$ to the armchair edge. The results for parameters of device D1 at $|n| = 6.6 \times 10^{12}$ cm^{-2} give triangular skipping orbits with the distance between the focusing peaks along the sample boundary weakly dependent on ϕ. Similar results are obtained for all carrier densities where the Fermi surfaces are anisotropic, i.e., for $|n| > 3 \times 10^{12}$ cm^{-2} where the Fermi surface around the γ point has a pronounced triangular shape. Corresponding TMF maps show focusing peaks at slightly shifted positions relative to each other. The 3-fold symmetry of the triangular Fermi surface means that the TMF maps repeat every 60°. This can be seen when comparing the TMF maps for $\phi = 30°$ and $\phi = 90°$, which are identical. At low carrier densities, near the main neutrality point, the Fermi surfaces are almost isotropic and the TMF maps are independent of ϕ. In addition, the positions of van Hove singularities are also independent of ϕ, in agreement with Ref. [55].

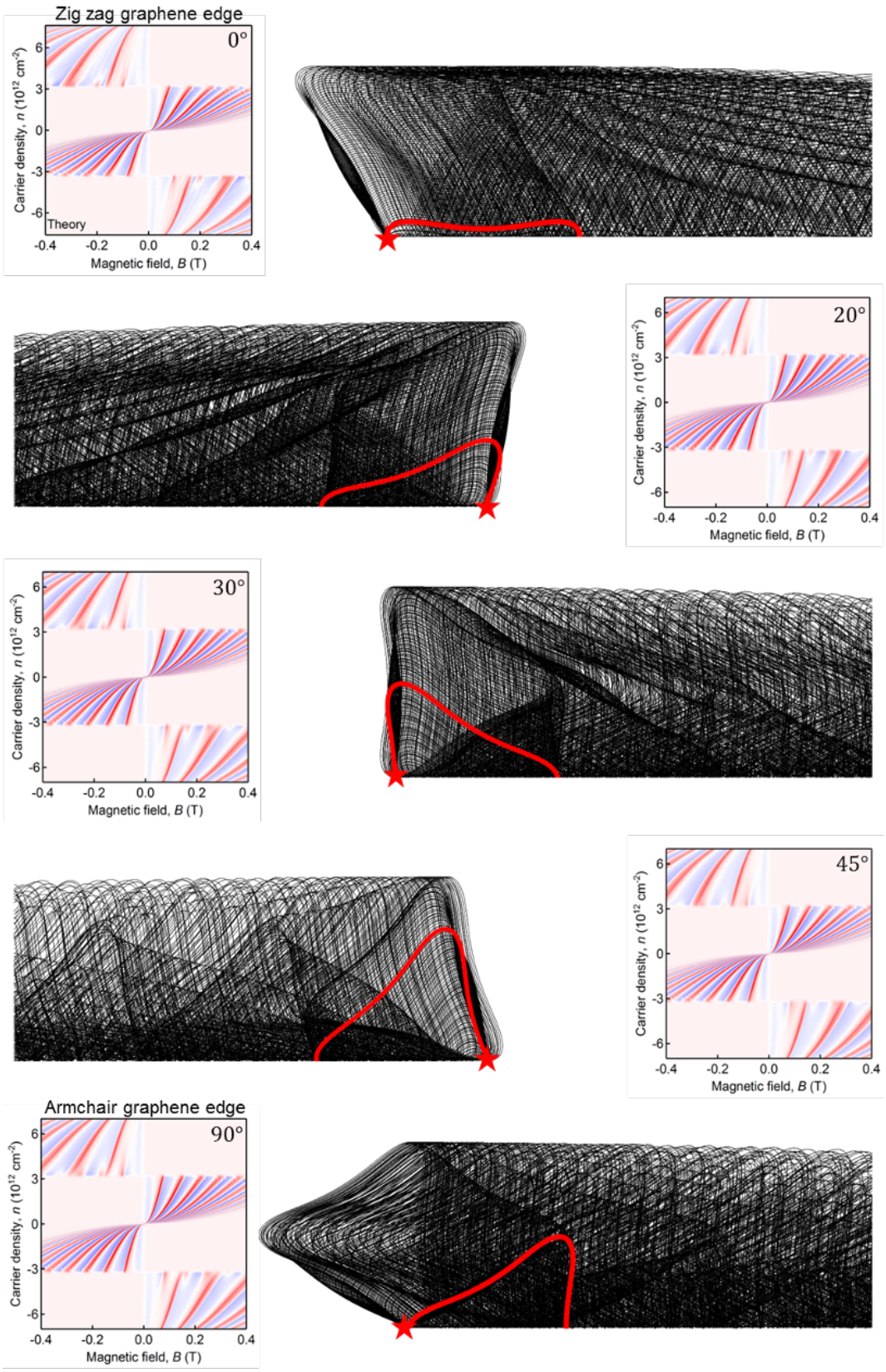

Figure 3.5: TMF maps simulated skipping orbits for different edge alignment. The units are arbitrary with the red and blue representing positive and negative resistance, respectively. The TMF maps are simulated for $\phi = 0°, 20°, 30°, 45°$ and $90°$ for device D1. The orientation of one of the monolayers is fixed such that $0°$ corresponds to the zigzag edge and $90°$ to the armchair edge. The skipping orbits are shown at $|n| = 6.6 \times 10^{12}$ cm^{-2}.

3.6 TMF with a displacement field

The transverse magnetic focusing (TMF) map in Fig. 3.4 shows the effect of a finite displacement field between the two graphene monolayers. To find the effective electric field for each carrier density n, we take into account electrostatic screening. At twist angles $\sim 2^\circ$ and at low carrier densities, the two monolayers are almost decoupled. To take into account electrostatic screening in this case, we include a screening term as proposed in Refs. [64, 65] given by the equations

$$\frac{ec_0}{\epsilon_0\epsilon}\left(\epsilon_0 D - \left(\frac{1+\epsilon}{4}\right)(n_1 - n_2)\, e\right) = \frac{h\upsilon}{2\sqrt{\pi}}\left(s_1\sqrt{|n_1|} - s_2\sqrt{|n_2|}\right), \tag{3.6.1}$$

$$n = n_1 + n_2. \tag{3.6.2}$$

The carrier densities in the two parallel graphene layers are given by n_1 and n_2 and they are separated by a distance c_0. The applied displacement field is denoted D, Dirac velocity is υ and the band indices s_1 and s_2 are given by $s_i = n_i/|n_i|$. Here, we take the electron charge as $e < 0$. In the case of TBG, we use $d \approx 0.34$ nm and following Refs. [65, 66, 67], the dielectric constant for twisted bilayer graphene is $\epsilon = 2.7$ as the field D is screened by both the free charges and also the dielectric environment between the layers. The total carrier density n is given by Eq. (3.6.2). To find the effective electric field for each value of n and D used in the experiment, the two equations are solved simultaneously using the Dirac velocity for monolayer graphene, $\upsilon = 10^6$ ms^{-1}. In the calculation, we take n_1 to be the bottom layer and n_2 to be the top layer. The positive direction of the applied field D is from the top to the bottom (i.e. pointing downwards). After the corresponding onsite potential difference was calculated for each carrier density, the Fermi surfaces were extracted for each doping to apply the TMF method described in section 3.5. Figure 3.6 shows additional TMF maps obtained from experiment and compared to the theoretically calculated maps for device D2 with $D = 0.5$ Vnm^{-1} and $D = 0.75$ Vnm^{-1}. The experiment shows good agreement with the theoretical calculations where the higher applied displacement field causes more

pronounced splitting between the minivalleys at low carrier densities. This can be seen by tracing the eye of the two split peaks in the TMF map in Figs. 3.6a and 3.6b close to $B = 0$ T.

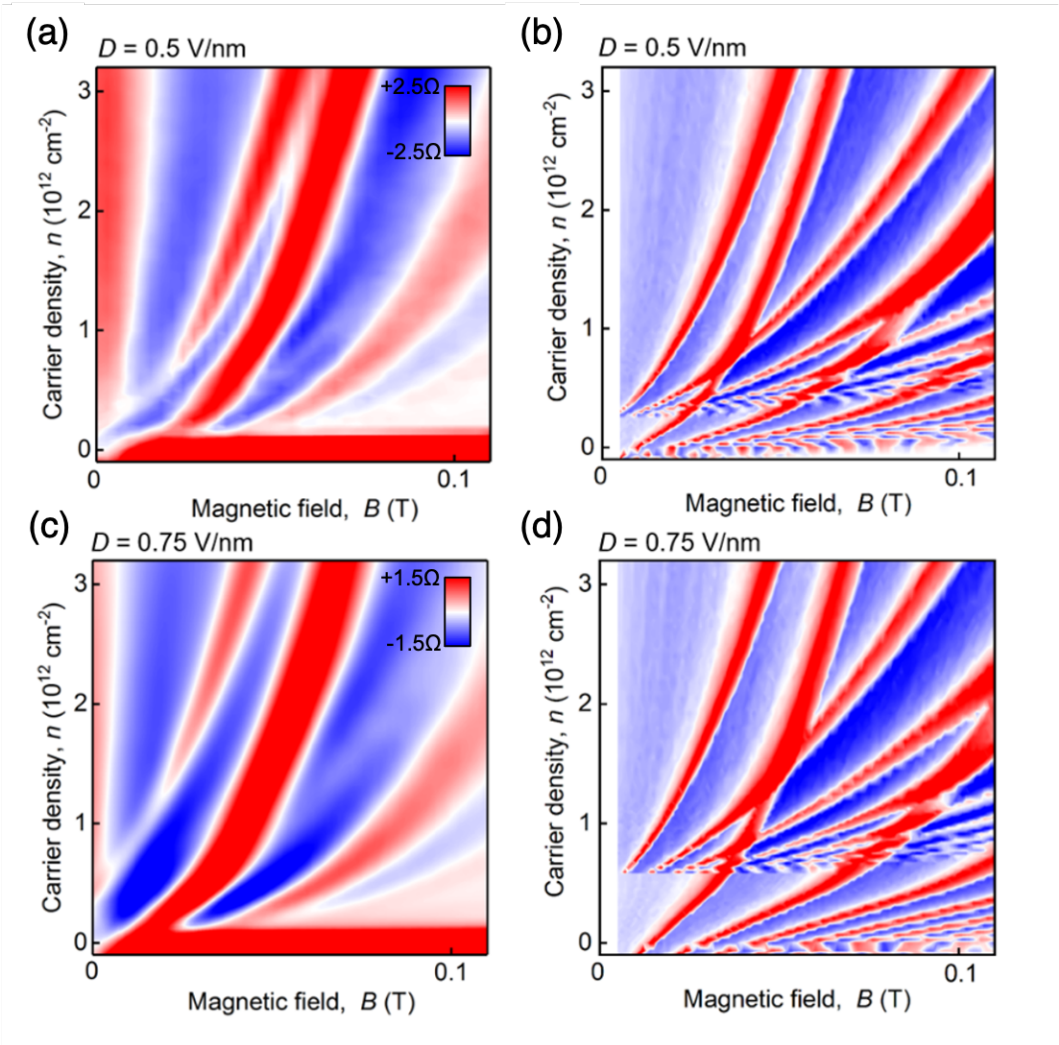

Figure 3.6: (a) R_f as a function of magnetic field and carrier density measured for device D2 at $T = 2$ K and $D = 0.5$ Vnm^{-1} at a distance of 4.9 μm from the injector. Color scale: blue to red, ± 2.5 Ω. (b) TMF map calculated numerically for panel (a). (c) R_f as a function of magnetic field and carrier density measured for device D2 at $T = 5$ K at a distance 4.9 μm from the injector in a displacement field 0.75 Vnm^{-1}. Color scale: blue to red, ± 1.5 Ω. (d) TMF map calculated numerically for panel (c).

3.7 Self-consistent screening

In section 3.6, modelling TMF with a displacement took into account electrostatic screening by solving Eqs. (3.6.1) and (3.6.2) simultaneously. This section will show the stand-alone iterative self-consistent calculation that was completed for TBG with twist angle $\theta = 3^\circ$ to show that an applied interlayer potential and the resulting charge density redistribution strongly screens an external electric field. The goal of the self-consistent calculation is to find the corresponding onsite potential energy difference Δ, given by the left-hand side of Eq. (3.6.1), between the two graphene layers for a fixed applied displacement field D and a fixed doping n. Figure 3.7 shows a diagram illustrating the directions of the applied and screening field. The applied displacement field D points downwards and causes electrons to accumulate on graphene layer 1. This charge instability in the system causes electrons to redistribute so that a screening field E_s is generated in the opposite direction to counteract the direction of the applied field. The self-consistent calculation reflects the screening effect in the physical system as charges redistribute between the two layers until the system is stable.

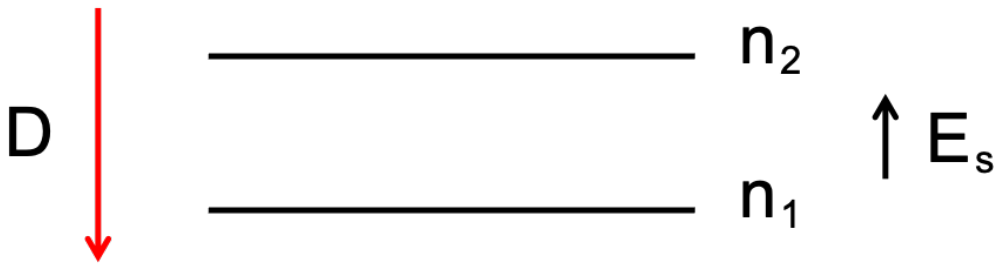

Figure 3.7: Schematic of TBG with applied displacement field D and the resulting electrostatic screening field E_s.

For the first iteration, we take the interlayer potential difference from the unscreened equation, which is the first term of Eq. (3.6.1). A fine mesh is created in $\boldsymbol{k}$-space and using the Hamiltonian in Eq. (2.1.1), the matrix is diagonalised to find the corresponding eigenvalues and eigenvectors for every $\boldsymbol{k}$-state. For each iteration of the self-consistent calculation, the charge neutrality point is found by finding the energy where the electron count and the hole count is the same. With this information, the Fermi energy at the fixed doping is found. Following this, the occupied wave functions

at energies below the Fermi energy are identified. The screening electron density accumulated on each layer n_i for $i = 1, 2$ is then found by calculating

$$n_i = 4 \int_{\text{mBZ}} \frac{d^2k}{(2\pi)^2} \sum_{l=1}^{4} \left[\left(\left| \Psi^l_{A_i}(k) \right|^2 + \left| \Psi^l_{B_i}(k) \right|^2 \right) f(\epsilon_l - \epsilon_f) - 1 \right], \tag{3.7.1}$$

where i is either layer 1 or layer 2, l is the band index for which there is four in TBG, $\Psi^l_{A_i}(k)$ and $\Psi^l_{B_i}(k)$ are the normalised wave functions of sublattices A and B in a particular layer, f is the Fermi function, ϵ_f is the Fermi level and the -1 ensures electrical neutrality when there is the interlayer potential [68]. The -1 originates from the fact that carbon has four valence electrons, and when only the valence band is filled at charge neutrality with zero doping, the Fermi-Dirac distribution has a contribution of $1/2$ for each electron. The excess carrier densities n_1 and n_2 are substituted back into the equation to produce a new Δ to give the screened field. Numerically stable self-consistent solutions are obtained for a range of fixed D and doping n.

Figure 3.8 plots the interlayer energy difference Δ against the carrier density n for a range of displacement fields D. As carrier density increases, the displacement field is more screened. This can be intuitively understood by considering the band structure for TBG with a perpendicular electric field in section 2.1.4, at higher Fermi energies, the difference in excess carrier densities accumulated on each layer increases. In comparison to the electrostatic screening present in bilayer graphene in Ref. [51], the effect of screening is greater in TBG as a result of stronger coupling between the graphene layers. For a displacement field $D = 2$ Vnm^{-1} in bilayer graphene, $\Delta \sim 200$ meV [51], while in TBG $\Delta \sim 150$ meV as shown in Fig. 3.8.

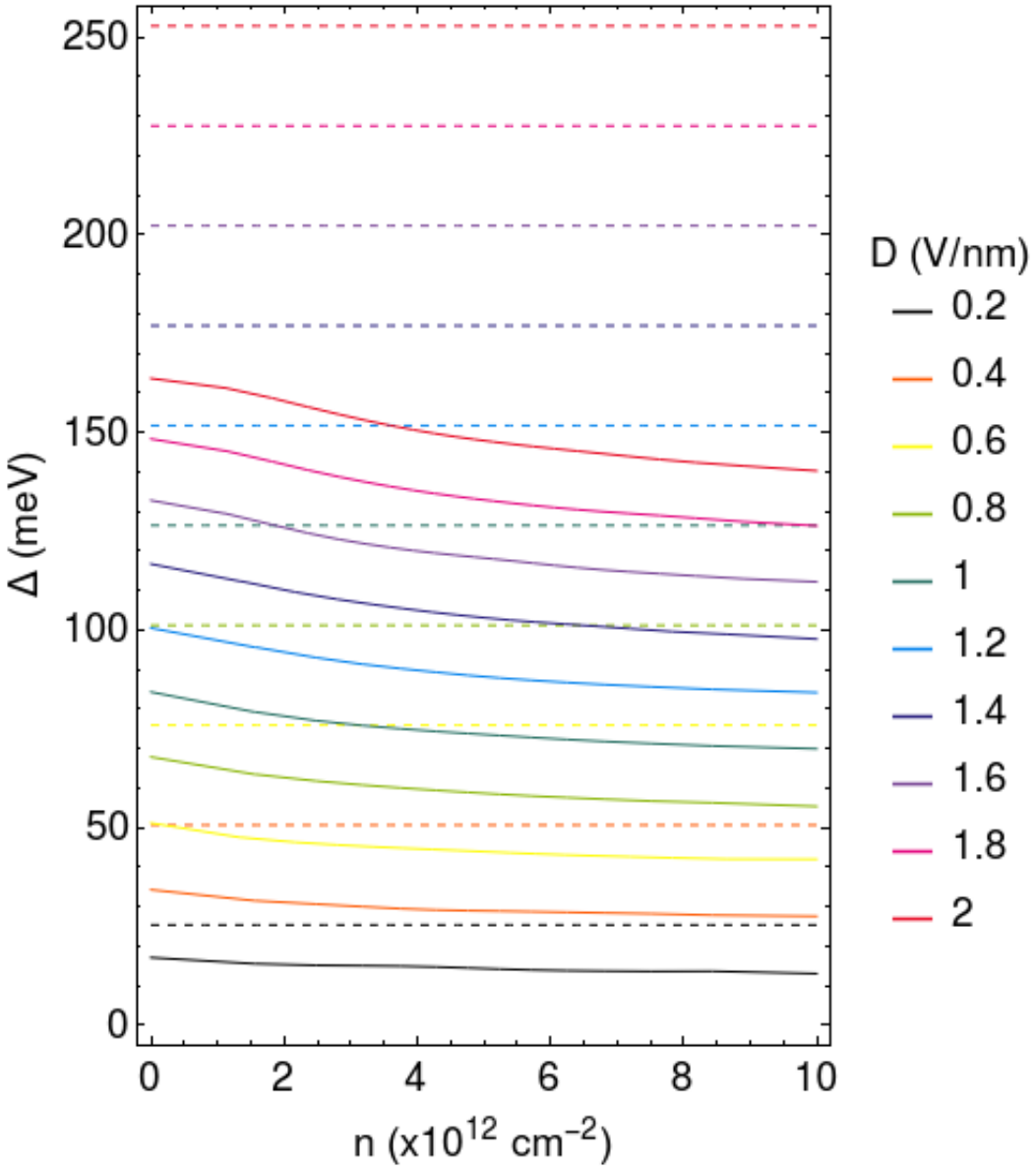

Figure 3.8: Interlayer potential difference Δ as a function of carrier density n for various applied displacement fields for twisted bilayer graphene with a twist angle of $\theta = 3°$. The dashed lines are the corresponding unscreened calculations.

3.8 Temperature dependence of TMF

By considering the temperature dependence of TMF and the evolution of consecutive focusing peaks, we can gain a deeper understanding of the carrier dynamics in TBG. Figure 3.9a shows how the amplitude of the TMF oscillations are affected by temperature T in the range $2\text{K} < T < 30\text{K}$ close to the main neutrality point at κ and κ', and the secondary neutrality point at γ. As temperature increases, the TMF amplitude becomes suppressed. We extract the relative scattering length for quantitative analysis using the same equation as in Ref. [55]

$$\frac{L_\text{s}}{L_\text{path}} = \left(\ln\left[\frac{A(T_\text{base})}{A(T)}\right]\right)^{-1}, \tag{3.8.1}$$

where L_path is the length of the trajectories traversing from the injection point to the first focal point as shown in the insets in Fig. 3.1, $A(T)$ and $A(T_\text{base})$ are the areas under the first or second focusing peak in Fig. 3.9a at temperature T and $T_\text{base} = 2$ K, respectively. Figure 3.9b is a plot of the temperature dependence of the relative scattering length, which show that all focusing peaks follow a T^{-2} scaling. This dependence suggests that low-angle electron-electron scattering dominates at low temperatures rather than phonon-dominated scattering, which would be characteristic of a T^{-1} dependence [60, 69]. Such temperature dependence was also found to be the reason for TMF suppression in graphene/hBN superlattices [55].

We can further analyse the differences between the TMF focusing of electrons near the main neutrality points and secondary neutrality points by calculating the ratio between the areas under the 2nd and 1st focusing peaks in Fig. 3.9a, A_2/A_1. This ratio characterises the proportion of electrons that undergo specular reflection at the sample boundary. The closer the ratio is to one, the higher the probability for injected electrons to reflect specularly. The inset in Fig. 3.9b shows the ratio of the amplitudes of the second and first focusing peak as a function of temperature for carrier densities $n = 1.8 \times 10^{12}$ cm^{-2} (right panel of Fig. 3.9a) and $n = 6.6 \times 10^{12}$ cm^{-2} (left panel of Fig. 3.9a). At low carrier densities where the Fermi surfaces are almost isotropic, $A_2/A_1 \approx 0.8$, which points towards almost specular reflection whereas for

higher carrier densities where the Fermi surfaces are triangular, $A_2/A_1 \approx 0.65$, which is less specular in comparison. For the latter case, it indicates a higher probability of diffusive scattering, which is consistent with the greater sensitivity of triangular Fermi surfaces in the miniband spectrum to perturbations of the moiré pattern near the sample edge. On the other hand, there is little hybridisation between the layers in the vicinity of κ and κ' and thus, it is expected that the scattering of Dirac electrons are less affected by the termination of the superlattice periodicity near the edge, while the spectrum near the γ point is affected more, which promotes diffusive scattering.

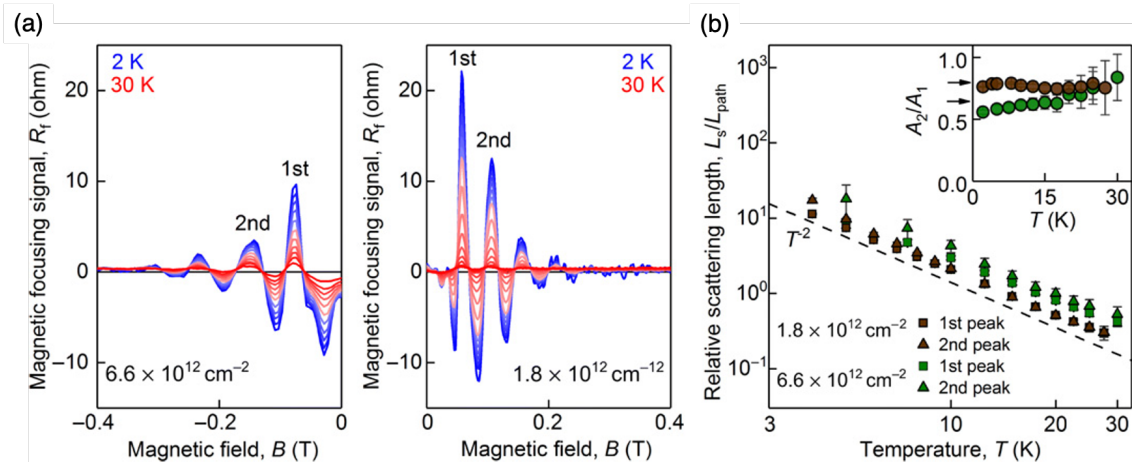

Figure 3.9: (a) Temperature dependence of the TMF signal measured at two characteristic carrier densities for device D1 (see legends). T was varied from 2 to 30 K (blue to red). (b) T dependence of the relative scattering length (see text) extracted from experimental data for consecutive focusing peaks. Absolute scattering lengths for several relative orientations of the crystallographic axes and the sample edge are shown in Fig. 3.5. The dashed line shows T^{-2} dependence. The inset shows the ratio of the areas under the first and second focusing peaks in (a) as a function of T. Arrows correspond to $A_2/A_1 = 0.8$ and 0.65. Error bars indicate the accuracy of determining A_2/A_1; large errors at $T > 20$ K are due to the relatively large background signal as the focusing peaks become strongly suppressed. [Figure provided by Alexey Berdyugin.]

Near the main neutrality point, there is little hybridisation between the two layers and the Fermi surfaces are isotropic and almost circular. This means L_{path} of electrons for low carrier densities can be approximated by $L_{\text{path}} \approx \pi L/2$ where L is the distance from the current injector to the voltage probe. The length of this trajectory is independent of the angle between the crystallographic axes orientation of the graphene layers and the sample edge. However, Fig. 3.5 shows that near the secondary neutrality point, L_{path} is sensitive to the relative orientation of the graphene layers and the sample

edge. For different orientations of TBG with the sample edge, L_{path} was calculated for several characteristic angles between the device edge and zigzag axis of the top graphene layer: $L_{\text{path}-0^\circ} = 1.11\ L$; $L_{\text{path}-10^\circ} = 1.25\ L$; $L_{\text{path}-20^\circ} = 1.58\ L$; $L_{\text{path}-30^\circ} = 1.77\ L$; $L_{\text{path}-45^\circ} = 1.93\ L$. Using these values, the absolute scattering length L_s was extracted as shown in Fig. 3.10. For all cases, scattering lengths vary between $\sim 100\ \mu$m and a few μm at low temperatures, indicating that at elevated temperatures, electron-electron scattering plays an important role in TMF suppression.

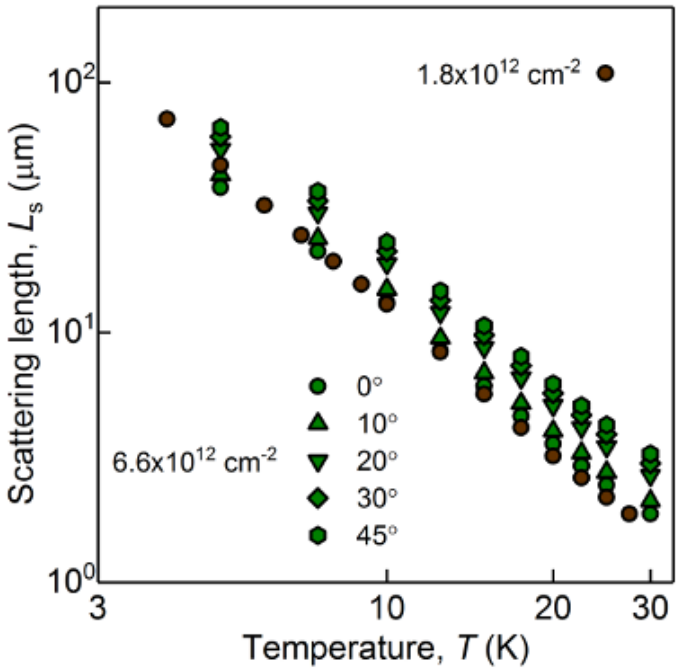

Figure 3.10: Electron scattering lengths corresponding to different relative orientations of the graphene's crystallographic axes and the sample edge were extracted from the temperature dependence of the first focusing peak in Fig. 3.9b using the calculated L_{path}. [Figure provided by Alexey Berdyugin.]

To conclude, this work uses TMF as a tool to probe the band structure of TBG. We have demonstrated the ballistic propagation of electrons in TBG and electron transport properties have been determined by the reconstruction of the energy spectrum in the presence of the long-range moiré potential. Furthermore, theoretical calculations are in agreement with the experiment where it is shown that a displacement field can be used to selectively manipulate electrons originating from different valleys. This could open up an avenue of implementing and exploiting the valley degree of freedom in electronic devices.

Chapter 4

Network of topological channels in twisted bilayer graphene

The ability to vary the electronic properties of twisted bilayer graphene by simply altering the twist angle between the layers has provided a versatile platform for researchers to explore rich physical phenomena at different twist angles. Previous theoretical works have investigated the effect of a perpendicular electric field on TBG [70, 71, 72, 73, 74, 75, 76, 77], and it was found that a large enough bias gives rise to a network of topological channels on the domain boundaries between AB and BA stacking regions [71, 73, 74, 75, 76, 77]. At these stacking regions, the electronic states are locally gapped out by the interlayer bias [78]. Previous works have shown the presence of two topological modes per spin and per valley along each AB-BA boundary [79, 80, 81, 82, 83, 84, 85]. The AB and BA regions have opposite signs of single-valley Hall conductivities, $+e^2/h$ and $-e^2/h$, respectively [86]. The difference of $2e^2/h$ results in two boundary modes per spin and per valley. The band structures obtained from the K and K' valley are π rotations of each other, which means the two modes propagate in opposite directions between the two valleys. We showed that the overlap of two graphene layers with a relative twist between the directions of their crystallographic axes forms a moiré pattern where the AB and BA regions appear periodically in a hexagonal pattern [87, 88, 89]. The boundary channels form a triangular grid with two modes travelling between adjacent AA stacking regions, as illustrated in Fig. 4.1a.

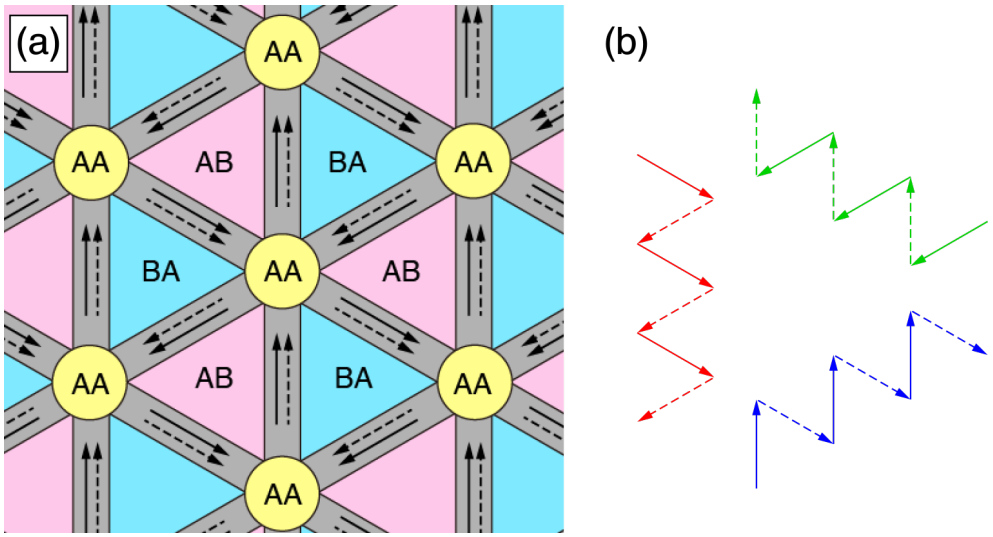

Figure 4.1: (a) Domain structure showing AB and BA regions and topological boundary channels that connect AA regions in biased TBG. The solid and dashed arrows represent independent propagating modes, modes 1 and modes 2, for the K valley. (b) Independent 1D eigenmodes in three directions. [Figure provided by Mikito Koshino.]

There are experimental studies that probe the network of topological channels present in TBG using transport measurements [90, 91, 92] and scanning tunnelling spectroscopy [20]. Given the structure of the moiré pattern, it may be expected that the electronic transport in the emergent topological channels of TBG could be described using a percolation network on a triangular lattice [93]. In general, such a percolation network model would split incoming modes into two or more outgoing modes in different directions. However, we show that for small-angle TBG with a large bias, instead of the expected two-dimensional network of topological modes, perfect 1D eigenmodes appear on the triangular AB-BA domain boundary and they propagate independently in three different directions. A schematic of these modes is shown in Fig. 4.1b where specific incoming and outgoing modes are connected at each vertex, i.e. at the AA stacking region nodes. The modes along different directions are never hybridised, and therefore all these states serve as independent perfect 1D channels over the entire TBG lattice. The results in this chapter have been published in [94] and our findings are consistent with Ref. [75] that discusses the perfect nesting of the Fermi surface in biased TBG. The versatility of tuning the TBG energy dispersion by applying a perpendicular electric field means there are opportunities to explore the parameter space to experimentally realise these 1D eigenmodes.

In this chapter, we study TBG for angles below the magic angle with an applied bias using the continuum-model Hamiltonian described in section 2.1. We demonstrate the emergence of two well-defined energy windows that contain sparsely distributed 1D eigenmodes on either side of zero energy. At zero energy, the band structures exhibit a cluster of nearly flat bands around the charge neutrality point. The origin of these energy windows are explained using a perturbational approach from the small interlayer coupling limit, and also by considering the two-band model consisting of the intersecting electron and hole bands of single-layer graphene in the presence of an interlayer bias.

4.1 Band structures and wave functions

Figure 4.2a presents the electric field dependence of the TBG band structure for various twist angles below the magic angle, $\theta = 1°, 0.5°, 0.3°$ and $0.2°$. The band structures include energy bands from both the K (black) and K' (red) valleys and is shown for the path $\kappa \to \gamma \to \mu \to \kappa'$ in the mBZ illustrated in Fig. 4.2b. In this work, we do not account for corrugation between the two graphene layers such that the interlayer coupling used in the tunnelling block of the Hamiltonian in Eq. (2.1.3) is $u = w_{\mathrm{AA}} = w_{\mathrm{AB}} = 0.103$ eV in this chapter. In addition, the convention used in this chapter is that the original Dirac point of layer 1 is placed at κ' while the original Dirac point of layer 2 is placed at κ. For small-angle TBG, we see that as the perpendicular electric field Δ increases, bands gradually shift towards zero energy both on the conduction and valence sides of the spectrum. This results in the formation of a cluster of very narrow bands around the charge neutrality point. Simultaneously, two well-defined energy windows are formed above and below the zero-energy band cluster where the energy bands within are sparsely distributed in comparison. In addition, we see that the size of the energy windows have a weak dependence on the size of Δ, which can be seen for $\theta = 0.2°$ where the energy window stays a similar size in increasing Δ.

The formation of 1D propagating modes inside the energy windows is of particular interest. These modes connect the cluster of bands at zero energy to the bulk bands outside of the energy windows. Figure 4.2c shows a three-dimensional band structure

of TBG calculated for $\theta = 0.5^\circ$ and $\Delta = 400$ meV in the K valley. On either side of charge neutrality, we see intersecting planes in the energy windows. Figure 4.2d shows the Fermi surface of the same system at a Fermi energy $E_F = 50$ meV with both the K and K' valleys plotted in black and red, respectively. For each valley, the electronic dispersion is composed of three intersecting planes within the energy windows. For the K valley, the planes have band velocities that are parallel to $(0, -1)$, $(\sqrt{3}/2, 1/2)$ and $(-\sqrt{3}/2, 1/2)$ directions. The different planes are independent of each other and there is no hybridisation between them, which results in nearly straight Fermi lines at a given Fermi energy. These findings were also reported in Ref. [75]. Moreover, we notice the presence of some flat bands near the upper limits of the energy windows close to the bulk bands that are independent of the 1D states. For example, in Fig. 4.2a, $\theta = 0.3^\circ$ in the largest bias $\Delta = 400$ meV, there are three horizontal lines between 50 meV $< |E|$ 100 meV, which can be interpreted as pseudo-Landau levels of the fictitious gauge field [73]. The qualitative features shown in the band structures obtained from the continuum-model Hamiltonian in Fig. 4.2, including the presence of the energy windows and the perfect 1D eigenmodes, agree with the band structures obtained from the tight-binding model shown in our paper [94].

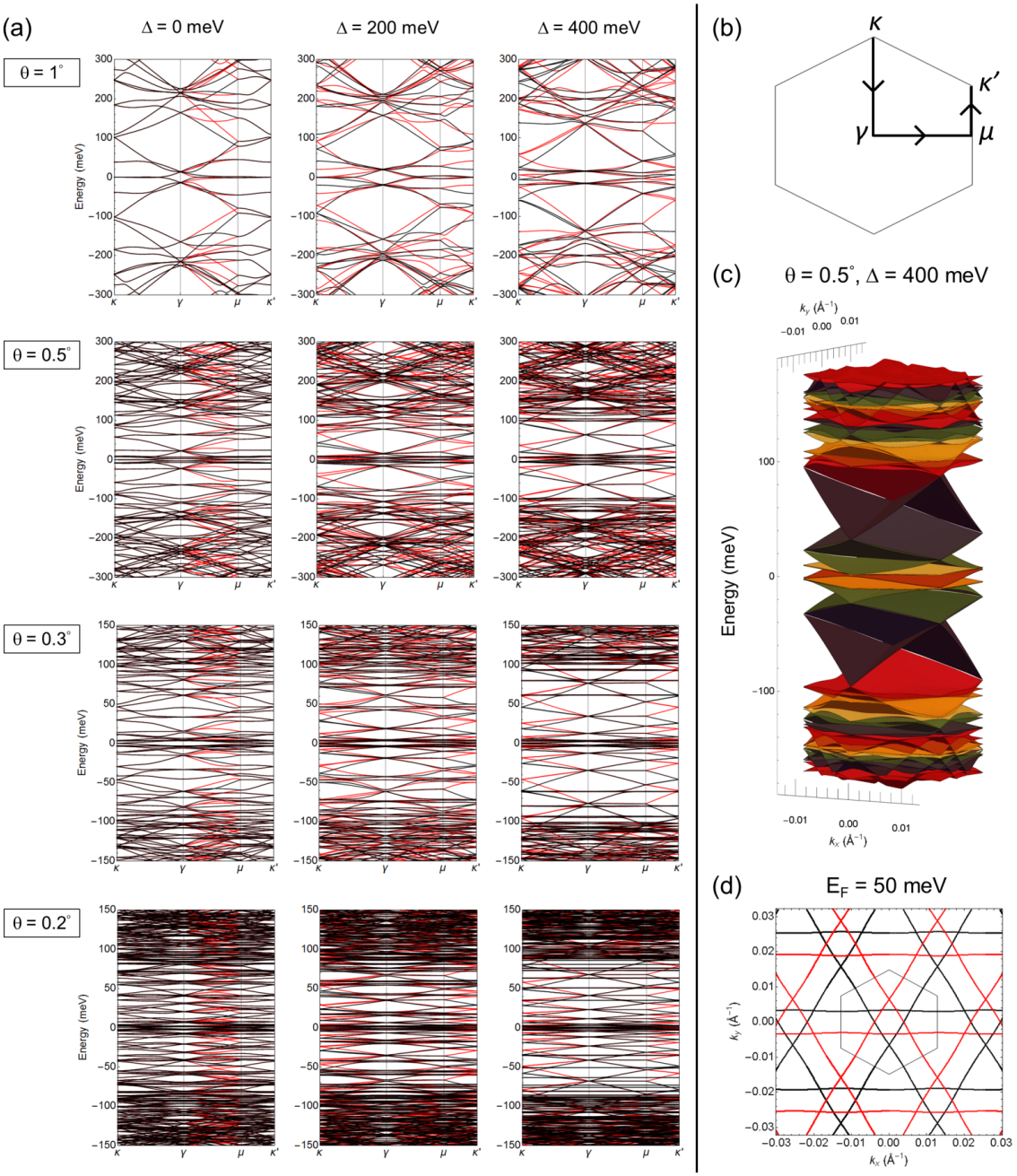

Figure 4.2: (a) Band structure of the twisted bilayer at various twist angles and varying Δ, calculated using the continuum model. (b) The moiré Brillouin zone showing the high symmetry points. (c) A three-dimensional plot of K-valley bands, and (d) the contour plot at $E_F = 50$ meV, calculated for $\theta = 0.5°$ and $\Delta = 400$ meV. The black and red lines represent K and K' valleys, respectively.

Figure 4.3 shows the wave functions for states in the energy window of TBG with $\theta = 0.5^\circ$ and $\Delta = 600$ meV in the K valley. The states are chosen from the same Fermi energy on the conduction side of the spectrum. The figure shows the squared amplitude on sublattices A_1, B_1, A_2 and B_2 and we see that the wave amplitude is mainly concentrated on layer 1, while it is concentrated on layer 2 in the valence band states. For the state marked by the red circle along the $\kappa - \gamma$ direction in Fig. 4.3 where the velocity is along the k_y direction, the wave function takes a 1D form and extends along the y-direction with no contribution in the x-direction. The wave functions for the states marked by the yellow and green circle in Fig. 4.3 are obtained by a $\pm 120^\circ$ rotation. These zigzag-shaped wave functions are localised on the AB-BA boundary separating the AB and BA regions where the energy band is gapped out. This work is in agreement with wave functions obtained from the tight-binding model in our paper [94] and were also reported in Ref. [75].

For the sake of completeness, we note that in the presence of lattice relaxation in TBG, described in our paper [94], the AB and BA significantly expand and the wave functions become more confined to the AB-BA boundary [75, 76]. In addition, the wave functions in the y-direction for relaxed TBG show that the amplitude is only on the boundaries of the other two directions along $(\sqrt{3}/2, -1/2)$ and $(-\sqrt{3}/2, -1/2)$ rather than the y-direction. Furthermore, the structure of the wave function along $(\sqrt{3}/2, -1/2)$ and $(-\sqrt{3}/2, -1/2)$ boundaries differ. Given that there are two topological modes per spin and per valley along each AB-BA boundary as illustrated in Fig. 4.1, this suggests that mode 1 is always scattered to mode 2 in the -120° direction and mode 2 is always scattered to mode 1 in the $+120^\circ$ direction. This results in three independent 1D propagating modes that are related by a 120° rotation as illustrated in Fig. 4.3.

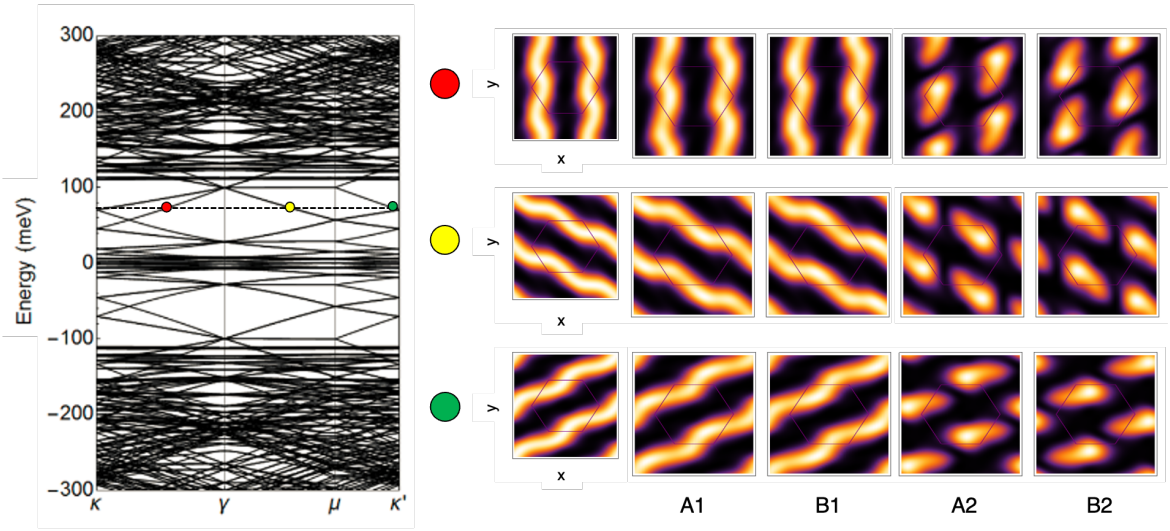

Figure 4.3: Energy spectrum and the wave functions of typical states at K valley in the energy window (indicated in the spectrum) calculated for $\theta = 0.5°$ and $\Delta = 600$ meV. The plots of the wave functions represent squared amplitude on sublattice A_1, B_1, A_2 and B_2 separately, where the hexagonal outline indicates a single moiré unit cell.

4.2 Origin of the perfect 1D eigenmodes

The origin of the energy window and the 1D eigenmodes can be intuitively understood by a perturbational approach from the small interlayer coupling limit. Figure 4.4 shows the continuum-model band structure of TBG with $\theta = 0.3°$ and $\Delta = 400$ meV, and with increasing interlayer coupling u from zero to the actual value in TBG. With small u, we see that two gaps open on the electron side and the hole side, and they eventually become the window regions in the full u parameter. We see that the 1D eigenmodes always remain inside the gap, preventing the spectrum from becoming fully gapped. The width of the energy window is on the order of u. As u increases, the energy bands between the two energy windows become squashed to form the zero-energy band cluster.

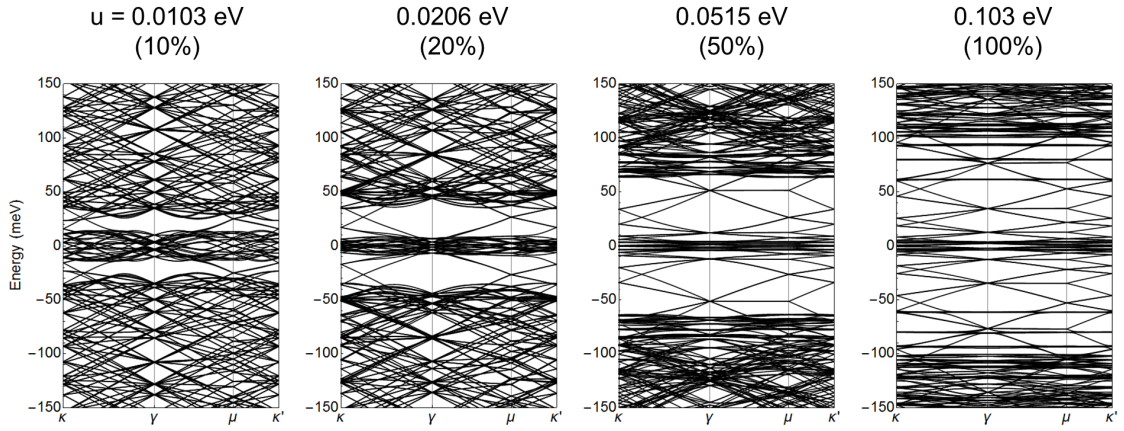

Figure 4.4: Band structure of the continuum model for twisted bilayer graphene with $\theta = 0.3°$ and $\Delta = 400$ meV, and the interlayer coupling u from zero to the actual value in TBG.

We can explain the opening of the two energy gaps for small u by considering what happens between the conduction band of one graphene layer and the hole band of the other graphene layer in the presence of an interlayer bias in the two-band model. For large Δ, the low-energy band structure is dominated by the hole band of graphene layer 1 and the electron band of layer 2 such that the two conical bands cross each other with a relative momentum shift of $\Delta \boldsymbol{K}_j (j = 0, 1, 2)$ via the interlayer tunnelling Hamiltonian T in Eq. (2.1.7), and the band anticrossing occurs at the cross-section. Figure 4.5a shows the crossing lines between the hole band of graphene layer 1 and the electron bands of graphene layer 2 with the three relative momentum shifts for $\theta = 0.3°$ and $\Delta = 200$ meV. The red, blue and green circles correspond to the crossing points with the hole band for $j = 0, 1, 2$. In Fig. 4.4, the size of the energy gap is approximately the value of the interlayer coupling u. By calculating the matrix element between the eigenstates of the hole band and the electron band, we do indeed find that the matrix element is approximately proportional to u, i.e. the size of the gap. Graphene's eigenstates in the (A,B) spinor representation are written as

$$|\boldsymbol{k}, s\,|=\rangle \frac{1}{\sqrt{2}} \begin{pmatrix} 1 \\ -se^{i\theta(\boldsymbol{k})} \end{pmatrix}, \tag{4.2.1}$$

where $s = \pm$ denotes either the conduction or valence band, respectively and the polar

angle is given by $\theta(\boldsymbol{k}) = \arctan(k_y/k_x)$. The matrix element of T from the hole band of graphene layer 1 to the conduction band of graphene layer 2 is calculated as

$$\langle \boldsymbol{k} + \Delta \boldsymbol{K}_j, +|T|\boldsymbol{k}, -\rangle \approx iu \sin\left[\theta(\boldsymbol{k}) - \frac{2\pi j}{3}\right], \tag{4.2.2}$$

where we assume $|\Delta \boldsymbol{K}_j| \ll |\boldsymbol{k}|$. Figure 4.5b shows the amplitude of the interlayer matrix element on the crossing lines on the Dirac cones of the two graphene layers. The thicker the line, the higher the amplitude. The matrix element vanishes near zero energy, which is marked by the black ring in Fig. 4.5b. This is the reason why two energy windows form on either side of charge neutrality. For a small-u limit, the number of states per unit area sandwiched by the two gaps is given by $2n_W$,

$$n_W = g_v g_s \frac{\Delta}{4\pi\hbar\upsilon} |\Delta \boldsymbol{K}_j|, \tag{4.2.3}$$

where $g_s = g_v = 2$ are the spin and valley degeneracies and $|\Delta \boldsymbol{K}_j| = 4\pi\theta/(3a)$. The parameter n_W characterises the carrier density needed to reach the energy window of the 1D eigenmodes, for example, for $\theta = 0.3^\circ$ and $\Delta = 200$ meV the carrier density is $n_w = 1.08 \times 10^{12}$ cm^{-2}. To obtain Eq. (4.2.3), the density of states for $|E| < \Delta/2$ is found to be $D(E) = g_s g_v \Delta/(2\pi\hbar^2\upsilon^2)$ and this is multiplied by the maximum energy of the crossing lines between the Dirac cones in Fig. 4.5a, which is given by $\hbar\upsilon|\Delta \boldsymbol{K}_j|/2$. The perfect 1D eigenmodes appear in the energy window when the region is dominated by the hole band of one graphene layer and the electron band of the other layer. For the interlayer bias to be large enough and the Fermi energy to be in the corresponding region of the 1D eigenmodes such that $|E_F| \lesssim u$, we obtain the condition $\Delta/2 \gtrsim u$, i.e. $\Delta \gtrsim 200$ meV.

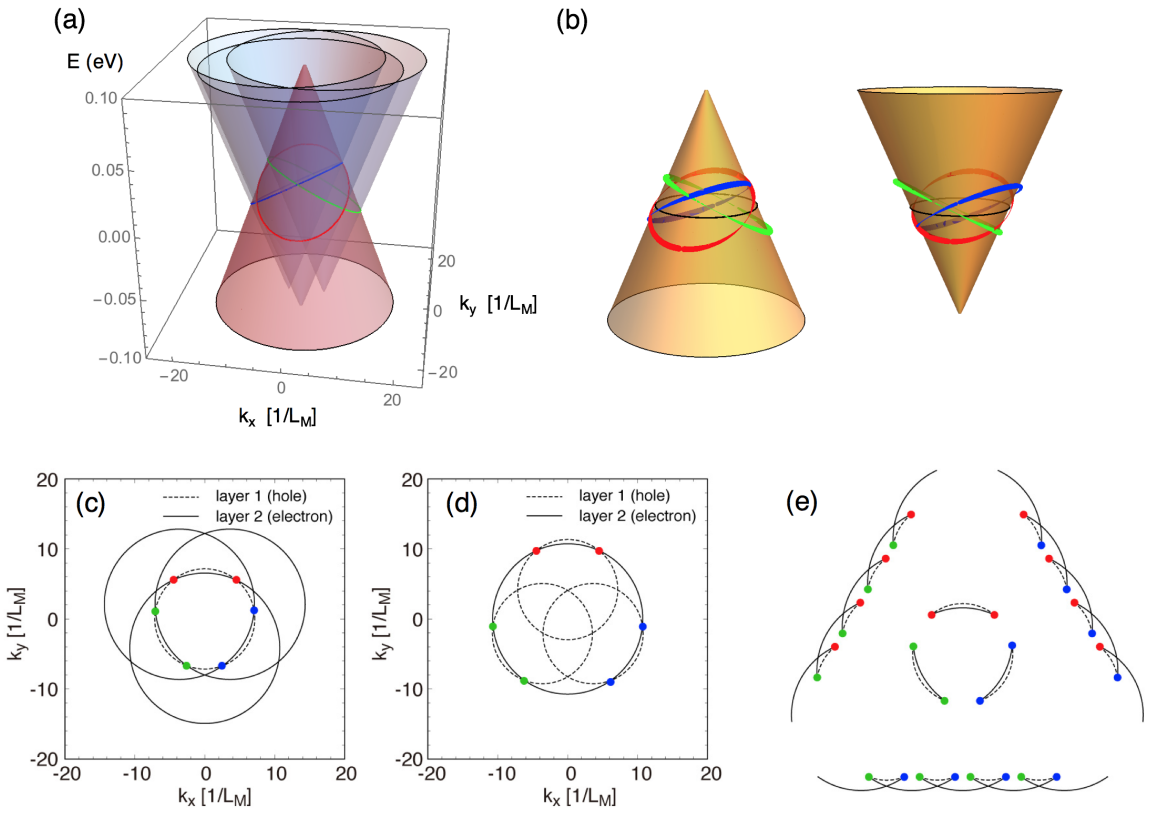

Figure 4.5: (a) Crossing lines between the Dirac cones, where three circles (red, blue and green) correspond to $j = 0, 1, 2$. Here we take $\theta = 0.3°$ and $\Delta = 200$ meV. (b) Amplitude of the interlayer matrix element on the crossing lines on the Dirac cones of layer 1 and 2. (c) and (d) Relative positions of the Fermi surfaces of layer 1 (dashed) and layer 2 (solid), in absence of u and at $E_F = 20$ meV. (e) The hybridised Fermi surfaces after the infinitesimal anticrossing. [Figure provided by Mikito Koshino.]

In the energy windows that are accessible by the interlayer bias, the Fermi surfaces consist of nestable Fermi lines [75] meaning these surfaces are connected via reciprocal lattice vectors. These 1D eigenmodes can be explained by understanding the reconstruction of the Fermi surface. Figures 4.5c and 4.5d illustrate the Fermi surfaces with no interaction between the layers, $u = 0$, and with Fermi energy $E_F = 20$ meV, which is slightly below the maximum energy of the crossing rings. Figure 4.5c shows the Fermi surface of the hole band from graphene layer 1 in dashed lines and the three solid black lines are Fermi surfaces for the electron band of layer 2 with the relative momentum shifts $\Delta \boldsymbol{K}_j (j = 0, 1, 2)$. Figure 4.5d shows the hole band of layer 1 centred instead. The hybridised Fermi surfaces after the anticrossing are shown in Fig. 4.5e. We see that three open Fermi surfaces are all related by a 120° rotation and there are also three closed pockets. When the interlayer interaction is turned on, the nesting between

the electron and hole parts of the closed pockets are gapped out of the constant energy plane as the Fermi surfaces are near an energy-momentum degeneracy and hybridise. In contrast, the open Fermi surfaces remain ungapped, which explains the origin of the 1D eigenmodes filling the gap.

From our calculations, the 1D eigenmodes propagate independently in three directions and never hybridise. This poses the question of how disorder plays a role in the system and how it affects electronic transport. In Fig. 4.1b, the independent 1D eigenmodes form a zigzag trajectory composed of straight lines along the AB-BA boundary and cornered angles in the AA regions. Hybridisation between different 1D eigenmodes can only occur when there is a local mixing of modes 1 and 2 on the AB-BA boundaries, or in the presence of an irregular reflection at the AA regions. In a real TBG lattice, the effect of lattice relaxation means that the moiré pattern exhibits a distorted triangular pattern with shifted AA spots and either extended or shortened AB-BA boundaries [87, 88, 89]. Despite this moiré-scale distortion across the lattice, we expect that this would not cause a strong mixing between different 1D eigenmodes because the local atomic structures of AA and AB/BA regions are not modified significantly, and as such, the 1D eigenmodes would still be confined to the AB-BA boundary and linked at the AA regions as the AB and BA regions are locally gapped out by the interlayer bias [95]. It is expected that major scatterings are only caused by a short-range disorder that is smaller than the local structures of the AB-BA boundary and the AA regions, which is about a few nm.

To conclude, the electronic transport is dominated by the ballistic transport through the 1D eigenmodes when the Fermi energy is in the energy window and scattering effects are neglected. In addition, it is expected that we do not have the Aharanov-Bohm (AB) oscillation in magnetic fields because the 1D eigenmodes are zigzag in shape and do not enclose triangular domains over the lattice, and thus do not cause any interference. Experiments have reported measurements on small-angle TBG in the presence of an interlayer bias, and a significant AB oscillation was observed [90, 91, 92]. We expect that magnetic oscillations take place when the perfect 1D eigenmodes are not well-formed because the bias is not large enough or the Fermi energy is not in the region of the energy windows, which may explain the experimental observations.

Chapter 5

Umklapp electron-phonon interaction

The moiré superlattice potential present in TBG makes it an interesting system to consider umklapp scattering. Umklapp scattering is a scattering process that allows wave vectors that fall outside of the first mBZ to be expressed as a wave vector inside the first mBZ by using the reciprocal lattice vectors. This chapter will present a calculation of the resistivity generated by umklapp scattering in which the Dirac electrons from the graphene layers in TBG interact with the superlattice potential to emit in-plane acoustic phonons. This work aims to quantify a specific mechanism for electron-phonon coupling where electrons tunnel from one graphene layer to another graphene layer whilst simultaneously transferring momentum to the superlattice. We consider processes that change the wave vector $\boldsymbol{k}$ or $\boldsymbol{k'}$ by absorbing or emitting a phonon with momentum $\boldsymbol{q}$, respectively,

$$\boldsymbol{k'} + \boldsymbol{q} \to \boldsymbol{k}, \tag{5.0.1}$$

$$\boldsymbol{k} \to \boldsymbol{q} + \boldsymbol{k'}. \tag{5.0.2}$$

Similarly, we also account for processes that change the wave vector to $\boldsymbol{k}$ or $\boldsymbol{k'}$ by emitting or absorbing a phonon with momentum $\boldsymbol{q}$, respectively,

$$\boldsymbol{k'} \to \boldsymbol{k} + \boldsymbol{q}, \tag{5.0.3}$$

$$\boldsymbol{k} + \boldsymbol{q} \to \boldsymbol{k'}. \tag{5.0.4}$$

We use the Boltzmann transport calculation to find the resistivity produced by the Umklapp scattering of electrons with acoustic phonon modes and show that the electron-phonon contribution to the resistivity is on the order of 1 Ω and hence, unlikely to be the dominant scattering mechanism producing resistivity. Here, we use $\hbar = k_B = 1$. The following will show the method for calculating the resistivity in TBG and we apply the same method to TDBG in section 5.5 where we find that the resistivity is also on the order of 1 Ω.

5.1 The Boltzmann transport equation

The linearised Boltzmann equation for the electron distribution function, $f^0_{\boldsymbol{k}}$, for a steady state system with a homogeneous electric field applied in the x-direction is given by

$$\left.\frac{\partial f^0_{\boldsymbol{k}}}{\partial t}\right|_{\text{field}} + \left.\frac{\partial f^0_{\boldsymbol{k}}}{\partial t}\right|_{\text{scattering}} = 0. \tag{5.1.1}$$

This can be written in terms of the collision integral $I\{\delta f_{\boldsymbol{k}}\}$ [96, 97], which is defined as the rate of change of the distribution function,

$$-e\boldsymbol{E}\cdot\boldsymbol{v}_{\boldsymbol{k}}\frac{\partial f^0_{\boldsymbol{k}}}{\partial \epsilon_{\boldsymbol{k}}} = I\{\delta f_{\boldsymbol{k}}\}. \tag{5.1.2}$$

The electron velocity is given by $\boldsymbol{v}_{\boldsymbol{k}} = \frac{\partial \epsilon_{\boldsymbol{k}}}{\partial \boldsymbol{k}} = sv\,(\cos\theta_{\boldsymbol{k}}, \sin\theta_{\boldsymbol{k}})$ where the band index $s = \pm 1$ is for the conduction and valence bands, respectively. In response to the electric field, electrons in a particular state in equilibrium will be perturbed by an unknown function of energy $\psi_{\boldsymbol{k}}$, hence, the electron distribution function can be expanded as

$$f(\boldsymbol{k}) = f_0(\epsilon_{\boldsymbol{k}}) + \delta f_{\boldsymbol{k}} \approx f_0(\epsilon_{\boldsymbol{k}} - \psi_k \cos\theta_{\boldsymbol{k}}) \approx f_0(\epsilon_{\boldsymbol{k}}) - \frac{\partial f_0(\epsilon_{\boldsymbol{k}})}{\partial \epsilon_{\boldsymbol{k}}}\psi_k \cos\theta_{\boldsymbol{k}}, \tag{5.1.3}$$

where the equilibrium electron distribution function is given by

$$f_0(\epsilon_{\boldsymbol{k}}) = \frac{1}{e^{(\epsilon-\epsilon_F/T)}+1}. \tag{5.1.4}$$

We neglect the hybridisation of the wave functions between the two layers in TBG and the two bilayers in TDBG and thus, we have a degeneracy factor of 8 that accounts for spin-valley degeneracy and layer degeneracy. Resistivity is obtained using

$$\frac{1}{\rho} = \frac{\boldsymbol{j}\cdot\boldsymbol{x}}{E} = \frac{8e}{E}\int \frac{d\boldsymbol{k}}{(2\pi)^2} f_{\boldsymbol{k}}\boldsymbol{v}_{\boldsymbol{k}}\cdot\boldsymbol{x}. \tag{5.1.5}$$

Substituting in the expanded electron distribution function and velocity gives

$$\begin{aligned}\frac{1}{\rho} &= \frac{8e}{E}\int \frac{d\boldsymbol{k}}{(2\pi)^2}\left(-\frac{\partial f_0(\epsilon_{\boldsymbol{k}})}{\partial \epsilon_{\boldsymbol{k}}}\psi_k \cos\theta_{\boldsymbol{k}}\right)(sv\cos\theta_{\boldsymbol{k}}) \\ &= \frac{2esv}{\pi^2}\int k dk d\theta_{\boldsymbol{k}} \cos^2\theta_{\boldsymbol{k}}\left(-\frac{\partial f_0(\epsilon_{\boldsymbol{k}})}{\partial \epsilon_{\boldsymbol{k}}}\psi_k\cos\theta_{\boldsymbol{k}}\right)\frac{\psi_k}{E}.\end{aligned} \tag{5.1.6}$$

We perform the integration at the Fermi level and approximate $-\partial f_0(\epsilon_{\boldsymbol{k}})/\partial\epsilon_{\boldsymbol{k}}$ using a Delta function because

$$-\frac{\partial f_0(\epsilon_{\boldsymbol{k}})}{\partial \epsilon_{\boldsymbol{k}}} = \frac{1}{T}\frac{e^{\frac{\epsilon_{\boldsymbol{k}}-\epsilon_F}{T}}}{\left(e^{\frac{\epsilon_{\boldsymbol{k}}-\epsilon_F}{T}}+1\right)^2} = \frac{f_0\left(\epsilon_{\boldsymbol{k}}\right)\left(1-f_0\left(\epsilon_{\boldsymbol{k}}\right)\right)}{T} \tag{5.1.7}$$

only has a non-zero numerator when we are at the Fermi energy. The resistivity is then obtained using

$$\frac{1}{\rho} = \frac{2esk_F}{\pi^2}\int d\theta_{\boldsymbol{k}}\cos^2\theta_{\boldsymbol{k}}\frac{\psi_k}{E}, \tag{5.1.8}$$

where ψ_k/E is found using the Boltzmann equation.

The collision integral includes 4 electron-phonon scattering processes between the states $\boldsymbol{k}$ and $\boldsymbol{k'}$, which conserve wave vector and energy. The collision integral can be split into two contributions with the same energy conservation delta functions such that $I = I_1 + I_2$. The first contribution describes processes that change the wave vector to $\boldsymbol{k}$ or $\boldsymbol{k'}$ as shown in Eqs. (5.0.1) and (5.0.2) to give the first term of the collision integral as

$$I_1 = 2\pi\sum_{\boldsymbol{k'},\boldsymbol{q}}\delta\left(\epsilon_{\boldsymbol{k}}-\epsilon_{\boldsymbol{k'}}-\omega_{\boldsymbol{q}}\right)\Big[\left|\langle\boldsymbol{k}|\hat{\boldsymbol{V}}|\boldsymbol{k'},\boldsymbol{q}\rangle\right|^2 f_{\boldsymbol{k'}}(1-f_{\boldsymbol{k}}) - \left|\langle\boldsymbol{k'},\boldsymbol{q}|\hat{\boldsymbol{V}}|\boldsymbol{k}\rangle\right|^2 f_{\boldsymbol{k}}(1-f_{\boldsymbol{k'}})\Big], \tag{5.1.9}$$

where the bras and kets denote the initial and final states, and the $\hat{\boldsymbol{V}}$ inside the bra-kets represent the electron-phonon interaction. Similarly, the second contribution to the collision integral originates from processes that change the wave vector to $\boldsymbol{k}$ or $\boldsymbol{k'}$ as shown in Eqs. (5.0.3) and (5.0.4) giving the contribution to the collision integral as

$$I_2 = 2\pi \sum_{\boldsymbol{k'},\boldsymbol{q}} \delta\left(\epsilon_{\boldsymbol{k}} - \epsilon_{\boldsymbol{k'}} + \omega_{\boldsymbol{q}}\right) \Big[\Big| \langle \boldsymbol{k}, \boldsymbol{q}|\hat{\boldsymbol{V}}|\boldsymbol{k'}\rangle \Big|^2 f_{\boldsymbol{k'}}(1 - f_{\boldsymbol{k}}) - \Big| \langle \boldsymbol{k'}|\hat{\boldsymbol{V}}|\boldsymbol{k}, \boldsymbol{q}\rangle \Big|^2 f_{\boldsymbol{k}}(1 - f_{\boldsymbol{k'}}) \Big]. \tag{5.1.10}$$

5.2 Electron-phonon interaction in TBG

In this work, we are interested in the interlayer electron-phonon interaction where an electron from one graphene layer scatters to the other graphene layer whilst absorbing or emitting a phonon. The interaction Hamiltonian with the phonon field in TBG can be described by considering small local deformations $\boldsymbol{u}(\boldsymbol{r})$ of the superlattice that produces umklapp electron-phonon scattering [98]. The deformations allow the Dirac electrons to emit or absorb in-plane acoustic phonons. The interacting Hamiltonian describing the electron-phonon interaction between the two graphene layers is given by

$$T_{\text{e-ph}} = w \sum_{j=0,1,2} e^{i(\boldsymbol{K}_\xi^j - \boldsymbol{K}_\xi^0)\cdot(\boldsymbol{r_0} + \boldsymbol{u}(\boldsymbol{r}))} \begin{pmatrix} 1 & e^{i\xi\frac{2\pi}{3}j} \\ e^{-i\xi\frac{2\pi}{3}j} & 1 \end{pmatrix}, \tag{5.2.1}$$

where we took the interlayer Hamiltonian of TBG in Eq. (2.1.3) and added a small in-plane local deformation $\boldsymbol{u}(\boldsymbol{r})$. The phonon displacement field is real and Hermitian, and can be written using the quantised phonon field operators,

$$\boldsymbol{u}(\boldsymbol{r}, t) = \sum_{\boldsymbol{q},\Lambda} \sqrt{\frac{1}{2A\rho_m \omega_{\boldsymbol{q},\Lambda}}} \left(\boldsymbol{\Pi}_{\boldsymbol{q},\Lambda} a_{\boldsymbol{q},\Lambda} e^{-i\omega_{\boldsymbol{q},\Lambda} t} + \boldsymbol{\Pi}_{-\boldsymbol{q},\Lambda} a^\dagger_{-\boldsymbol{q},\Lambda} e^{i\omega_{\boldsymbol{q},\Lambda} t} \right) e^{i\boldsymbol{q}\cdot\boldsymbol{r}}. \tag{5.2.2}$$

The polarisation of the phonon mode $\boldsymbol{\Pi}_{\boldsymbol{q},\Lambda}$ is either parallel ($\Lambda = \text{L}$) to or perpendicular ($\Lambda = \text{T}$) to the direction of phonon propagation such that $\boldsymbol{\Pi}_{\boldsymbol{q},L} = \boldsymbol{q}/q$ and $\boldsymbol{\Pi}_{\boldsymbol{q},T} = \boldsymbol{z} \times \boldsymbol{q}/q$ for longitudinal and transverse phonons, respectively. The graphene mass density is $\rho_m = 7.6 \times 10^{-7}$ kgm^{-2} and for acoustic phonons, the linear dispersion is

given by $\omega_{\boldsymbol{q},\Lambda} = c_\Lambda q$ where $c_L = 0.15$ eVÅ and $c_T = 0.09$ eVÅ [99]. We retain terms at first order in the displacements in Eq. (5.2.1) to give the electron-phonon interaction matrix,

$$T_{\text{e-ph}} = iw \sum_{j,\boldsymbol{q},\Lambda} \begin{pmatrix} 1 & e^{i\xi\frac{2\pi}{3}j} \\ e^{-i\xi\frac{2\pi}{3}j} & 1 \end{pmatrix} \sqrt{\frac{1}{2A\rho_m\omega_{\boldsymbol{q},\Lambda}}} \times \left\{ \boldsymbol{K}_\xi^j \cdot \left(\boldsymbol{\Pi}_{\boldsymbol{q},\Lambda} a_{\boldsymbol{q},\Lambda} e^{-i\omega_{\boldsymbol{q},\Lambda}t} + \boldsymbol{\Pi}_{-\boldsymbol{q},\Lambda} a^\dagger_{-\boldsymbol{q},\Lambda} e^{i\omega_{\boldsymbol{q},\Lambda}t} \right) \right\} e^{i\left(\boldsymbol{q}+\Delta\boldsymbol{K}_\xi^0 - \Delta\boldsymbol{K}_\xi^j\right)\cdot\boldsymbol{r}}. \quad (5.2.3)$$

5.3 Collision integral for TBG

In the collision integral in Eqs. (5.1.9) and (5.1.10), the interacting potential $\hat{\boldsymbol{V}}$ is sandwiched between the graphene wave functions to find the matrix elements. The wave functions are normalised to the area of the sample A, and account for the $\pm\Delta\boldsymbol{K}_\xi^0/2$ rotation to the top and bottom layers as described in section 2.1.1,

$$\psi(\boldsymbol{k}) = \frac{1}{\sqrt{2A}} \begin{pmatrix} 1 \\ s\xi e^{i\xi\theta_{\boldsymbol{k}}} \end{pmatrix} e^{i\left(\boldsymbol{k}\pm\frac{\Delta\boldsymbol{K}_\xi^0}{2}\right)\cdot\boldsymbol{r}}, \quad (5.3.1)$$

where s is the band index and the polar angle of momentum in the graphene plane is given by $\theta_{\boldsymbol{k}} = \arctan(k_x/k_y)$. The equilibrium phonon distribution is given by

$$N_{\boldsymbol{q}}^0 = \frac{1}{e^{\omega_{\boldsymbol{q},\Lambda}/T} - 1} \quad (5.3.2)$$

and the resulting transition amplitudes for the 4 scattering processes are

$$\left| \langle \boldsymbol{k}|\hat{\boldsymbol{V}}|\boldsymbol{k'},\boldsymbol{q}\rangle \right|^2 = \frac{w^2}{8A} \sum_{j,\Lambda} \left| 1 + s_i\xi e^{i\xi\left(\frac{2\pi}{3}j+\theta_{\boldsymbol{k'}}\right)} + s_f\xi e^{-i\xi\left(\theta_{\boldsymbol{k}}+\frac{2\pi}{3}j\right)} + s_i s_f \xi^2 e^{i\xi\left(\theta_{\boldsymbol{k'}}-\theta_{\boldsymbol{k}}\right)} \right|^2 \times \frac{\left(\boldsymbol{K}_\xi^j \cdot \boldsymbol{\Pi}_{\boldsymbol{q},\Lambda}\right)^2}{\rho_m\omega_{\boldsymbol{q},\Lambda}} N_{\boldsymbol{q}} \delta_{\boldsymbol{q},\boldsymbol{k}-\boldsymbol{k'}+\Delta\boldsymbol{K}_\xi^j}, \quad (5.3.3)$$

$$\left|\langle \boldsymbol{k'},\boldsymbol{q}|\hat{\boldsymbol{V}}|\boldsymbol{k}\rangle\right|^2 = \frac{w^2}{8A}\sum_{j,\Lambda}\left|1+s_i\xi e^{i\xi\left(\frac{2\pi}{3}j+\theta_{\boldsymbol{k}}\right)}+s_f\xi e^{-i\xi\left(\theta_{\boldsymbol{k'}}+\frac{2\pi}{3}j\right)}+s_is_f\xi^2e^{i\xi\left(\theta_{\boldsymbol{k}}-\theta_{\boldsymbol{k'}}\right)}\right|^2 \times \frac{\left(\boldsymbol{K}^j_\xi\cdot\boldsymbol{\Pi}_{-\boldsymbol{q},\Lambda}\right)^2}{\rho_m\omega_{\boldsymbol{q},\Lambda}}\left(N_{\boldsymbol{q}}+1\right)\delta_{\boldsymbol{q},\boldsymbol{k}-\boldsymbol{k'}+\Delta\boldsymbol{K}^j_\xi}, \quad (5.3.4)$$

$$\left|\langle \boldsymbol{k},\boldsymbol{q}|\hat{\boldsymbol{V}}|\boldsymbol{k'}\rangle\right|^2 = \frac{w^2}{8A}\sum_{j,\Lambda}\left|1+s_i\xi e^{i\xi\left(\frac{2\pi}{3}j+\theta_{\boldsymbol{k'}}\right)}+s_f\xi e^{-i\xi\left(\theta_{\boldsymbol{k}}+\frac{2\pi}{3}j\right)}+s_is_f\xi^2e^{i\xi\left(\theta_{\boldsymbol{k'}}-\theta_{\boldsymbol{k}}\right)}\right|^2 \times \frac{\left(\boldsymbol{K}^j_\xi\cdot\boldsymbol{\Pi}_{-\boldsymbol{q},\Lambda}\right)^2}{\rho_m\omega_{\boldsymbol{q},\Lambda}}\left(N_{\boldsymbol{q}}+1\right)\delta_{\boldsymbol{q},\boldsymbol{k'}-\boldsymbol{k}+\Delta\boldsymbol{K}^j_\xi}, \quad (5.3.5)$$

$$\left|\langle \boldsymbol{k'}|\hat{\boldsymbol{V}}|\boldsymbol{k},\boldsymbol{q}\rangle\right|^2 = \frac{w^2}{8A}\sum_{j,\Lambda}\left|1+s_i\xi e^{i\xi\left(\frac{2\pi}{3}j+\theta_{\boldsymbol{k}}\right)}+s_f\xi e^{-i\xi\left(\theta_{\boldsymbol{k'}}+\frac{2\pi}{3}j\right)}+s_is_f\xi^2e^{i\xi\left(\theta_{\boldsymbol{k}}-\theta_{\boldsymbol{k'}}\right)}\right|^2 \times \frac{\left(\boldsymbol{K}^j_\xi\cdot\boldsymbol{\Pi}_{\boldsymbol{q},\Lambda}\right)^2}{\rho_m\omega_{\boldsymbol{q},\Lambda}}N_{\boldsymbol{q}}\delta_{\boldsymbol{q},\boldsymbol{k'}-\boldsymbol{k}+\Delta\boldsymbol{K}^j_\xi}. \quad (5.3.6)$$

We simplify the contributions to the collision integral in Eqs. (5.1.9) and (5.1.10) using $\left(\boldsymbol{K}^j_\xi\cdot\boldsymbol{\Pi}_{\boldsymbol{q},\Lambda}\right)^2=\left(\boldsymbol{K}^j_\xi\cdot\boldsymbol{\Pi}_{-\boldsymbol{q},\Lambda}\right)^2$, and convert the sum over $\boldsymbol{k'}$ to an integral. This gives

$$I_1 = 2\pi\int\frac{d\boldsymbol{k'}}{(2\pi)^2}\sum_{\boldsymbol{q},j,\Lambda}\frac{w^2}{8}\frac{\left(\boldsymbol{K}^j_\xi\cdot\boldsymbol{\Pi}_{\boldsymbol{q},\Lambda}\right)^2\left|1+s_i\xi e^{i\xi\left(\frac{2\pi}{3}j+\theta_{\boldsymbol{k'}}\right)}+s_f\xi e^{-i\xi\left(\theta_{\boldsymbol{k}}+\frac{2\pi}{3}j\right)}+s_is_f\xi^2e^{i\xi\left(\theta_{\boldsymbol{k'}}-\theta_{\boldsymbol{k}}\right)}\right|^2}{\rho_m\omega_{\boldsymbol{q},\Lambda}} \times\delta\left(\epsilon_{\boldsymbol{k}}-\epsilon_{\boldsymbol{k'}}-\omega_{\boldsymbol{q},\Lambda}\right)\delta_{\boldsymbol{q},\boldsymbol{k}-\boldsymbol{k'}+\Delta\boldsymbol{K}^j_\xi}\left[N_{\boldsymbol{q}}f_{\boldsymbol{k'}}\left(1-f_{\boldsymbol{k}}\right)-\left(N_{\boldsymbol{q}}+1\right)f_{\boldsymbol{k}}\left(1-f_{\boldsymbol{k'}}\right)\right], \quad (5.3.7)$$

$$I_2 = 2\pi\int\frac{d\boldsymbol{k'}}{(2\pi)^2}\sum_{\boldsymbol{q},j,\Lambda}\frac{w^2}{8}\frac{\left(\boldsymbol{K}^j_\xi\cdot\boldsymbol{\Pi}_{\boldsymbol{q},\Lambda}\right)^2\left|1+s_i\xi e^{i\xi\left(\frac{2\pi}{3}j+\theta_{\boldsymbol{k'}}\right)}+s_f\xi e^{-i\xi\left(\theta_{\boldsymbol{k}}+\frac{2\pi}{3}j\right)}+s_is_f\xi^2e^{i\xi\left(\theta_{\boldsymbol{k'}}-\theta_{\boldsymbol{k}}\right)}\right|^2}{\rho_m\omega_{\boldsymbol{q},\Lambda}} \times\delta\left(\epsilon_{\boldsymbol{k}}-\epsilon_{\boldsymbol{k'}}+\omega_{\boldsymbol{q},\Lambda}\right)\delta_{\boldsymbol{q},\boldsymbol{k'}-\boldsymbol{k}+\Delta\boldsymbol{K}^j_\xi}\left[\left(N_{\boldsymbol{q}}+1\right)f_{\boldsymbol{k'}}\left(1-f_{\boldsymbol{k}}\right)-N_{\boldsymbol{q}}f_{\boldsymbol{k}}\left(1-f_{\boldsymbol{k'}}\right)\right]. \quad (5.3.8)$$

Note that the collision integral vanishes when the distribution functions are the equilibrium ones. To prove this, we can look at I_1 in Eq. (5.3.7) and substitute the equilibrium distributions, $f^0_{\boldsymbol{k}}$ and $N^0_{\boldsymbol{q}}$, to show that it goes to zero (similarly with I_2),

$$\delta\left(\epsilon_{\boldsymbol{k}}-\epsilon_{\boldsymbol{k'}}-\omega_{\boldsymbol{q},\Lambda}\right)\left[N_{\boldsymbol{q}}^{0}f_{\boldsymbol{k'}}^{0}\left(1-f_{\boldsymbol{k}}^{0}\right)-\left(N_{\boldsymbol{q}}^{0}+1\right)f_{\boldsymbol{k}}^{0}\left(1-f_{\boldsymbol{k'}}^{0}\right)\right]$$
$$=\left(\frac{1}{e^{\omega_{\boldsymbol{q},\Lambda}/T}-1}\right)\left(\frac{1}{e^{\left(\epsilon_{\boldsymbol{k}}-\omega_{\boldsymbol{q},\Lambda}\right)/T}+1}\right)\left(\frac{e^{\epsilon_{\boldsymbol{k}}/T}}{e^{\epsilon_{\boldsymbol{k}}/T}+1}\right)$$
$$-\left(\frac{e^{\omega_{\boldsymbol{q},\Lambda}/T}}{e^{\omega_{\boldsymbol{q},\Lambda}/T}-1}\right)\left(\frac{1}{e^{\epsilon_{\boldsymbol{k}}/T}+1}\right)\left(\frac{e^{\left(\epsilon_{\boldsymbol{k}}-\omega_{\boldsymbol{q},\Lambda}\right)/T}}{e^{\left(\epsilon_{\boldsymbol{k}}-\omega_{\boldsymbol{q},\Lambda}\right)/T}+1}\right)=0. \quad (5.3.9)$$

This means we can study the collision integral close to equilibrium distributions. If we are not in equilibrium, we can write the electron distribution function as the combination of the equilibrium distribution function and a perturbation as shown in Eq. (5.1.3). This is substituted into the collision integral such that the square brackets in I_1 and I_2 (Eqs. (5.3.7) and (5.3.8)) are $\delta f_{\boldsymbol{k'}}\left(N_{\boldsymbol{q}}+f_{\boldsymbol{k}}^{0}\right)-\delta f_{\boldsymbol{k}}\left(N_{\boldsymbol{q}}+1-f_{\boldsymbol{k'}}^{0}\right)$ and $\delta f_{\boldsymbol{k'}}\left(N_{\boldsymbol{q}}+1-f_{\boldsymbol{k}}^{0}\right)-\delta f_{\boldsymbol{k}}\left(N_{\boldsymbol{q}}+f_{\boldsymbol{k'}}^{0}\right)$, respectively.

Using Eq. (5.1.7), we obtain $\delta f_{\boldsymbol{k}}=f_0\left(\epsilon_{\boldsymbol{k}}\right)\left(1-f_0\left(\epsilon_{\boldsymbol{k}}\right)\right)\psi_{\boldsymbol{k}}/T$, and this is substituted into the collision integral. Phonon absorption and emission is accounted for using $\eta=\pm1$, and the full collision integral [96, 97] is given by

$$I=\int\frac{d\boldsymbol{k'}}{(2\pi)^2}\sum_{\boldsymbol{q},j,\Lambda,\eta}W_{\boldsymbol{k'},\boldsymbol{q}}\frac{\partial N_0\left(w_{\boldsymbol{q},\Lambda}\right)}{\partial w_{\boldsymbol{q},\Lambda}}\left(f_0\left(\epsilon_{\boldsymbol{k}}\right)-f_0\left(\epsilon_{\boldsymbol{k'}}\right)\right)\left(\psi_{\boldsymbol{k'}}-\psi_{\boldsymbol{k}}\right)\eta\delta\left(\epsilon_{\boldsymbol{k}}-\epsilon_{\boldsymbol{k'}}+\eta\omega_{\boldsymbol{q},\Lambda}\right), \quad (5.3.10)$$

$$W_{\boldsymbol{k'},\boldsymbol{q}}=\frac{\pi w^2}{4}\frac{\left(\boldsymbol{K}_{\xi}^{j}\cdot\boldsymbol{\Pi}_{\boldsymbol{q},\Lambda}\right)^2\left|1+s_i\xi e^{i\xi\left(\frac{2\pi}{3}j+\theta_{\boldsymbol{k'}}\right)}+s_f\xi e^{-i\xi\left(\theta_{\boldsymbol{k}}+\frac{2\pi}{3}j\right)}+s_is_f\xi^2e^{i\xi\left(\theta_{\boldsymbol{k'}}-\theta_{\boldsymbol{k}}\right)}\right|^2}{\rho_m\omega_{\boldsymbol{q},\Lambda}}, \quad (5.3.11)$$

$$\boldsymbol{q}=\boldsymbol{k}-\boldsymbol{k'}+\eta\Delta\boldsymbol{K}_{\xi}^{j}. \quad (5.3.12)$$

We simplify the collision integral further using

$$f_0\left(\epsilon_{\boldsymbol{k}}\right)-f_0\left(\epsilon_{\boldsymbol{k'}}\right)=f_0\left(\epsilon_{\boldsymbol{k}}\right)-f_0\left(\epsilon_{\boldsymbol{k}}+\eta\omega_{\boldsymbol{q},\Lambda}\right)\approx-\eta\omega_{\boldsymbol{q},\Lambda}\frac{\partial f_0\left(\epsilon_{\boldsymbol{k}}\right)}{\partial\epsilon_{\boldsymbol{k}}}, \quad (5.3.13)$$

to obtain

$$I = \int \frac{d\boldsymbol{k'}}{(2\pi)^2} \sum_{\boldsymbol{q},j,\Lambda,\eta} W_{\boldsymbol{k'},\boldsymbol{q}} \frac{\partial N_0\left(w_{\boldsymbol{q},\Lambda}\right)}{\partial w_{\boldsymbol{q},\Lambda}} \left(-\omega_{\boldsymbol{q},\Lambda} \frac{\partial f_0\left(\epsilon_{\boldsymbol{k}}\right)}{\partial \epsilon_{\boldsymbol{k}}}\right) \left(\psi_{\boldsymbol{k'}} - \psi_{\boldsymbol{k}}\right) \delta\left(\epsilon_{\boldsymbol{k}} - \epsilon_{\boldsymbol{k'}} + \eta\omega_{\boldsymbol{q},\Lambda}\right). \tag{5.3.14}$$

We substitute this into the Boltzmann equation in Eq. (5.1.2) and assume that the phonon energy is negligible such that $\sum_\eta \delta\left(\epsilon_{\boldsymbol{k}} - \epsilon_{\boldsymbol{k'}} + \eta\omega_{\boldsymbol{q},\Lambda}\right) \approx 2\delta(k-k')/v$, where the graphene dispersion is $\epsilon_{\boldsymbol{k}} = vk$. This gives

$$eEsv\cos\theta_{\boldsymbol{k}} = \int \frac{2}{v} \frac{k_F d\theta_{\boldsymbol{k'}}}{(2\pi)^2} \sum_{vectq,j,\Lambda} W_{\boldsymbol{k'},\boldsymbol{q}} \frac{\partial N_0\left(\omega_{\boldsymbol{q},\Lambda}\right)}{\partial \omega_{\boldsymbol{q},\Lambda}} \omega_{\boldsymbol{q},\Lambda} \left(\psi_{k'}\cos\theta_{\boldsymbol{k'}} - \psi_k \cos\theta_{\boldsymbol{k}}\right). \tag{5.3.15}$$

The delta function requires that $k = k'$ meaning we assume $\psi_k \approx \psi_{k'}$, and Eq. (5.3.15) can be rewritten as

$$\frac{E}{\psi_k} = \int \frac{k_F d\theta_{\boldsymbol{k'}}}{2\pi^2 esv^2} \sum_{\boldsymbol{q},j,\Lambda} W_{\boldsymbol{k'},\boldsymbol{q}} \frac{\partial N_0\left(\omega_{\boldsymbol{q},\Lambda}\right)}{\partial \omega_{\boldsymbol{q},\Lambda}} \omega_{\boldsymbol{q},\Lambda} \left(\frac{\cos\theta_{\boldsymbol{k'}}}{\cos\theta_{\boldsymbol{k}}} - 1\right). \tag{5.3.16}$$

5.4 Analytical expression for resistivity

To find an analytical expression, we take $T > \omega_{\boldsymbol{q},\Lambda}$ so that $\partial N_0\left(\omega_{\boldsymbol{q},\Lambda}\right)/\partial\omega_{\boldsymbol{q},\Lambda} = -T/\omega^2_{\boldsymbol{q},\Lambda}$. In the limit of $\Delta\boldsymbol{K}^j_\xi \gg \boldsymbol{k}, \boldsymbol{k'}$, the phonon wave vector is on the same order of magnitude as the moiré reciprocal lattice vectors, i.e. $\boldsymbol{q} \sim \Delta\boldsymbol{K}^j_\xi$. Applying these assumptions gives us an integral that can be calculated analytically. Taking $s_i = s_f = 1$ and $\xi = 1$ for the scattering between conduction bands in the K valley, we obtain

$$\frac{E}{\psi_k} = \frac{\pi w^2}{4} \int \frac{k_F d\theta_{\boldsymbol{k'}}}{2\pi^2 esv^2\rho_m} \sum_{j,\eta,\Lambda} \left(\boldsymbol{K}^j_\xi \cdot \boldsymbol{\Pi}_{\boldsymbol{q},\Lambda}\right)^2 \left|1 + e^{i\left(\frac{2\pi}{3}j + \theta_{\boldsymbol{k'}}\right)} + e^{-i\left(\theta_{\boldsymbol{k}} + \frac{2\pi}{3}j\right)} + e^{i\left(\theta_{\boldsymbol{k'}} - \theta_{\boldsymbol{k}}\right)}\right|^2 \times \frac{T}{\omega^2_{\boldsymbol{q},\Lambda}} \left(1 - \frac{\cos\theta_{\boldsymbol{k'}}}{\cos\theta_{\boldsymbol{k}}}\right). \tag{5.4.1}$$

Using

$$\omega^2_{\boldsymbol{q},\Lambda} \approx c^2_\Lambda (\Delta K)^2, \text{ and } \left(\boldsymbol{K}^j_\xi \cdot \boldsymbol{\Pi}_{\boldsymbol{q},\Lambda}\right)^2 = \begin{cases} 0 & \text{for } \Lambda = L \\ K^2 & \text{for } \Lambda = T \end{cases}, \tag{5.4.2}$$

gives the resistivity in SI units as

$$\rho = \frac{9w^2\pi K^2 k_B \hbar T}{8e^2 v^2 \rho_m c_T^2 (\Delta K)^2}. \tag{5.4.3}$$

For high temperatures, resistivity is inversely proportional to the square of the twist angle θ,

$$\rho = \frac{9w^2\pi k_B \hbar T}{8e^2 v^2 \rho_m c_T^2 \theta^2}, \tag{5.4.4}$$

and is on the order of 1 Ω. Figure 5.1 shows the linear dependence of resistivity with temperature for a twist angle of $\theta = 3°$ suggesting that the umklapp electron-phonon process make a small contribution to resistivity in TBG.

5.5 Resistivity in TDBG

Using the same method as for TBG, we look at the resistivity generated by umklapp electron-phonon scattering processes in TDBG by using the low-energy bilayer graphene wave function [48], which accounts for the non-dimer sites in the system and is given by

$$\psi(\boldsymbol{k}) = \frac{1}{\sqrt{2A}} \begin{pmatrix} 1 \\ 0 \\ 0 \\ s\xi e^{i2\xi\theta_{\boldsymbol{k}}} \end{pmatrix} e^{i\left(\boldsymbol{k} \pm \frac{\Delta \boldsymbol{K}_\xi^0}{2}\right)\cdot \boldsymbol{r}}. \tag{5.5.1}$$

Using the same method as for TBG in Eq. (5.4.1), E/ψ_k is given by

$$\frac{E}{\psi_k} = \frac{\pi w^2}{4} \int \frac{k_F d\theta_{\boldsymbol{k'}}}{2\pi^2 e s v^2 \rho_m} \sum_{j,\eta,\Lambda} \left(\boldsymbol{K}_\xi^j \cdot \boldsymbol{\Pi}_{\boldsymbol{q},\Lambda}\right)^2 \left|\xi e^{-i\xi\left(2\theta_{\boldsymbol{k'}} + \frac{2\pi}{3}j\right)}\right|^2 \frac{T}{\omega_{\boldsymbol{q},\Lambda}^2} \left(1 - \frac{\cos\theta_{\boldsymbol{k'}}}{\cos\theta_{\boldsymbol{k}}}\right). \tag{5.5.2}$$

Using Eq. (5.1.8) and following the same method as for TBG, we obtain the resistivity as

$$\rho = \frac{3w^2\pi k_B \hbar T}{8e^2 v^2 \rho_m c_T^2 \theta^2}, \tag{5.5.3}$$

which is also on the order of 1 Ω as shown in Fig. 5.1. This chapter concludes that for both TBG and TDBG, the contribution to resistivity from a specific mechanism

of electron-phonon scattering where an electron tunnels from one layer to another layer while transferring momentum to the superlattice is unlikely to be the dominant scattering process generating resistivity, even at room temperature. In graphene/hBN superlattices, it was shown that umklapp electron-electron scattering was the dominant scattering mechanism [98], which could be the subject of further study.

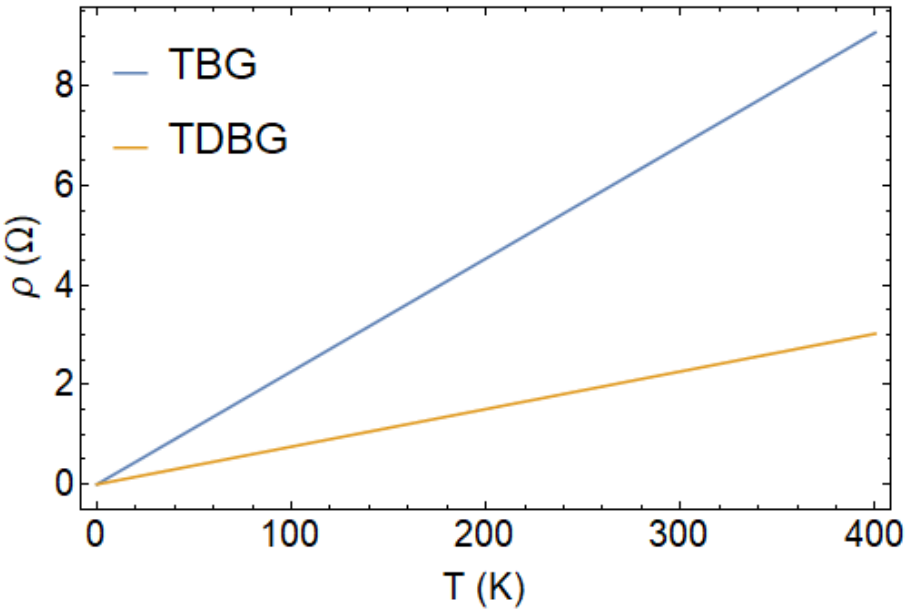

Figure 5.1: Resistivity as a function of temperature in TBG and TDBG with twist angle $\theta = 3°$. For both heterostructures, the resistivity is on the order of 1 Ω.

Chapter 6

Conclusions

The work in this thesis is dedicated to the electronic properties of few-layer twistronic graphene. The first part of the thesis introduces the continuum-model Hamiltonian for twisted bilayer graphene and the theory is extended to both twisted double bilayer graphene and twisted monolayer-bilayer graphene. The resulting electronic miniband spectra are presented for both with and without a perpendicular electric field.

Moreover, we have investigated twisted bilayer graphene at relatively large angles of approximately 2° with the transverse magnetic focusing effect. The theoretical work supports the experimental manifestation of micrometre-scale ballistic transport in the system and allowed us to probe the band structure of the material. In addition, we studied the system in the presence of a perpendicular electric field and found that the breaking of the layer degeneracy causes minivalley splitting and allows selective focusing originating from different minivalleys, which is of interest for using this degree of freedom in valleytronics.

Furthermore, we looked at small-angle twisted bilayer graphene below 1° with a large potential asymmetry between the top and bottom layers. We found that for sufficiently large biases, two well-defined energy windows form on either side of zero energy, which contain one-dimensional eigenmodes. We found that the perpendicular electric field causes the AB and BA regions in the lattice to be locally gapped out to create a network of one-dimensional states at the domain boundaries. We showed that the topological channels do not form a percolating network, but instead, the one-dimensional eigenmodes propagate independently in three different directions.

Finally, we present an analytical calculation of umklapp electron-phonon interaction in twisted bilayer graphene and twisted double bilayer graphene. We conclude that despite being possible, it is unlikely that this is the dominant scattering mechanism generating resistivity in these systems, even at room temperature. It would be interesting to study umklapp electron-electron interactions in future works as this was shown to be the dominant scattering mechanism in graphene/hBN superlattices.

Bibliography

[1] K. S. Novoselov, A. K. Geim, S. V. Morozov, D. E. Jiang, Y. Zhang, S. V. Dubonos, I. V. Grigorieva, and A. A. Firsov. Electric field effect in atomically thin carbon films. *Science*, 306(5696):666–669, 2004.

[2] A. K. Geim and K. S. Novoselov. The rise of graphene. In *Nanoscience and technology: a collection of reviews from nature journals*, pages 11–19. World Scientific, 2010.

[3] A. K. Geim and I. V. Grigorieva. Van der Waals heterostructures. *Nature*, 499(7459):419–425, 2013.

[4] K. S. Novoselov, A. Mishchenko, A. Carvalho, and A. H. Castro Neto. 2D materials and van der Waals heterostructures. *Science*, 353(6298), 2016.

[5] C. R. Dean, A. F. Young, I. Meric, C. Lee, L. Wang, S. Sorgenfrei, K. Watanabe, T. Taniguchi, P. Kim, K. L. Shepard, and J. Hone. Boron nitride substrates for high-quality graphene electronics. *Nature Nanotechnology*, 5(10):722–726, 2010.

[6] M. Yankowitz, Q. Ma, P. Jarillo-Herrero, and B. J. LeRoy. van der Waals heterostructures combining graphene and hexagonal boron nitride. *Nature Reviews Physics*, 1(2):112–125, 2019.

[7] C. R. Dean, L. Wang, P. Maher, C. Forsythe, F. Ghahari, Y. Gao, J. Katoch, M. Ishigami, P. Moon, M. Koshino, T. Taniguchi, K. Watanabe, K. L. Shepard, J. Hone, and P. Kim. Hofstadter's butterfly and the fractal quantum Hall effect in moiré superlattices. *Nature*, 497(7451):598–602, 2013.

[8] B. Hunt, J. D. Sanchez-Yamagishi, A. F. Young, M. Yankowitz, B. J. LeRoy, K. Watanabe, T. Taniguchi, P. Moon, M. Koshino, P. Jarillo-Herrero, and R. C. Ashoori. Massive Dirac fermions and hofstadter butterfly in a van der Waals heterostructure. *Science*, 340(6139):1427–1430, 2013.

[9] Y. Cao, V. Fatemi, S. Fang, K. Watanabe, T. Taniguchi, E. Kaxiras, and P. Jarillo-Herrero. Unconventional superconductivity in magic-angle graphene superlattices. *Nature*, 556(7699):43–50, 2018.

[10] Y. Cao, V. Fatemi, A. Demir, S. Fang, S. L. Tomarken, J. Y. Luo, J. D. Sanchez-Yamagishi, K. Watanabe, T. Taniguchi, E. Kaxiras, R. C. Ashoori, and P. Jarillo-Herrero. Correlated insulator behaviour at half-filling in magic-angle graphene superlattices. *Nature*, 556(7699):80–84, 2018.

[11] M. Yankowitz, S. Chen, H. Polshyn, Y. Zhang, K. Watanabe, T. Taniguchi, D. Graf, A. F. Young, and C. R. Dean. Tuning superconductivity in twisted bilayer graphene. *Science*, 363(6431):1059–1064, 2019.

[12] R. Bistritzer and A. H. MacDonald. Moiré bands in twisted double-layer graphene. *Proceedings of the National Academy of Sciences*, 108(30):12233–12237, 2011.

[13] G. Li, A. Luican, J. M. B. Lopes Dos Santos, A. H. Castro Neto, A. Reina, J. Kong, and E. Y. Andrei. Observation of van Hove singularities in twisted graphene layers. *Nature Physics*, 6(2):109–113, 2010.

[14] W. Yan, M. Liu, R. F. Dou, L. Meng, L. Feng, Z. D. Chu, Y. Zhang, Z. Liu, J. C. Nie, and L. He. Angle-dependent van Hove singularities in a slightly twisted graphene bilayer. *Physical Review Letters*, 109(12):126801, 2012.

[15] I. Brihuega, P. Mallet, H. González-Herrero, G. Trambly de Laissardière, M. M. Ugeda, L. Magaud, J. M. Gómez-Rodríguez, F. Ynduráin, and J. Y. Veuillen. Unraveling the intrinsic and robust nature of van Hove singularities in twisted bilayer graphene by scanning tunneling microscopy and theoretical analysis. *Physical Review Letters*, 109(19):196802, 2012.

[16] E. Y. Andrei and A. H. MacDonald. Graphene bilayers with a twist. *Nature Materials*, 19(12):1265–1275, 2020.

[17] Hennrik Schmidt, Johannes C Rode, Dmitri Smirnov, and Rolf J Haug. Superlattice structures in twisted bilayers of folded graphene. *Nat. Commun.*, 5, 2014.

[18] A. I. Berdyugin, B. Tsim, P. Kumaravadivel, S. G. Xu, A. Ceferino, A. Knothe, R. K. Kumar, T. Taniguchi, K. Watanabe, A. K. Geim, I. V. Grigorieva, and V. I. Fal'ko. Minibands in twisted bilayer graphene probed by magnetic focusing. *Science Advances*, 6(16), 2020.

[19] K. Kim, A. DaSilva, S. Huang, B. Fallahazad, S. Larentis, T. Taniguchi, K. Watanabe, B. J. LeRoy, A. H. MacDonald, and E. Tutuc. Tunable moiré bands and strong correlations in small-twist-angle bilayer graphene. *Proceedings of the National Academy of Sciences*, 114(13):3364–3369, 2017.

[20] S. Huang, K. Kim, D. K. Efimkin, T. Lovorn, T. Taniguchi, K. Watanabe, A. H. MacDonald, E. Tutuc, and B. J. LeRoy. Topologically protected helical states in minimally twisted bilayer graphene. *Physical Review Letters*, 121(3):037702, 2018.

[21] J. M. B. Lopes dos Santos, N. M. R. Peres, and A. H. Castro Neto. Graphene bilayer with a twist: electronic structure. *Physical Review Letters*, 99(25):256802, 2007.

[22] E. J. Mele. Commensuration and interlayer coherence in twisted bilayer graphene. *Physical Review B*, 81(16):161405, 2010.

[23] G. Trambly de Laissardière, D. Mayou, and L. Magaud. Localization of dirac electrons in rotated graphene bilayers. *Nano Letters*, 10(3):804–808, 2010.

[24] S. Shallcross, S. Sharma, E. Kandelaki, and O. A. Pankratov. Electronic structure of turbostratic graphene. *Physical Review B*, 81(16):165105, 2010.

[25] E. S. Morell, J. D. Correa, P. Vargas, M. Pacheco, and Z. Barticevic. Flat bands in slightly twisted bilayer graphene: tight-binding calculations. *Physical Review B*, 82(12):121407, 2010.

[26] M. Kindermann and P. N. First. Local sublattice-symmetry breaking in rotationally faulted multilayer graphene. *Physical Review B*, 83(4):045425, 2011.

[27] J. M. B. Lopes dos Santos, N. M. R. Peres, and A. H. Castro Neto. Continuum model of the twisted graphene bilayer. *Physical Review B*, 86:155449, 2012.

[28] P. Moon and M. Koshino. Energy spectrum and quantum Hall effect in twisted bilayer graphene. *Physical Review B*, 85:195458, May 2012.

[29] G. Trambly de Laissardière, D. Mayou, and L. Magaud. Numerical studies of confined states in rotated bilayers of graphene. *Physical Review B*, 86(12):125413, 2012.

[30] E. J. Mele. Band symmetries and singularities in twisted multilayer graphene. *Physical Review B*, 84:235439, 2011.

[31] P. Moon and M. Koshino. Optical absorption in twisted bilayer graphene. *Physical Review B*, 87:205404, 2013.

[32] M. Koshino. Interlayer interaction in general incommensurate atomic layers. *New J. Phys.*, 17(1):015014, 2015.

[33] M. Koshino and P. Moon. Electronic properties of incommensurate atomic layers. *Journal of the Physical Society of Japan*, 84(12):121001, 2015.

[34] A. Garcia-Ruiz, H. Y. Deng, V. V. Enaldiev, and V. I. Fal'ko. Full Slonczewski-Weiss-McClure parametrization of few-layer twistronic graphene. *Physical Review B*, 104(8):085402, 2021.

[35] M. Koshino, N. F. Q. Yuan, T. Koretsune, M. Ochi, K. Kuroki, and L. Fu. Maximally localized wannier orbitals and the extended Hubbard model for twisted bilayer graphene. *Physical Review X*, 8(3):031087, 2018.

[36] G. Tarnopolsky, A. J. Kruchkov, and A. Vishwanath. Origin of magic angles in twisted bilayer graphene. *Physical Review Letters*, 122(10):106405, 2019.

[37] N. N. T. Nam and M. Koshino. Lattice relaxation and energy band modulation in twisted bilayer graphene. *Physical Review B*, 96(7):075311, 2017.

[38] G. W. Burg, J. Zhu, T. Taniguchi, K. Watanabe, A. H. MacDonald, and E. Tutuc. Correlated insulating states in twisted double bilayer graphene. *Physical Review Letters*, 123(19):197702, 2019.

[39] C. Shen, Y. Chu, Q. S. Wu, N. Li, S. Wang, Y. Zhao, J. Tang, J. Liu, J. Tian, K. Watanabe, T. Taniguchi, R. Yang, Z. Y. Meng, D. Shi, O. V. Yazyev, and G. Zhang. Correlated states in twisted double bilayer graphene. *Nature Physics*, 16(5):520–525, 2020.

[40] Y. Cao, D. Rodan-Legrain, O. Rubies-Bigorda, J. M. Park, K. Watanabe, T. Taniguchi, and P. Jarillo-Herrero. Tunable correlated states and spin-polarized phases in twisted bilayer-bilayer graphene. *Nature*, 583(7815):215–220, 2020.

[41] X. Liu, Z. Hao, E. Khalaf, J. Y. Lee, Y. Ronen, H. Yoo, D. H. Najafabadi, K. Watanabe, T. Taniguchi, A. Vishwanath, and P. Kim. Tunable spin-polarized correlated states in twisted double bilayer graphene. *Nature*, 583(7815):221–225, 2020.

[42] M. Koshino. Band structure and topological properties of twisted double bilayer graphene. *Physical Review B*, 99(23):235406, 2019.

[43] N. R. Chebrolu, B. L. Chittari, and J. Jung. Flat bands in twisted double bilayer graphene. *Physical Review B*, 99(23):235417, 2019.

[44] Y. W. Choi and H. J. Choi. Intrinsic band gap and electrically tunable flat bands in twisted double bilayer graphene. *Physical Review B*, 100(20):201402, 2019.

[45] J. Y. Lee, E. Khalaf, S. Liu, X. Liu, Z. Hao, P. Kim, and A. Vishwanath. Theory of correlated insulating behaviour and spin-triplet superconductivity in twisted double bilayer graphene. *Nature Communications*, 10(1):1–10, 2019.

[46] F. J. Culchac, R. R. Del Grande, R. B. Capaz, L. Chico, and E. S. Morell. Flat bands and gaps in twisted double bilayer graphene. *Nanoscale*, 12(8):5014–5020, 2020.

[47] F. Haddadi, Q. S. Wu, A. J. Kruchkov, and O. V. Yazyev. Moiré flat bands in twisted double bilayer graphene. *Nano letters*, 20(4):2410–2415, 2020.

[48] E. McCann and M. Koshino. The electronic properties of bilayer graphene. *Reports on Progress in Physics*, 76(5):056503, 2013.

[49] R. T. Weitz, M. T. Allen, B. E. Feldman, J. Martin, and A. Yacoby. Broken-symmetry states in doubly gated suspended bilayer graphene. *Science*, 330(6005):812–816, 2010.

[50] M. Koshino and E. McCann. Gate-induced interlayer asymmetry in aba-stacked trilayer graphene. *Physical Review B*, 79(12):125443, 2009.

[51] Y. Zhang, T. T. Tang, C. Girit, Z. Hao, M. C. Martin, A. Zettl, M. F. Crommie, Y. R. Shen, and F. Wang. Direct observation of a widely tunable bandgap in bilayer graphene. *Nature*, 459(7248):820–823, 2009.

[52] Y. Shi, S. Che, K. Zhou, S. Ge, Z. Pi, T. Espiritu, T. Taniguchi, K. Watanabe, Y. Barlas, R. Lake, and C.N. Lau. Tunable lifshitz transitions and multiband transport in tetralayer graphene. *Physical Review Letters*, 120(9):096802, 2018.

[53] S. Xu, M. M. Al Ezzi, N. Balakrishnan, A. Garcia-Ruiz, B. Tsim, C. Mullan, J. Barrier, N. Xin, B. A. Piot, T. Taniguchi, K. Watanabe, A. Carvalho, A. Mishchenko, A. K. Geim, V. I. Fal'ko, S. Adam, A. H. Castro Neto, K. S. Novoselov, and Y. Shi. Tunable van Hove singularities and correlated states in twisted monolayer-bilayer graphene. *Nature Physics*, 17(5):619–626, 2021.

[54] E. Suárez Morell, M. Pacheco, L. Chico, and L. Brey. Electronic properties of twisted trilayer graphene. *Physical Review B*, 87(12):125414, 2013.

[55] M. Lee, J. R. Wallbank, P. Gallagher, K. Watanabe, T. Taniguchi, V. I. Fal'ko, and D. Goldhaber-Gordon. Ballistic miniband conduction in a graphene superlattice. *Science*, 353(6307):1526–1529, 2016.

[56] V. S. Tsoi. Focusing of electrons in a metal by a transverse magnetic field. *ZhETF Pisma Redaktsiiu*, 19:114, 1974.

[57] V. S. Tsoi. Determination of the dimensions of nonextremal Fermi-surface sections by transverse focusing of electrons. *Soviet Journal of Experimental and Theoretical Physics Letters*, 22:197, 1975.

[58] H. Van Houten, C. W. J. Beenakker, J. G. Williamson, M. E. I. Broekaart, P. H. M. Van Loosdrecht, B. J. Van Wees, J. E. Mooij, C. T. Foxon, and J. J. Harris. Coherent electron focusing with quantum point contacts in a two-dimensional electron gas. *Physical Review B*, 39(12):8556, 1989.

[59] J. J. Heremans, M. B. Santos, and M. Shayegan. Observation of magnetic focusing in two-dimensional hole systems. *Applied Physics Letters*, 61(14):1652–1654, 1992.

[60] T. Taychatanapat, K. Watanabe, T. Taniguchi, and P. Jarillo-Herrero. Electrically tunable transverse magnetic focusing in graphene. *Nature Physics*, 9(4):225–229, 2013.

[61] V. S. Tsoi, J. Bass, and P. Wyder. Studying conduction-electron/interface interactions using transverse electron focusing. *Reviews of Modern Physics*, 71(5):1641, 1999.

[62] N. W. Ashcroft and N. D. Mermin. Solid State Physics, 1976.

[63] D. Xiao, M.C. Chang, and Q. Niu. Berry phase effects on electronic properties. *Rev. Mod. Phys.*, 82(3):1959, 2010.

[64] H. Schmidt, T. Lüdtke, P. Barthold, E. McCann, V. I. Fal'ko, and R. J. Haug. Tunable graphene system with two decoupled monolayers. *Applied Physics Letters*, 93(17):172108, 2008.

[65] S. Slizovskiy, A. Garcia-Ruiz, A. I. Berdyugin, N. Xin, T. Taniguchi, K. Watanabe, A. K. Geim, N. D. Drummond, and V. I. Fal'ko. Out-of-plane dielectric susceptibility of graphene in twistronic and Bernal bilayers. *Nano Letters*, 21(15):6678–6683, 2021.

[66] J. D. Sanchez-Yamagishi, T. Taychatanapat, K. Watanabe, T. Taniguchi, A. Yacoby, and P. Jarillo-Herrero. Quantum Hall effect, screening, and layer-polarized insulating states in twisted bilayer graphene. *Physical Review Letters*, 108(7):076601, 2012.

[67] B. Fallahazad, Y. Hao, K. Lee, S. Kim, R. S. Ruoff, and E. Tutuc. Quantum Hall effect in Bernal stacked and twisted bilayer graphene grown on Cu by chemical vapor deposition. *Physical Review B*, 85(20):201408, 2012.

[68] Y. Shi, S. Xu, Y. Yang, S. Slizovskiy, S. V. Morozov, S. K. Son, S. Ozdemir, C. Mullan, J. Barrier, J. Yin, and A. I. Berdyugin. Electronic phase separation in multilayer rhombohedral graphite. *Nature*, 584(7820):210–214, 2020.

[69] E. H. Hwang and S. D. Sarma. Acoustic phonon scattering limited carrier mobility in two-dimensional extrinsic graphene. *Physical Review B*, 77(11):115449, 2008.

[70] L. Xian, S. Barraza-Lopez, and M. Y. Chou. Effects of electrostatic fields and charge doping on the linear bands in twisted graphene bilayers. *Physical Review B*, 84(7):075425, 2011.

[71] P. San-Jose and E. Prada. Helical networks in twisted bilayer graphene under interlayer bias. *Phys. Rev. B*, 88(12):121408, 2013.

[72] P. Moon, Y.-W. Son, and M. Koshino. Optical absorption of twisted bilayer graphene with interlayer potential asymmetry. *Physical Review B*, 90(15):155427, 2014.

[73] A. Ramires and J. L. Lado. Electrically tunable gauge fields in tiny-angle twisted bilayer graphene. *Physical Review Letters*, 121(14):146801, 2018.

[74] D. K. Efimkin and A. H. MacDonald. Helical network model for twisted bilayer graphene. *Phys. Rev. B*, 98(3):035404, 2018.

[75] M. Fleischmann, R. Gupta, F. Wullschläger, S. Theil, D. Weckbecker, V. Meded, S. Sharma, B. Meyer, and S. Shallcross. Perfect and controllable nesting in minimally twisted bilayer graphene. *Nano Letters*, 20(2):971–978, 2020.

[76] N. R. Walet and F. Guinea. The emergence of one-dimensional channels in marginal-angle twisted bilayer graphene. *2D Materials*, 7(1):015023, 2019.

[77] T. Hou, Y. Ren, Y. Quan, J. Jung, W. Ren, and Z. Qiao. Current partition and conducting topological networks in twisted graphene bilayer. *arXiv preprint arXiv:1904.12826*, 2019.

[78] E. McCann. Asymmetry gap in the electronic band structure of bilayer graphene. *Phys. Rev. B*, 74(16):161403, 2006.

[79] A. Vaezi, Y. Liang, D. H. Ngai, L. Yang, and E.-A. Kim. Topological edge states at a tilt boundary in gated multilayer graphene. *Phys. Rev. X*, 3:021018, Jun 2013.

[80] F. Zhang, A. H. MacDonald, and E. J. Mele. Valley chern numbers and boundary modes in gapped bilayer graphene. *PNAS*, 110(26):10546–10551, 2013.

[81] M. Pelc, W. Jaskólski, A. Ayuela, and L. Chico. Topologically confined states at corrugations of gated bilayer graphene. *Phys. Rev. B*, 92(8):085433, 2015.

[82] L. Ju, Z. Shi, N. Nair, Y. Lv, C. Jin, J. Velasco Jr, C. Ojeda-Aristizabal, H. A. Bechtel, M. C. Martin, A. Zettl, et al. Topological valley transport at bilayer graphene domain walls. *Nature*, 520(7549):650–655, 2015.

[83] L.-J. Yin, H. Jiang, J.-B. Qiao, and L. He. Direct imaging of topological edge states at a bilayer graphene domain wall. *Nature communications*, 7(1):1–6, 2016.

[84] C. Lee, G. Kim, J. Jung, and H. Min. Zero-line modes at stacking faulted domain walls in multilayer graphene. *Physical Review B*, 94(12):125438, 2016.

[85] J. Li, K. Wang, K. J. McFaul, Z. Zern, Y. Ren, K. Watanabe, T. Taniguchi, Z. Qiao, and J. Zhu. Gate-controlled topological conducting channels in bilayer graphene. *Nature nanotechnology*, 11(12):1060, 2016.

[86] M. Koshino. Electron delocalization in bilayer graphene induced by an electric field. *Phys. Rev. B*, 78(15):155411, 2008.

[87] L. Brown, R. Hovden, P. Huang, M. Wojcik, D. A. Muller, and J. Park. Twinning and twisting of tri-and bilayer graphene. *Nano Letters*, 12(3):1609–1615, 2012.

[88] J. Lin, W. Fang, W. Zhou, A. R. Lupini, J. C. Idrobo, J. Kong, S. J. Pennycook, and S. T. Pantelides. AC/AB stacking boundaries in bilayer graphene. *Nano Letters*, 13(7):3262–3268, 2013.

[89] J. S. Alden, A. W. Tsen, P. Y. Huang, R. Hovden, L. Brown, J. Park, D. A. Muller, and P. L. McEuen. Strain solitons and topological defects in bilayer graphene. *Proceedings of the National Academy of Sciences*, 110(28):11256–11260, 2013.

[90] P. Rickhaus, J. Wallbank, S. Slizovskiy, R. Pisoni, H. Overweg, Y. Lee, M. Eich, M. H. Liu, K. Watanabe, T. Taniguchi, T. Ihn, and K. Ensslin. Transport through a network of topological channels in twisted bilayer graphene. *Nano Letters*, 18(11):6725–6730, 2018.

[91] H. Yoo, R. Engelke, S. Carr, S. Fang, K. Zhang, P. Cazeaux, S. H. Sung, R. Hovden, A. W. Tsen, T. Taniguchi, K. Watanabe, G. C. Yi, M. Kim, M. Luskin, E. B. Tadmor, E. Kaxiras, and P. Kim. Atomic and electronic reconstruction at the van der Waals interface in twisted bilayer graphene. *Nature Materials*, 18(5):448, 2019.

[92] S. G. Xu, A. I. Berdyugin, P. Kumaravadivel, F. Guinea, R. K. Kumar, D. A. Bandurin, S. V. Morozov, W. Kuang, B. Tsim, S. Liu, J. H. Edgar, I. V. Grigorieva, V. I. Fal'ko, M. Kim, and A. K. Geim. Giant oscillations in a triangular network of one-dimensional states in marginally twisted graphene. *Nature Communications*, 10(4008), 2019.

[93] J. T. Chalker and P. D. Coddington. Percolation, quantum tunnelling and the integer hall effect. *Journal of Physics C: Solid State Physics*, 21(14):2665, 1988.

[94] B. Tsim, N. N. T. Nam, and M. Koshino. Perfect one-dimensional chiral states in biased twisted bilayer graphene. *Physical Review B*, 101(12):125409, 2020.

[95] M. Koshino and Y. W. Son. Moiré phonons in twisted bilayer graphene. *Physical Review B*, 100:075416, 2019.

[96] L. D. Landau, E. M. Lifshitz, and L. P. Pitaevskij. *Course of Theoretical Physics. Vol. 10, Section 79.* Oxford, 1981.

[97] J. M. Ziman. *Electrons and phonons: the theory of transport phenomena in solids*. Oxford University Press, 2001.

[98] J. R. Wallbank, R. K. Kumar, M. Holwill, Z. Wang, G. H. Auton, J. Birkbeck, A. Mishchenko, L. A. Ponomarenko, K. Watanabe, T. Taniguchi, K. S. Novoselov, I. L. Aleiner, A. K. Geim, and V. I Fal'ko. Excess resistivity in graphene superlattices caused by umklapp electron-electron scattering. *Nature Physics*, 15(1):32–36, 2019.

[99] J. Serrano, A. Bosak, R. Arenal, M. Krisch, K. Watanabe, T. Taniguchi, H. Kanda, A. Rubio, and L. Wirtz. Vibrational properties of hexagonal boron nitride: inelastic X-ray scattering and ab initio calculations. *Physical Review Letters*, 98(9):095503, 2007.